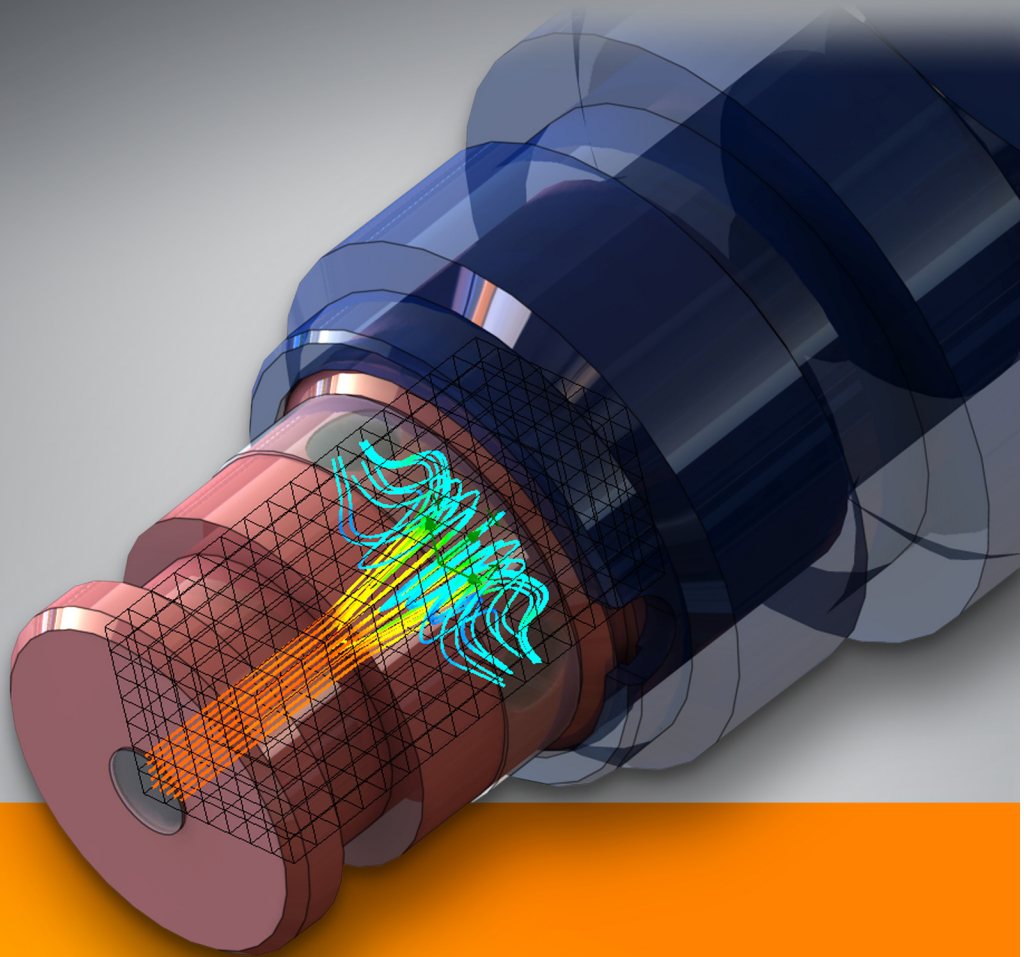


SolidWorks Flow Simulation 2012 Technical Reference



Contents

Technical Reference	1-1
Physical Capabilities of Flow Simulation	1-1
Governing Equations	1-3
The Navier-Stokes Equations for Laminar and Turbulent Fluid Flows	1-3
Laminar/turbulent Boundary Layer Model	1-7
Constitutive Laws and Thermophysical Properties	1-7
Real Gases	1-8
Compressible Liquids	1-11
Non-Newtonian Liquids	1-11
Equilibrium volume condensation of water from steam	1-14
Mass Transfer in Fluid Mixtures	1-14
Rotation	1-15
Global Rotating Reference Frame	1-15
Local rotating regions	1-15
Conjugate Heat Transfer	1-16
Joule Heating by Electric Current in Solids	1-17
Radiation Heat Transfer Between Solids	1-19
Ray Tracing	1-19
General Assumptions	1-19
The Ray Tracing Method	1-20
View Factor Calculation	1-22
Environment and Solar Radiation	1-23
Discrete Ordinates	1-23
General Assumptions	1-23
The Discrete Ordinates Method	1-24
Radiation Spectrum	1-26

Radiative Surface and Radiation Source Types	1-26
<i>Radiative Surfaces</i>	1-26
<i>Radiation Sources</i>	1-28
<i>Simultaneous Use of Radiative Surface and Radiation Source Conditions</i>	1-28
Viewing Results	1-28
Flows in Porous Media	1-29
General Approach	1-29
Perforated Plates in Boundary Conditions	1-31
Cavitation	1-31
Engineering cavitation model (for pre-defined water only)	1-32
Isothermal cavitation model	1-33
Two-phase (fluid + particles) Flows	1-34
Boundary Conditions and Engineering Devices	1-36
Internal Flow Boundary Conditions	1-36
External Flow Boundary Conditions	1-37
Wall Boundary Conditions	1-37
Internal Flow Boundary Conditions	1-38
Periodic Boundary Conditions	1-38
Heat Pipes	1-38
Thermal Joint	1-39
Two-resistor Components	1-39
Thermoelectric Coolers	1-40
HVAC	1-41
Local Mean Age	1-41
Comfort Parameters	1-41
Tracer Study	1-45
Numerical Solution Technique	1-48
Computational Mesh	1-48
Spatial Approximations	1-49
Spatial Approximations at the Solid/fluid Interface	1-50
Temporal Approximations	1-51
Form of the Numerical Algorithm	1-52
Methods to Resolve Linear Algebraic Systems	1-53
Iterative Methods for Nonsymmetrical Problems	1-53
Iterative Methods for Symmetric Problems	1-53
Multigrid Method	1-53
References	1-54
Validation Examples	2-1

Introduction	2-1
1 Flow through a Cone Valve	2-3
2 Laminar Flows Between Two Parallel Plates	2-7
3 Laminar and Turbulent Flows in Pipes	2-17
4 Flows Over Smooth and Rough Flat Plates	2-23
5 Flow in a 90-degree Bend Square Duct	2-27
6 Flows in 2D Channels with Bilateral and Unilateral Sudden Expansions	2-31
7 Flow over a Circular Cylinder	2-37
8 Supersonic Flow in a 2D Convergent-Divergent Channel	2-41
9 Supersonic Flow over a Segmental Conic Body	2-45
10 Flow over a Heated Plate	2-51
11 Convection and Radiation in an Annular Tube	2-55
12 Pin-fin Heat Sink Cooling by Natural Convection	2-61
13 Plate Fin Heat Sink Cooling by Forced Convection	2-65
14 Unsteady Heat Conduction in a Solid	2-69
15 Tube with Hot Laminar Flow and Outer Heat Transfer	2-73
16 Flow over a Heated Cylinder	2-77
17 Natural Convection in a Square Cavity	2-81
18 Particles Trajectories in Uniform Flows	2-85
19 Porous Screen in a Non-uniform Stream	2-89
20 Lid-driven Flows in Triangular and Trapezoidal Cavities	2-95
21 Flow in a Cylindrical Vessel with a Rotating Cover	2-101
22 Flow in an Impeller	2-105
23 Cavitation on a hydrofoil	2-111
24 Isothermal Cavitation in a Throttle Nozzle	2-115
25 Thermoelectric Cooling	2-119
References	2-123

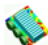
Technical Reference

Physical Capabilities of Flow Simulation

With Flow Simulation it is possible to study a wide range of fluid flow and heat transfer phenomena that include the following:

- External and internal fluid flows
- Steady-state and time-dependent fluid flows
- Compressible gas and incompressible fluid flows
- Subsonic, transonic, and supersonic gas flows
- Free, forced, and mixed convection
- Fluid flows with boundary layers, including wall roughness effects
- Laminar and turbulent fluid flows
- Multi-species fluids and multi-component solids
- Fluid flows in models with moving/rotating surfaces and/or parts
- Heat conduction in fluid, solid and porous media with/without conjugate heat transfer and/or contact heat resistance between solids and/or radiation heat transfer between opaque solids (some solids can be considered transparent for radiation), and/or volume (or surface) heat sources, e.g. due to Peltier effect, etc.
- Joule heating due to direct electric current in electrically conducting solids¹
- Various types of thermal conductivity in solid medium, *i.e.* isotropic, unidirectional, biaxial/axisymmetrical, and orthotropic
- Fluid flows and heat transfer in porous media



1. Capabilities and features marked with  are available for the **Electronics Cooling** module users only.

Physical Capabilities of Flow Simulation

- Flows of non-Newtonian liquids
- Flows of compressible liquids
- Real gases
- Cavitation in incompressible water flows
- Equilibrium volume condensation of water from steam and its influence on fluid flow and heat transfer
- Relative humidity in gases and mixtures of gases
- Two-phase (fluid + particles) flows
- Periodic boundary conditions.

Governing Equations

The Navier-Stokes Equations for Laminar and Turbulent Fluid Flows

Flow Simulation solves the Navier-Stokes equations, which are formulations of mass, momentum and energy conservation laws for fluid flows. The equations are supplemented by fluid state equations defining the nature of the fluid, and by empirical dependencies of fluid density, viscosity and thermal conductivity on temperature. Inelastic non-Newtonian fluids are considered by introducing a dependency of their dynamic viscosity on flow shear rate and temperature, and compressible liquids are considered by introducing a dependency of their density on pressure. A particular problem is finally specified by the definition of its geometry, boundary and initial conditions.

Flow Simulation is capable of predicting both *laminar* and *turbulent* flows. Laminar flows occur at low values of the Reynolds number, which is defined as the product of representative scales of velocity and length divided by the kinematic viscosity. When the Reynolds number exceeds a certain critical value, the flow becomes turbulent, i.e. flow parameters start to fluctuate randomly.

Most of the fluid flows encountered in engineering practice are turbulent, so Flow Simulation was mainly developed to simulate and study turbulent flows. To *predict* turbulent flows, *the Favre-averaged Navier-Stokes equations* are used, where time-averaged effects of the flow turbulence on the flow parameters are considered, whereas the other, i.e. large-scale, time-dependent phenomena are taken into account directly. Through this procedure, extra terms known as the Reynolds stresses appear in the equations for which additional information must be provided. To close this system of equations, Flow Simulation employs transport equations for the turbulent kinetic energy and its dissipation rate, the so-called *k- ϵ* model.

Flow Simulation employs one system of equations to describe both laminar and turbulent flows. Moreover, transition from a laminar to turbulent state and/or vice versa is possible.

Flows in models with moving walls (without changing the model geometry) are computed by specifying the corresponding boundary conditions. Flows in models with rotating parts are computed in coordinate systems attached to the models rotating parts, i.e. rotating with them, so the models' stationary parts must be axisymmetric with respect to the rotation axis.

Governing Equations

The conservation laws for mass, angular momentum and energy in the Cartesian coordinate system rotating with angular velocity Ω about an axis passing through the coordinate system's origin can be written in the conservation form as follows:

$$\frac{\partial \rho}{\partial t} + \frac{\partial}{\partial x_i}(\rho u_i) = 0 \quad (1.1)$$

$$\frac{\partial \rho u_i}{\partial t} + \frac{\partial}{\partial x_j}(\rho u_i u_j) + \frac{\partial p}{\partial x_i} = \frac{\partial}{\partial x_j}(\tau_{ij} + \tau_{ij}^R) + S_i \quad i = 1, 2, 3 \quad (1.2)$$

$$\frac{\partial \rho H}{\partial t} + \frac{\partial \rho u_i H}{\partial x_i} = \frac{\partial}{\partial x_i} \left(u_j (\tau_{ij} + \tau_{ij}^R) + q_i \right) + \frac{\partial p}{\partial t} - \tau_{ij}^R \frac{\partial u_i}{\partial x_j} + \rho \varepsilon + S_i u_i + Q_H, \quad (1.3)$$

$$H = h + \frac{u^2}{2},$$

where u is the fluid velocity, ρ is the fluid density, S_i is a mass-distributed external force per unit mass due to a porous media resistance (S_i^{porous}), a buoyancy ($S_i^{gravity} = -\rho g_i$, where g_i is the gravitational acceleration component along the i -th coordinate direction), and the coordinate system's rotation ($S_i^{rotation}$), i.e., $S_i = S_i^{porous} + S_i^{gravity} + S_i^{rotation}$, h is the thermal enthalpy, Q_H is a heat source or sink per unit volume, τ_{ik} is the viscous shear stress tensor, q_i is the diffusive heat flux. The subscripts are used to denote summation over the three coordinate directions.

For calculations with the **High Mach number flow** option enabled, the following energy equation is used:

$$\frac{\partial \rho E}{\partial t} + \frac{\partial \rho u_i \left(E + \frac{p}{\rho} \right)}{\partial x_i} = \frac{\partial}{\partial x_i} \left(u_j (\tau_{ij} + \tau_{ij}^R) + q_i \right) - \tau_{ij}^R \frac{\partial u_i}{\partial x_j} + \rho \varepsilon + S_i u_i + Q_H, \quad (1.4)$$

$$E = e + \frac{u^2}{2},$$

where e is the internal energy.

For Newtonian fluids the viscous shear stress tensor is defined as:

$$\tau_{ij} = \mu \left(\frac{\partial u_i}{\partial x_j} + \frac{\partial u_j}{\partial x_i} - \frac{2}{3} \delta_{ij} \frac{\partial u_k}{\partial x_k} \right) \quad (1.5)$$

Following Boussinesq assumption, the Reynolds-stress tensor has the following form:

$$\tau_{ij}^R = \mu_t \left(\frac{\partial u_i}{\partial x_j} + \frac{\partial u_j}{\partial x_i} - \frac{2}{3} \delta_{ij} \frac{\partial u_k}{\partial x_k} \right) - \frac{2}{3} \rho k \delta_{ij} \quad (1.6)$$

Here δ_{ij} is the Kronecker delta function (it is equal to unity when $i = j$, and zero otherwise), μ is the dynamic viscosity coefficient, μ_t is the turbulent eddy viscosity coefficient and k is the turbulent kinetic energy. Note that μ_t and k are zero for laminar flows. In the frame of the k - \mathcal{E} turbulence model, μ_t is defined using two basic turbulence properties, namely, the turbulent kinetic energy k and the turbulent dissipation \mathcal{E} ,

$$\mu_t = f_\mu \frac{C_\mu \rho k^2}{\mathcal{E}} \quad (1.7)$$

Here f_μ is a turbulent viscosity factor. It is defined by the expression

$$f_\mu = [1 - \exp(-0.025 R_y)]^2 \cdot \left(1 + \frac{20.5}{R_T} \right) , \quad (1.8)$$

$$\text{where } R_T = \frac{\rho k^2}{\mu \mathcal{E}} , \quad R_y = \frac{\rho \sqrt{k} y}{\mu}$$

and y is the distance from the wall. This function allows us to take into account laminar-turbulent transition.

Two additional transport equations are used to describe the turbulent kinetic energy and dissipation,

$$\frac{\partial \rho k}{\partial t} + \frac{\partial}{\partial x_i} (\rho u_i k) = \frac{\partial}{\partial x_i} \left(\left(\mu + \frac{\mu_t}{\sigma_k} \right) \frac{\partial k}{\partial x_i} \right) + S_k , \quad (1.9)$$

$$\frac{\partial \rho \mathcal{E}}{\partial t} + \frac{\partial}{\partial x_i} (\rho u_i \mathcal{E}) = \frac{\partial}{\partial x_i} \left(\left(\mu + \frac{\mu_t}{\sigma_\mathcal{E}} \right) \frac{\partial \mathcal{E}}{\partial x_i} \right) + S_\mathcal{E} , \quad (1.10)$$

Governing Equations

where the source terms S_k and S_ε are defined as

$$S_k = \tau_{ij}^R \frac{\partial u_i}{\partial x_j} - \rho \varepsilon + \mu_t P_B \quad (1.11)$$

$$S_\varepsilon = C_{\varepsilon 1} \frac{\varepsilon}{k} \left(f_1 \tau_{ij}^R \frac{\partial u_i}{\partial x_j} + \mu_t C_B P_B \right) - C_{\varepsilon 2} f_2 \frac{\rho \varepsilon^2}{k} . \quad (1.12)$$

Here P_B represents the turbulent generation due to buoyancy forces and can be written as

$$P_B = - \frac{g_i}{\sigma_B} \frac{1}{\rho} \frac{\partial \rho}{\partial x_i} \quad (1.13)$$

where g_i is the component of gravitational acceleration in direction x_i , the constant $\sigma_B = 0.9$, and constant C_B is defined as: $C_B = 1$ when $P_B > 0$, and 0 otherwise;

$$f_1 = 1 + \left(\frac{0.05}{f_\mu} \right)^3, \quad f_2 = 1 - \exp(-R_T^2) \quad (1.14)$$

The constants C_μ , $C_{\varepsilon 1}$, $C_{\varepsilon 2}$, σ_k , σ_ε are defined empirically. In Flow Simulation the following typical values are used:

$$C_\mu = 0.09, C_{\varepsilon 1} = 1.44, C_{\varepsilon 2} = 1.92, \sigma_\varepsilon = 1.3, \quad \sigma_k = 1 \quad (1.15)$$

Where Lewis number $Le=1$ the diffusive heat flux is defined as:

$$q_i = \left(\frac{\mu}{Pr} + \frac{\mu_t}{\sigma_c} \right) \frac{\partial h}{\partial x_i}, \quad i = 1, 2, 3. \quad (1.16)$$

Here the constant $\sigma_c = 0.9$, Pr is the Prandtl number, and h is the thermal enthalpy.

These equations describe both laminar and turbulent flows. Moreover, transitions from one case to another and back are possible. The parameters k and μ_t are zero for purely laminar flows.

Laminar/turbulent Boundary Layer Model

A laminar/turbulent boundary layer model is used to describe flows in near-wall regions. The model is based on the so-called Modified Wall Functions approach. This model is employed to characterize laminar and turbulent flows near the walls, and to describe transitions from laminar to turbulent flow and vice versa. The modified wall function uses a Van Driest's profile instead of a logarithmic profile. If the size of the mesh cell near the wall is more than the boundary layer thickness the integral boundary layer technology is used. The model provides accurate velocity and temperature boundary conditions for the above mentioned conservation equations.

Constitutive Laws and Thermophysical Properties

The system of Navier-Stokes equations is supplemented by definitions of thermophysical properties and state equations for the fluids. Flow Simulation provides simulations of gas and liquid flows with density, viscosity, thermal conductivity, specific heats, and species diffusivities as functions of pressure, temperature and species concentrations in fluid mixtures, as well as equilibrium volume condensation of water from steam can be taken into account when simulating steam flows.

Generally, the state equation of a fluid has the following form:

$$\rho = f(p, T, y), \quad (1.17)$$

where $y = (y_1, \dots, y_M)$ is the concentration vector of the fluid mixture components.

Excluding special cases (see below subsections concerning **Real Gases, Equilibrium volume condensation of water from steam**), **gases** are considered ideal, i.e. having the state equation of the form

$$\rho = \frac{P}{RT}, \quad (1.18)$$

where R is the gas constant which is equal to the universal gas constant R_{univ} divided by the fluid molecular mass M , or, for the mixtures of ideal gases,

$$R = R_{univ} \sum_m \frac{y_m}{M_m}, \quad (1.19)$$

where y_m , $m=1, 2, \dots, M$, are the concentrations of mixture components, and M_m is the molecular mass of the m -th component.

Specific heat at constant pressure, as well as the thermophysical properties of the gases, i.e. viscosity and thermal conductivity, are specified as functions of temperature. In addition, proceeding from Eq. (1.18), each of such gases has constant specific heat ratio C_p/C_v .

Governing Equations

Excluding special cases (see below subsections **Compressible Liquids, Non-Newtonian Liquids**), **liquids** are considered incompressible, i.e. the density of an individual liquid depends only on temperature:

$$\rho = f(T) \quad , \quad (1.20)$$

and the state equation for a mixture of liquids is defined as

$$\rho = \left(\sum_m \frac{y_m}{\rho_m} \right)^{-1} \quad (1.21)$$

The specific heat and the thermophysical properties of the liquid (i.e. viscosity and thermal conductivity), are specified as functions of temperature.

Real Gases

The state equation of ideal gas (1.18) become inaccurate at high pressures or in close vicinity of the gas-liquid phase transition curve. Taking this into account, a real gas state equation together with the related equations for thermodynamical and thermophysical properties should be employed in such conditions. At present, this option may be used only for a single gas, probably mixed with ideal gases.

In case of user-defined real gas, Flow Simulation uses a custom modification of the Redlich-Kwong equation that may be expressed in dimensionless form as follows:

$$p_r = T_r \left(\frac{1}{\Phi_r - b} - \frac{aF}{\Phi_r (\Phi_r + c)} \right) \quad (1.22)$$

where $p_r = p/p_c$, $T_r = T/T_c$, $\Phi_r = V_r \cdot Z_c$, $V_r = V/V_c$, $F = T_r^{-1.5}$, p_c , T_c , and V_c are the user-specified critical parameters of the gas, i.e. pressure, temperature, and specific volume at the critical point, and Z_c is the gas compressibility factor that also defines the a , b , and c constants.

A particular case of equation (1.22) with $Z_c = 1/3$ (which in turn means that $b=c$) is the original Redlich equation as given in Ref. 1.

Alternatively, one of the modifications (Ref. 1) taking into account the dependence of F on temperature and the Pitzer acentricity factor ω may be used: the Wilson modification, the Barnes-King modification, or the Soave modification.

The specific heat of real gas at constant pressure (C_p) is determined as the combination of the user-specified temperature-dependent "ideal gas" specific heat (C_p^{ideal}) and the automatically calculated correction. The former is a polynomial with user-specified order and coefficients. The specific heat at constant volume (C_v) is calculated from C_p by means of the state equation.

Likewise, the thermophysical properties are defined as a sum of user-specified "basic" temperature dependency (which describes the corresponding property in extreme case of low pressure) and the pressure-dependent correction which is calculated automatically.

The basic dependency for dynamic viscosity η of the gas is specified in a power-law form: $\eta = a \cdot T^n$. The same property for liquid is specified either in a similar power-law form $\eta = a \cdot T^n$ or in an exponential form: $\eta = 10^{a(1/T-1/n)}$. As for the correction, it is given according to the Jossi-Stiel-Thodos equation for non-polar gases or the Stiel-Thodos equations for polar gases (see Ref. 1), judging by the user-specified attribute of polarity. The basic dependencies for thermal conductivities λ of the substance in gaseous and liquid states are specified by the user either in linear $\lambda = a + n \cdot T$ or in power-law $\lambda = a \cdot T^n$ forms, and the correction is determined from the Stiel-Thodos equations (see Ref. 1).

All user-specified coefficients must be entered in SI unit system, except those for the exponential form of dynamic viscosity of the liquid, which should be taken exclusively from Ref. 1.

In case of pre-defined real gas, the custom modification of the Redlich-Kwong equation of the same form as Eq. (1.22) is used, with the distinction that the coefficients a , b , and c are specified explicitly as dependencies on T_r in order to reproduce the gas-liquid phase transition curve at $P < P_c$ and the critical isochore at $P > P_c$ with higher precision.

Governing Equations

When the calculated (p, T) point drops out of the region bounded by the temperature and pressure limits (zones 1 - 8 on Fig.1.1) or gets beyond the gas-liquid phase transition curve (zone 9 on Fig.1.1), the corresponding warnings are issued and properties of the real gas are extrapolated linearly.

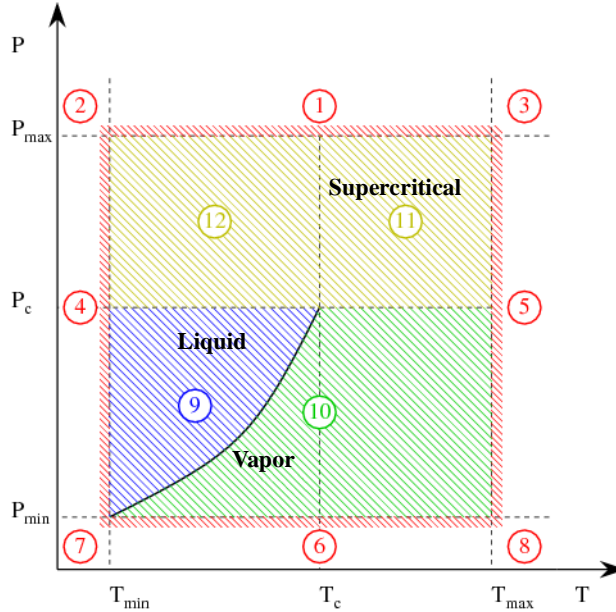


Fig.1.1

If a real gas mixes with ideal gases (at present, mixtures of multiple real gases are not considered), properties of this mixture are determined as an average weighted with mass or volume fractions:

$$v = \sum_{i=1}^N Y_i v_i \quad (1.23)$$

where v is the mixture property (i.e., C_p , μ , or λ), N is the total number of the mixture gases (one of which is real and others are ideal), Y_i is the mass fraction (when calculating C_p) or the volume fraction (when calculating μ and λ) of the i -th gas in the mixture.

The real gas model has the following limitations and assumptions:

- The precision of calculation of thermodynamic properties at nearly-critical temperatures and supercritical pressures may be lowered to some extent in comparison to other temperature ranges. Generally speaking, the calculations involving user-defined real gases at supercritical pressures are not recommended.

- The user-defined dependencies describing the specific heat and transport properties of the user-defined real gases should be applicable in the whole $T_{\min} \dots T_{\max}$ range (or, speaking about liquid, in the whole temperature range where the liquid exists).
- T_{\min} for user-defined real gas should be set at least 5...10 K higher than the triple point of the substance in question.

Compressible Liquids

Compressible liquids whose density depends on pressure and temperature can be considered within the following approximations:

- obeying the logarithmic law:

$$\rho = \rho_0 \cdot \left(1 - C \cdot \ln \frac{B + P}{B + P_0} \right),$$

where ρ_0 is the liquid's density under the reference pressure P_0 , C , B are coefficients, here ρ_0 , C , and B can depend on temperature, P is the calculated pressure;

- obeying the power law:

$$\rho = \rho_0 \cdot \left(\frac{P + B}{P_0 + B} \right)^{1/n},$$

where, in addition to the above-mentioned designations, n is a power index which can be temperature dependent.

Non-Newtonian Liquids

Flow Simulation is capable of computing laminar flows of inelastic non-Newtonian liquids. In this case the viscous shear stress tensor is defined, instead of Eq. (1.5), as

$$\tau_{ij} = \mu(\dot{\gamma}) \cdot \left(\frac{\partial u_i}{\partial x_j} + \frac{\partial u_j}{\partial x_i} \right), \quad (1.24)$$

where shear rate,

$$\dot{\gamma} = \sqrt{d_{ij}^2 - d_{ii} \cdot d_{jj}}, \quad d_{ij} = \frac{\partial u_i}{\partial x_j} + \frac{\partial u_j}{\partial x_i}$$

and for specifying a viscosity function $\mu(\dot{\gamma})$ the following five models of inelastic non-Newtonian viscous liquids are available in Flow Simulation:

Governing Equations

- The Herschel-Bulkley model:

$$\mu(\dot{\gamma}) = K \cdot (\dot{\gamma})^{n-1} + \frac{\tau_o}{\dot{\gamma}},$$

where K is the liquid's consistency coefficient, n is the liquid's power law index, and τ_o is the liquid's yield stress.

This model includes the following special cases:

- $n = 1$, $\tau_o = 0$ describes Newtonian liquids, in this case K is the liquid's dynamic viscosity;
- $n = 1$, $\tau_o > 0$ describes the Bingham model of non-Newtonian liquids, featured by a non-zero threshold yield stress (τ_o) below of which the liquid behaves as a solid, so to achieve a flow this threshold shear stress must be exceeded. (In Flow Simulation this threshold is modeled by automatically equating K , named plastic viscosity in this case, to a substantially high value at $\tau < \tau_o$);
- $0 < n < 1$, $\tau_o = 0$ describes the power law model of shear-thinning non-Newtonian liquids (see also below);
- $n > 1$, $\tau_o = 0$ describes the power law model of shear-thickening non-Newtonian liquids (see also below);

- The power-law model:

$$\mu(\dot{\gamma}) = K \cdot (\dot{\gamma})^{n-1}$$

in contrast to the Herschel-Bulkley model's special case, the μ values are restricted:

$$\mu_{\min} \leq \mu \leq \mu_{\max};$$

- The Carreau model:

$$\mu = \mu_{\infty} + (\mu_o - \mu_{\infty}) \cdot \left[1 + (K_t \cdot \dot{\gamma})^2 \right]^{(n-1)/2},$$

where:

- μ_{∞} is the liquid's dynamic viscosity at infinite shear rate, i.e., the minimum dynamic viscosity;
- μ_o is the liquid's dynamic viscosity at zero shear rate, i.e., the maximum dynamic viscosity;
- K_t is the time constant;
- n is the power law index.

This model is a smooth version of the power law model with the μ restrictions.

In all these three models described above, all parameters with the exception of the dimensionless power law index can be temperature-dependent.

- The Cross-William-Landel-Ferry (Cross-WLF) model is another modification of the power-law model for shear-thinning liquids. It takes into account the effects of the temperature T :

$$\mu(T, \dot{\gamma}, p) = \frac{\mu_0(T, p)}{1 + \left[\frac{\mu_0(T, p) \cdot \dot{\gamma}}{\tau_*} \right]^{(1-n)}} ,$$

where:

- $\mu_0(T) = D_1 \cdot e^{\left[-\frac{A_1 \cdot (T - T_*)}{A_2 + (T - T_*)} \right]}$ is the zero-shear viscosity;
- $T_* = D_2$ is the glass-transition temperature;
- n is the power-law index;
- τ_* is the shear stress at which the liquid changes its behavior from Newtonian to a shear-thinning one;
- A_1, A_2, D_1 and D_2 are the additional model constants.
- The Polynomial regression model:
 $\ln \mu(\dot{\gamma}, T) = C_1 + C_2 \ln \dot{\gamma} + C_3 \ln^2 \dot{\gamma} + C_4 T + C_5 T \ln \dot{\gamma} + C_6 T \ln^2 \dot{\gamma}$,
 where $C_i, i = 1 \dots 6$ are the user-specified coefficients.

The minimum shear rate, below which the viscosity is considered constant, can be determined automatically as the point where $\mu(\dot{\gamma})$ reaches its maximum value.

The minimum shear rate can also be manually specified by user. The maximum shear rate, after which the viscosity is considered constant, can be specified by user also.

- The Viscosity table model defines the liquid's viscosity $\mu(\dot{\gamma}, T)$ by linear interpolation or polynomial approximation of the user-specified tabular dependencies of the viscosity μ on the shear rate $\dot{\gamma}$ at the various temperatures T . Coefficients of the 2nd and 3rd order polynomials are automatically determined with the least squares method. In addition, the user can specify the minimum and maximum shear rates, outside of which the viscosity μ is constant. The minimum shear rate for 2nd order polynomials can be determined automatically as the point where $\mu(\dot{\gamma})$ reaches its maximum value.

Equilibrium volume condensation of water from steam

If the gas whose flow is computed includes steam, Flow Simulation can predict an equilibrium volume condensation of water from this steam (without any surface condensation) taking into account the corresponding changes of the steam temperature, density, enthalpy, specific heat, and sonic velocity. In accordance with the equilibrium approach, local mass fraction of the condensed water in the local total mass of the steam and the condensed water is determined from the local temperature of the fluid, pressure, and, if a multi-component fluid is considered, the local mass fraction of the steam. Since this model implies an equilibrium conditions, the condensation has no history, i.e. it is a local fluid property only.

In addition, it is assumed that

- the volume of the condensed water is neglected, i.e. considered zero, so this prediction works properly only if the volume fraction of the condensed water does not exceed 5%,
- the steam temperature falls into the range of 283...610 K and the pressure does not exceed 10 MPa.

Mass Transfer in Fluid Mixtures

The mass transfer in fluid mixtures is governed by species conservation equations. The equations that describe concentrations of mixture components can be written as

$$\frac{\partial \rho y_m}{\partial t} + \frac{\partial}{\partial x_i} (\rho u_i y_m) = \frac{\partial}{\partial x_i} \left((D_{mn} + D_{mn}^t) \frac{\partial y_n}{\partial x_i} \right) + S_m, \quad m = 1, 2, \dots, M \quad (1.25)$$

Here D_{mn} , D_{mn}^t are the molecular and turbulent matrices of diffusion, S_m is the rate of production or consumption of the m -th component.

In case of Fick's diffusion law:

$$D_{mn} = D \cdot \delta_{mn}, \quad D_{mn}^t = \delta_{mn} \cdot \frac{\mu_t}{\sigma} \quad (1.26)$$

The following obvious algebraic relation between species concentrations takes place:

$$\sum_m y_m = 1. \quad (1.27)$$

Rotation

Global Rotating Reference Frame

The rotation of the coordinate system is taken into account via the following mass-distributed force:

$$S_i^{rotation} = -2e_{ijk}\Omega_j\rho u_k + \rho\Omega^2 r_i ,$$

where e_{ijk} is the Levy-Civita symbols (function), Ω is the angular velocity of the rotation, r is the vector coming to the point under consideration from the nearest point lying on the rotation axis.

Local rotating regions

This option is employed for calculating time-dependent (transient) or steady-state flows in regions surrounding rotating non-axisymmetrical solids (e.g. impellers, mixers, propellers, etc), when a single global rotating reference cannot be employed. For example, local rotating regions can be used in analysis of the fluid flow in the model including several components rotating over different axes and/or at different speeds or if the computational domain has a non-axisymmetrical (with respect to a rotating component) outer solid/fluid interface. In accordance with the employed approach, each rotating solid component is surrounded by an axisymmetrical (with respect to the component's rotation axis) **Rotating region**, which has its own coordinate system rotating together with the component. If the model includes several rotating solid components having different rotation axes, the rotating regions surrounding these components must not intersect with each other. The fluid flow equations in the stationary (non-rotating) regions of the computational domain are solved in the inertial (non-rotating) Cartesian Global Coordinate System. The influence of the rotation's effect on the flow is taken into account in the equations written in each of the rotating coordinate systems.

Governing Equations

To connect solutions obtained within the rotating regions and in non-rotating part of the computational domain, special internal boundary conditions are set automatically at the fluid boundaries of the rotating regions. Since the coordinate system of the rotating region rotates, the rotating region's boundaries are sliced into rings of equal width as shown on the Fig.1.2. Then the values of flow parameters transferred as boundary conditions from the adjacent fluid regions are averaged circumferentially over each of these rings.

Computational domain or fluid subdomain
Flow parameters are calculated in the inertial Global Coordinate System

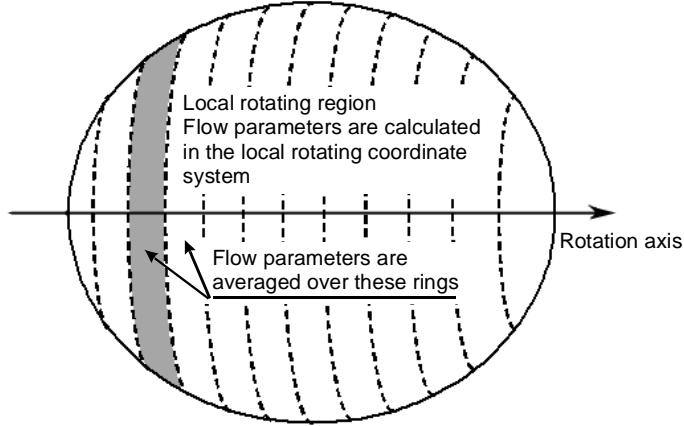


Fig.1.2

To solve the problem, an iterative procedure of adjusting the flow solutions in the rotating regions and in the adjacent non-rotating regions, therefore in the entire computational domain, is performed with relaxations.

Please note that even in case of time-dependent (transient) analysis the flow parameters within the rotating regions are calculated using a steady-state approach and averaged on the rotating regions' boundaries as described above.

Conjugate Heat Transfer

Flow Simulation allows to predict simultaneous heat transfer in solid and fluid media with energy exchange between them. Heat transfer in fluids is described by the energy conservation equation (1.3) where the heat flux is defined by (1.16). The phenomenon of anisotropic heat conductivity in solid media is described by the following equation:

$$\frac{\partial \rho e}{\partial t} = \frac{\partial}{\partial x_i} \left(\lambda_i \frac{\partial T}{\partial x_i} \right) + Q_H, \quad (1.28)$$

where e is the specific internal energy, $e = c \cdot T$, c is specific heat, Q_H is specific heat release (or absorption) per unit volume, and λ_i are the eigenvalues of the thermal conductivity tensor. It is supposed that the heat conductivity tensor is diagonal in the considered coordinate system. For isotropic medium $\lambda_1 = \lambda_2 = \lambda_3 = \lambda$.

If a solid consists of several solids attached to each other, then the thermal contact resistances between them (on their contact surfaces), specified in the Engineering database in the form of contact conductance (as $m^2 \cdot K/W$), can be taken into account when calculating the heat conduction in solids. As a result, a solid temperature step appears on the contact surfaces. In the same manner, i.e. as a thermal contact resistance, a very thin layer of another material between solids or on a solid in contact with fluid can be taken into account when calculating the heat conduction in solids, but it is specified by the material of this layer (its thermal conductivity taken from the Engineering database) and thickness. The surface heat source (sink) due to Peltier effect may also be considered (see **"Thermoelectric Coolers"** on page 1-40).

The energy exchange between the fluid and solid media is calculated via the heat flux in the direction normal to the solid/fluid interface taking into account the solid surface temperature and the fluid boundary layer characteristics, if necessary.

If a solid medium is porous with a fluid flowing through it, then a conjugate heat transfer problem in this porous-solid/fluid medium can be solved also in the manner described below. The equations (1.3) and (1.28) are solved in a usual way, but with addition of energy exchange between the fluid and the porous solid matrix, defined via the volumetric heat exchange in the Eq. (1.28) in a form of $Q_H^{porosity} = \gamma \cdot (T_p - T)$, where γ is the user-defined volumetric coefficient of heat transfer between fluid and the porous matrix, T_p is the temperature of the porous matrix, T is the fluid temperature, and the same Q_H with the opposite sign is employed in Eq. (1.28) for the porous matrix. Note that the γ and c of the porous matrix used in Eq. (1.28) can differ from those of the corresponding bulk solid material. Naturally, both the fluid flow equations and the porous matrix heat transfer equation take into account the fluid and solid densities multiplied by the corresponding fluid and solid volume fractions in the porous matrix.

Joule Heating by Electric Current in Solids



This feature is available for the Electronics Cooling module users only.

Flow Simulation is able to calculate steady-state (and quasi time-dependent) direct electric current in electroconductive solids. In presence of the electric current, the corresponding specific Joule heat $Q_J [W/m^3]$ is released and included in Q_H of heat transfer equation (1.28) (see **"Conjugate Heat Transfer"** on page 1-16). In the case of isotropic material Q_J is

$$Q_J = r \cdot i^2, \quad (1.29)$$

Governing Equations

where r is the solids' electrical resistivity [$\Omega\cdot m$] (it can be temperature-dependent) and i is the electric current density [A/m^2].

The electric current density vector

$$\mathbf{i} = -\left(\frac{1}{r_{11}} \frac{\partial \varphi}{\partial x_1}, \frac{1}{r_{22}} \frac{\partial \varphi}{\partial x_2}, \frac{1}{r_{33}} \frac{\partial \varphi}{\partial x_3} \right), \quad (1.30)$$

is determined via the electric potential φ [V]. To obtain the electric potential φ , Flow Simulation utilizes the steady-state Laplace equation

$$\frac{\partial}{\partial x_i} \left(\frac{1}{r_{ii}} \frac{\partial \varphi}{\partial x_i} \right) = 0 \quad (1.31)$$

Here r_{ii} is the temperature-dependent electrical resistivity in the i -th coordinate direction.

Transient electric problems with boundary conditions depending on time are considered as quasi-steady-state. In this case the steady-state problem for potential is solved at each time step, not taking into account transient electrical processes in solids.

The Laplace equation is solved numerically in the computational subdomain (it may be a part of the overall computational domain) of electroconductive materials. This computational subdomain automatically excludes dielectric solids and fluid areas inside. The total electric current in normal direction over a surface I_n [A] or electric potential φ [V] may be specified by user as boundary conditions for the problem. These conditions may be imposed on surfaces between fluid/electroconductive solid, electroconductive solid/electroconductive solid, dielectric solid/electroconductive solid, and outer solid surfaces. If no electrical boundary conditions are specified by user, the $I_n = 0$ boundary condition is automatically specified by default on bounding surfaces.

A surface between electroconductive solids in the computational subdomain is either considered zero-resistance (default) or the electric contact resistance is specified on it. The resistance value is either given explicitly or calculated from the given material and its thickness.

A contact resistance specified on a surface implies that the current passing through it produces the corresponding Joule heating, which yields the following surface heat source Q_{JS} [W/m^2]:

$$Q_{JS} = i_n \cdot \Delta \varphi \quad (1.32)$$


where i_n is the electric current density normal to the surface and $\Delta \varphi$ is the electric potential drop at this surface.

The anisotropic electrical resistivity of electroconductive solids can be anisotropic, i.e. specified by its components in the coordinate system's directions r_i , $i = 1, 2, 3$. The isotropic/anisotropic type of material is specified for electrical resistivity and thermal conductivity simultaneously, i.e. so that their main axes coincide.

Radiation Heat Transfer Between Solids

In addition to heat conduction in solids, Flow Simulation is capable of calculating radiation heat transfer between solids which surface emissivity is specified. If necessary, a heat radiation from the computational domain far-field boundaries or the model openings can also be defined and considered either as thermal, i.e. by specifying the boundaries emissivity and temperature, or as a solar radiation defined by the specified location (on the surface of the Earth) and time (including date) or by a constant or time-dependent direction and intensity.

Depending on the following conditions, two different approaches are used:

- ❑ If the heat radiation absorption in solids or radiation spectrum are not considered in the analysis, the radiative heat transfer is calculated using the Ray Tracing approach.
-  ❑ If the heat radiation absorption in solids or radiation spectrum are considered, the Discrete Ordinates method is used.¹

Ray Tracing

General Assumptions

- ❑ The heat radiation from the solid surfaces, both the emitted and reflected, is assumed diffuse (except for the symmetry radiative surface type), i.e. obeying the Lambert law, according to which the radiation intensity per unit area and per unit solid angle is the same in all directions.
- ❑ The solar radiation is absorbed and reflected by surfaces independently from thermal radiation from all other heat radiation sources.
- ❑ The propagating heat radiation passes through a solid specified as radiation transparent without any refraction and/or absorption. A solid can be specified as transparent to the solar radiation only, or transparent to the thermal radiation from all sources except the solar radiation, or transparent to both types of radiation, thermal and solar.
- ❑ The project fluids neither emit nor absorb heat radiation (i.e., they are transparent to the heat radiation), so the heat radiation concerns solid surfaces only.
- ❑ The radiative solid surfaces which are not specified as a blackbody or whitebody are assumed an ideal graybody, i.e. having a continuous emissive power spectrum similar to that of blackbody, so their monochromatic emissivity is independent of the emission wavelength. For certain materials with certain surface conditions, the graybody emissivity can depend on the surface temperature.

1. Capabilities and features marked with  are available for the **HVAC** module users only.

The Ray Tracing Method

In a general case, the surfaces participating in the heat radiation (hereinafter **radiative surfaces**) can emit, absorb, and reflect a heat radiation (both the solar and thermal). The heat radiation leaving a radiative surface or radiation source is defined as:

$$q_T = \varepsilon \cdot \sigma \cdot T^4 + \rho_T \cdot q_{T,i} \text{ for thermal radiation,}$$

where: ε is the surface emissivity, σ is the Stefan-Boltzmann constant, T is the temperature of the surface ($\varepsilon \sigma T^4$ is the heat radiated by this surface in accordance with the Stefan-Boltzmann law), $q_{T,i}$ is the incident thermal radiation arriving at this surface, ρ_T is the surface reflectivity for thermal radiation ($\rho_T = 1 - \varepsilon$ for graybody walls and $\rho = 0$ for diffusive radiation sources);

and

$$q_S = \rho_S \cdot q_{S,i} \text{ for solar radiation,}$$

where: ρ_S is the surface reflectivity for solar radiation determined from the solar absorptance α as $\rho_T = 1 - \alpha$ ($\rho_T = 1$ for graybody walls and $\rho = 0$ for solar radiation sources), $q_{S,i}$ is the incident solar radiation arriving at this surface.

The total heat radiation q leaving the surface, which is determined as:

$$q = q_T + q_S ;$$

and the net radiation q_N being the difference between the heat radiation leaving this surface and the incident heat radiation $q_i = q_{T,i} + q_{S,i}$ arriving at it:

$$q_N = q - q_i = (q_T + q_S) - (q_{T,i} + q_{S,i});$$

are calculated for each of the surfaces participating in the radiation heat transfer.

In order to reduce the of memory requirements, the problem of determining the leaving and net heat radiation fluxes is solved using a discrete ray Monte-Carlo approach consisting of the following main elements:

- ❑ To reduce the number of radiation rays and, therefore, the required calculation time and resources, the computational mesh cells containing faces approximating the radiative surfaces are joined in clusters by a special procedure that takes into account the face area and angle between normal and face in each partial cell. The cells intersected by boundaries between radiative surfaces of different emissivity are considered as belonging to one of these surfaces and cannot be combined in one cluster. This procedure is executed after constructing the computational mesh before the calculation and after each solution-adaptive mesh refinement, if any.
- ❑ From each cluster, a number of rays are emitted, equally distributed over the enclosing unit hemisphere. Each ray is traced through the fluid and transparent solid bodies until

it intercepts the computational domain's boundary or a cluster belonging to another radiative surface, thus defining a 'target' cluster. Since the radiation heat is transferred along these rays only, their number and arrangement govern the accuracy of calculating the radiation heat coming from one radiative surface to another (naturally, the net heat radiated by a radiative surface does not depend on number of these rays). So, for each of the clusters, the hemisphere governed by the ray's origin and the normal to the face at this origin is uniformly divided into several nearly equal solid angles generated by several zenith angles (at least 3 within the 0...90° range, including the zero zenith angle of the normal to the face) and several azimuth angles (at least 12 within the 0...360° range).

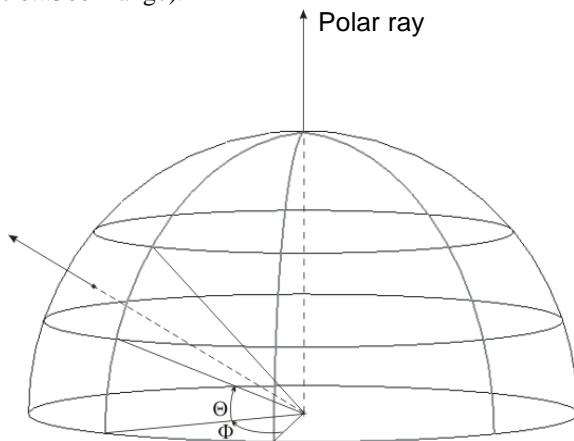


Fig.1.3Definition of rays emitted from cluster.

The total number of emitted rays is

$$N = (m - 1) \cdot n + 1,$$

where m is the number of different latitude values for the rays (including the polar ray),

n is the number of different longitude values ($n = 2$ for 2D case),

Θ and Φ are the zenith (latitudinal) and azimuth (longitudinal) angles, respectively.

The value of m is defined directly by the **View factor resolution level** which can be changed by the user via the **Calculation Control Options** dialog box. The value of n depends on m as follows: $n = m \cdot 4$.

The higher the View factor resolution level, the better the accuracy of the radiation heat transfer calculation, but the calculation time and required computer resources increase significantly when high values of View factor resolution level are specified.

Periodically during the calculation, a radiation ray is emitted in each of the solid angles in a direction that is defined randomly within this solid angle. These radiation rays are traced until intersection with either another radiative surface or the boundary of the

computational domain. To increase the accuracy of heat radiation calculation, the number of radiation rays emitted from each cluster can be increased automatically during the calculation, depending on the surface temperature and emissivity, to equalize the radiation heat emitting through the solid angles.

- When a radiation ray intercepts a cluster of other radiative surfaces, the radiation heat carried by this ray is uniformly distributed over the area of this cluster. The same procedure is performed if several radiation rays hit the same cluster. To smooth a possible non-uniformity of the incident radiation heat distribution over a radiative surface, a fraction of the radiation heat arriving with rays at a cluster can be transferred to the neighboring clusters also. In addition, small fluctuations are smoothed by the heat conduction in solid regions.

View Factor Calculation

The view factor between two clusters is the fraction of the total radiation energy emitted from one of the clusters that is intercepted by other clusters. The following relations are used in the code to define the view factor.

3D case

View factor for each ray (except for the polar ray) are defined as follows:

$$F_k = \frac{\varepsilon_k}{n}, \quad \varepsilon_k = (2k-1) \cdot \left[\frac{n}{(m-1) \cdot n + 1} \right]^2, \quad k = \overline{1, 2, \dots, m-1}.$$

View factor for the Polar ray is:

$$F_{polar} = 1 - \left[\frac{(m-1) \cdot n}{(m-1) \cdot n + 1} \right]^2.$$

2D case

$$F_k = \frac{\varepsilon_k}{2}, \quad \varepsilon_k = 2 \cdot \sin \left[\frac{\pi}{2 \cdot (2m-1)} \right] \cdot \sin \left[\frac{\pi}{2 \cdot (2m-1)} (2k-1) \right], \quad k = \overline{1, 2, \dots, m-1}.$$

$$F_{polar} = \cos \left[\frac{\pi \cdot (m-1)}{2m-1} \right].$$

Set of Equations

$$Q_{T,i} = \sum_k F_{i,k} q_{T,i,k} \text{ is the incident thermal radiation flux;}$$

$Q_{s,i} = \sum_k F_{i,k} q_{s,i,k}$ is the incident solar radiation flux;

$q_{t,k} - \rho_{t,k} \sum_k (F_{i,k} q_{t,i,k}) = \varepsilon_k \sigma T_k^4$ for thermal radiation;

$q_{s,k} - \rho_{s,k} \sum_k (F_{i,k} q_{s,i,k}) = 0$ for solar radiation.

Please note that for the sake of simplicity the set of equations described here defines the radiation heat transfer between clusters only and does not take into account the outer boundaries radiation and radiation sources such as environment, diffusive and solar radiation. In the full set of equations these sources are also considered.

Environment and Solar Radiation

Environmental and solar radiation can be applied to external and internal problems. In fact, the environment radiation is the non-directional energy flux generated by the walls of an imaginary huge "room" that surrounds the body. This flux has predefined radiation parameters.

In contrast to the environment radiation, the solar radiation is modeled by the directional energy flux. Therefore, the solar radiation is defined via its power flow (intensity) and its directional vector. In addition to the solar radiation from the computational domain boundaries, a solar radiation source emitting directional radiation can be specified.

The external radiation view factor can be calculated as $F = \sum_k F_k \cdot S$, where F_i are the view factors for the rays that have reached the boundaries of the computational domain, and S is the cluster area. Each solar radiation source produces one ray that follows the directional vector. After it reaches the outer boundary or the surface having appropriate radiation boundary condition, the view factor can be estimated as $F = \left(\overrightarrow{n_{solar}}, \overrightarrow{n_{clust}} \right) \cdot S$.

Discrete Ordinates



This feature is available for the HVAC module users only.

General Assumptions

- ☐ The whole 4π directional domain at any location within the computational domain is discretized into the specified number of equal solid angles.
- ☐ Radiation absorptive (semi-transparent) solids absorb and emit heat radiation in accordance with the specified solid material absorption coefficient. Scattering is not considered.

- Surfaces of opaque solids absorb the incident heat radiation in accordance with their specified emissivity coefficients, the rest incident radiation is reflected specularly or diffusively, or both specularly and diffusively, in accordance with the specified specularly coefficient.
- Radiation absorptive solids reflect radiation specularly, the radiation is refracted in accordance with the specified refraction indices of the solid and adjacent medium (another radiation absorptive solid, or a transparent solid or fluid, which refraction index is always considered as equal to 1). The refraction index value cannot exceed 4.

The Discrete Ordinates Method

In the discrete ordinates method the radiation transfer equation is solved for a set of discrete directions \vec{s} representing the directional domain of 4π at any position within the computational domain defined by the position vector \vec{r} . The directional domain is broken down into the specified number of equal solid angles or directions. The total number of directions is defined as:

$$N_{ord} = 8 \cdot \frac{RL \cdot (RL + 1)}{2}$$

where RL is the **Discretization level** specified by the user. Within each direction the radiation intensity is considered constant.

In the absence of scattering the radiation transfer equation can be written as:

$$\frac{dI(\vec{s}, \vec{r})}{ds} = \kappa \cdot [n^2 \cdot I_b(\vec{r}) - I(\vec{s}, \vec{r})] \quad (1.33)$$

where I is the radiation intensity per solid angle, $I_b = \frac{\sigma T^4}{\pi}$ is the blackbody radiation intensity, k is the medium absorption coefficient, n is the refraction index.

At the surfaces of opaque solids the incident heat radiation is absorbed depending on the specified emissivity coefficient, the rest of the incident radiation is reflected specularly or diffusively, or both specularly and diffusively. The surface specularly (f_s) defines the fraction of reflected radiation, which is reflected specularly, and the diffusively reflected fraction is determined as $(1 - f_s)$. The opaque surfaces can also emit heat radiation diffusively in accordance with the surface temperature and the specified emissivity coefficient.

The absorptive (semi-transparent) solids absorb heat radiation in accordance with the specified absorption coefficient. At the interface between two absorptive (semi-transparent) solids or between an absorptive solid and a fluid the incident radiation changes its direction in accordance with the Snell's law:

$$\frac{\sin \theta_2}{\sin \theta_1} = \frac{n_1}{n_2},$$

where n_1 and n_2 are the refractive indices of the first and second medium (n is always equal to 1 for a fully transparent solid or fluid) and θ_1 and θ_2 are the incident and refraction angles correspondingly.

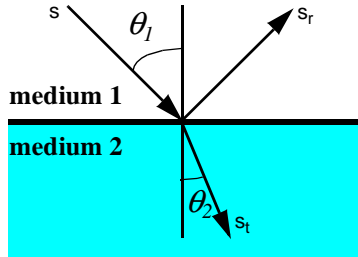


Fig.1.4 Radiation reflection at the interface between two absorptive media.

The radiation reflection at the interface between two absorptive (semi-transparent) solids or between an absorptive solid and a fluid follows the Fresnel's relation for unpolarized light:

$$\rho(\vec{s}) = \frac{1}{2} \left[\frac{\tan^2(\theta_1 - \theta_2)}{\tan^2(\theta_1 + \theta_2)} + \frac{\sin^2(\theta_1 - \theta_2)}{\sin^2(\theta_1 + \theta_2)} \right],$$

where ρ is the reflectivity which define the fraction of reflected radiation.

The fraction of radiation transmitted through the interface is defined as:

$$\tau = 1 - \rho.$$

Since all fluids are considered as transparent to heat radiation, the heat radiation propagates through them, as well as through transparent solids, without any interaction with them. However, as the heat radiation is traced through the computational domain by the discrete ordinates method, the "false scattering" effect caused by the discretization inaccuracies can appear - it is similar to the "numerical diffusion" effect in fluid flow calculations. Creating a finer computational mesh allows to reduce this effect.

When the radiation propagates from a small source to a significant distance, the "ray effect" can be encountered as a result of breaking down the directional domain into several directions. As radiation in these directions is traced from the source, it begin to demonstrate a ray-like behavior because more and more cells fall within the same direction with the distance and the radiation intensity distribution within the direction becomes non-uniform. This effect must be considered when decreasing the cell size to avoid the "false scattering" effect, so the discretization level must be increased if the finer mesh is used.

Radiation Spectrum



This feature is available for the HVAC module users only.

Spectrum can be specified for radiation from the computational domain boundaries and for radiation sources set on surfaces of opaque solids (representing openings). Specifying the spectrum for a radiation source or radiation from the far-field boundaries automatically selects the discrete ordinates method for calculating the radiative heat transfer.

The radiation spectrum is considered as consisting of several bands, which edges are specified by the user. Properties of radiation sources, surfaces and materials are considered constant within each band. The wavelength-dependent properties of solid materials are averaged over the specified spectrum bands, so it is recommended to specify the band edges at the wavelengths, at which the material properties change substantially.

If the radiation spectrum is considered, the equation (1.33) takes the following form:

$$\frac{dI_{\lambda_i}(\vec{s}, \vec{r})}{ds} = k_{\lambda_i} \cdot \left[n^2 \cdot I_{b,\lambda_i}(\vec{r}) - I_{\lambda_i}(\vec{s}, \vec{r}) \right] \quad (1.34)$$

where I_{λ_i} is the heat radiation intensity in the i -th spectrum band, I_{b,λ_i} is the intensity of the blackbody radiation in the i -th spectrum band, k_{λ_i} is the specified the medium absorption coefficient in the i -th spectrum band.

Radiative Surface and Radiation Source Types

Radiative Surfaces

Radiative surface or radiation source type	Specified values	Dependent values
Wall	ε, T, f_s	$\rho = 1 - \varepsilon, \alpha = \varepsilon, f_d = 1 - f_s$
Symmetry (ideal reflection)	No parameters	
Absorbent wall	No parameters	
Wall to ambient	ε, T, f_s	$\rho = 1 - \varepsilon, \alpha = \varepsilon, f_d = 1 - f_s$
Non-radiating	No parameters	

A radiative surface can only be specified on the surface of an opaque solid.

For the **Wall** and **Wall to ambient** boundary condition, the program gets T from the current results set.

The rays are emitted only from surfaces and boundaries on which the **Wall** or radiation source conditions are applied.

Surfaces with the specified **Absorbent wall** boundary condition are taken into account during the calculation but they can act as absorptive surfaces only. This wall type takes all heat from the radiation that reaches it and does not emit any heat.

The **Symmetry** boundary condition forces the walls to which it is applied to reflect rays as an ideal mirror.

Wall to ambient reproduces the most elementary phenomenon among the radiation effects. The walls with this condition does not interact with any other surfaces. They can only exhaust energy into the space that surrounds the computational domain. Heat flux from such surface could be calculated as:

$$Q = \sigma \cdot (T^4 - \epsilon_{out} \cdot T_{out}^4),$$


where T_{out} is the temperature of the environmental radiation.

When a ray reaches the surface of a radiation source or the **Wall to ambient** surface, it disappears. All energy carried by this ray also dies away.

Non-radiating boundary condition removes specific surfaces from the radiation heat transfer analysis, so they do not affect the results.



- The **Absorbent wall** and **Non-radiating surface** types of radiative surfaces are not consistent with the Discrete ordinates method, and are substituted in the calculation with **Whitebody wall**, which emissivity is considered equal to 0 (i.e. to that of whitebody), so that the surface fully reflects all the incident radiation (in accordance with the Lambert law) and does not emit any heat by itself.¹

1. Capabilities and features marked with  are available for the **HVAC** module users only.

Radiation Sources

Diffusive radiation source	Power (Q) or Intensity (I) or T and/or spectrum ^a
Solar radiation source	n , Power (Q) or Intensity (I) or T ^b

- a. The spectrum definition is available for the HVAC module users only.
- b. The spectrum of a solar radiation source is always the pre-defined **Daylight Spectrum** (available for the HVAC module users only).

A radiation source can only be specified on the surface of an opaque solid. Note that when calculating net radiation rate on such surface, radiation source is not accounted. All the incident radiation disappears without absorption or reflection on the radiation source surface, unless there is a radiative surface condition defined on the same surface.

The solar radiation source makes the wall to emit radiation like the outer solar radiation. It is specified by the direction vector and power or intensity or temperature. The solar radiation at the computational domain boundaries can be specified not only by the direction vector and intensity, but also by the location (on the surface of the Earth) and time.

Simultaneous Use of Radiative Surface and Radiation Source Conditions

The user can specify a radiative surface and radiation source on the same surface of an opaque solid. In this case the total heat radiation leaving the surface is determined as:

$$q = (1 - \mathcal{E}) q_i + \mathcal{E} \sigma T^4 + q_{source}$$

where: \mathcal{E} is the emissivity of the radiative surface, q_i is the incident heat radiation arriving on the surface, T is the surface temperature and q_{source} is the heat radiation emitted by the radiation source. Please note that the radiative surface emissivity coefficient and temperature do not influence the heat radiation emitted by the radiation source defined on the same surface - the radiation source properties are specified independently.

Viewing Results

The main result of the radiation heat transfer calculation is the solids' surface or internal temperatures. But these temperatures are also affected by heat conduction in solids and solid/fluid heat transfer. To see the results of radiation heat transfer calculation only, the user can view the **Leaving radiant flux** and distribution of **Net radiant flux** over the selected radiative surfaces at Surface Plots. User can also see the maximum, minimum, and average values of these parameters as well as the **Leaving radiation rate** and **Net radiation rate** as an integral over the selected surfaces in Surface Parameters. All these parameters can be viewed separately for the solar radiation and radiation from solar radiation sources (solar radiation) and the radiation from all other heat radiation sources (thermal radiation).

When the absorptive (semi-transparent) solids are considered, the additional parameters such as **Absorption volume radiant flux**, **Net volume radiant flow** and **Net volume radiant flux** become available both for the solar and thermal radiation, as well as for the total radiation and heat flux.

Flows in Porous Media

General Approach

Porous media are treated in Flow Simulation as distributed resistances to fluid flow, so they can not occupy the whole fluid region or fill the dead-end holes. In addition, if the **Heat conduction in solids** option is switched on, the heat transfer between the porous solid matrix and the fluid flowing through it is also considered. Therefore, the porous matrix act on the fluid flowing through it via the S_i , $S_i u_i$, and (if heat conduction in solids is considered) Q_H terms in Eqs. (1.2) and (1.3), whose components related to porosity are defined as:

$$S_i^{porous} = -k \delta_{ij} \rho u_j, \quad (1.35)$$

$$Q_H^{porosity} = \gamma \cdot (T_p - T) \quad (1.36)$$

where k is the resistance vector of the porous medium (see below), γ is the user-defined volumetric porous matrix/fluid heat transfer coefficient, T_p is the temperature of the porous matrix, T is temperature of the fluid flowing through the matrix, and the other designations are given in Section 1. In addition, the fluid density in Eqs. (1.1)-(1.3) is multiplied by the porosity n of the porous medium, which is the volume fraction of the interconnected pores with respect to the total medium volume.

In the employed porous medium model turbulence disappears within a porous medium and the flow becomes laminar.

If the heat conduction in porous matrix is considered, then, in addition to solving Eqs. (1.1)-(1.3) describing fluid flow in porous medium, an Eq. (1.28) describing the heat conduction in solids is also considered within the porous medium. In this equation the source Q_H due to heat transfer between the porous matrix and the fluid is defined in the same manner as in Eq. (1.36), but with the opposite sign. The values of γ and c for the porous matrix may differ from those of the corresponding bulk solid material and hence must be specified independently. Density of the solid material is multiplied by the solid volume fraction in the porous matrix, i.e. by $(1-n)$.

Thermal conductivity of the porous matrix can be specified as anisotropic in the same manner as for the solid material.

The conjugate heat transfer problem in a porous medium is solved under the following restrictions:

Governing Equations

- heat conduction in a porous medium not filled with a fluid is not considered,
- porous media are considered transparent for radiation heat transfer,
- heat sources in the porous matrix can be specified in the forms of heat generation rate or volumetric heat generation rate only; heat sources in a form of constant or time-dependent temperature can not be specified.

To perform a calculation in Flow Simulation, you have to specify the following porous medium properties: the effective **porosity** of the porous medium, defined as the volume fraction of the interconnected pores with respect to the total medium volume. Later on, the **permeability type** of the porous medium must be chosen among the following:

- isotropic (i.e., the medium permeability is independent of direction),
- unidirectional (i.e., the medium is permeable in one direction only),
- axisymmetrical (i.e., the medium permeability is fully governed by its axial and transversal components with respect to a specified direction),
- orthotropic (i.e., the general case, when the medium permeability varies with direction and is fully governed by its three components determined along three principal directions).

Then you have to specify some constants needed to determine the porous medium resistance to fluid flow, i.e., vector k defined as $k = - \text{grad}(P)/(\rho \cdot V)$, where P , ρ , and V are fluid pressure, density, and velocity, respectively. It is calculated according to one of the following formulae:

- $k = \Delta P \cdot S / (m \cdot L)$, where ΔP is the pressure difference between the opposite sides of a sample parallelepiped porous body, m is the mass flow rate through the body, S and L are the body cross-sectional area and length in the selected direction, respectively. You can specify ΔP as a function of m , whereas S and L are constants. Instead of mass flow rate you can specify volume flow rate, v . In this case Flow Simulation calculates $m = v \cdot \rho$. All these values do not specify the porous body for the calculation, but its resistance k only.
- $k = (A \cdot V + B) / \rho$, where V is the fluid velocity, A and B are constants, ρ is the fluid density. Here, only A and B are specified, since V and ρ are calculated.
- $k = \mu / (\rho \cdot D^2)$, where μ and ρ are the fluid dynamic viscosity and density, D is the reference pore size determined experimentally. Here, only D is specified, since μ and ρ are calculated.
- $k = \mu / (\rho \cdot D^2) \cdot f(Re)$, differing from the previous formula by the $f(Re)$ factor, yielding a more general formula. Here, in addition to D , $f(Re)$ as a formula dependency is specified.

To define a certain porous body, specify both the body position in the model and, if the porous medium has a unidirectional or axisymmetrical permeability, the reference directions in the porous body.

Perforated Plates in Boundary Conditions



This feature is available for the Electronics Cooling module users only.

A perforated plate is a particular case of porous media treated in Flow Simulation as distributed hydraulic resistances. Flow Simulation allows to specify a perforated plate as a special feature imposed on a pressure-opening- or fan-type flow boundary condition (see **"Boundary Conditions and Engineering Devices" on page 1-36**) via the **Perforated Plates** option. With the use of this feature, the user specifies a perforated plate via its porosity ε (defined as the fraction of the plate area covered by holes) and the holes' shape and size (holes may be either round with specified diameter, or rectangular with specified width and height, or regular polygons with specified side length and number of vertices). Then it can be assigned to any of the above mentioned flow boundary conditions as a distributed hydraulic resistance yielding the additional pressure drop at this boundary

$$\Delta p = -\zeta \cdot \frac{1}{2} \rho \cdot u^2, \quad (1.37)$$

where ρ is the fluid density, u is the fluid velocity inside the plate's holes, and ζ is the perforated plate's hydraulic resistance, calculated according to Ref. 2 from the plate porosity ε and the Reynolds number of the flow in the holes:

$$Re = \rho \cdot u \cdot D_h / \mu, \quad (1.38)$$

where $D_h = 4 \cdot F / \Pi$ is the hole hydraulic diameter defined via the area of a single hole F and its perimeter Π , and μ is the fluid's dynamic viscosity. Please note that the $\zeta(Re, \varepsilon)$ dependence taken from Ref. 2 and employed in Flow Simulation is valid for non-swirled, normal-to-plate flows only.

Cavitation

A liquid subjected to a low pressure below some threshold ruptures and forms vaporous cavities. More specifically, when the local pressure at a point in the liquid falls below the saturation pressure at the local temperature, the liquid undergoes phase transition and form cavities filled with the vapor with an addition of gas that has been dissolved in the liquid. This phenomenon is called cavitation.

The following models of cavitation are available in Flow Simulation:

- **Engineering cavitation model** (for pre-defined water only):
This model employs a homogeneous equilibrium approach and is available for pre-defined water only. It has the capability to account for the thermal effects.
- **Isothermal cavitation model:**
This model is based on the approach considering isothermal, two-phase flows. The isothermal cavitation model is only available for user-defined incompressible liquids.

Engineering cavitation model (for pre-defined water only)

The homogeneous equilibrium approach is employed. It is applicable for a variety of important industrial processes.

The fluid is assumed to be a homogeneous gas-liquid mixture with the gaseous phase consisting of the vapor and non-condensable (dissolved) gas. The vapor mass fraction is defined at the local equilibrium thermodynamic conditions. The dissolved gas mass fraction is a constant, which can be modified by user.

The velocities and temperatures of the gaseous (including vapor and non-condensable gas) and liquid phases are assumed to be the same.

The density of the gas-liquid mixture is calculated as:

$$\rho = \frac{1}{v}, \quad v = y_g \frac{R_{univ} T}{P \mu_g} + (1 - y_g - y_v) v_l(T, P) + y_v \frac{R_{univ} T z_v(T, P)}{P \mu_v},$$

where v is the specific volume of the gas-liquid mixture, v_l is the specific volume of liquid, $z_v(T, P)$ is the vapor compressibility ratio, R_{univ} is the universal gas constant, P is the local static pressure, T is the local temperature, y_v is the mass fraction of vapor, μ_v is the molar mass of vapor, y_g is the mass fraction of the non-condensable gas; μ_g is the molar mass of the non-condensable gas. The properties of the dissolved non-condensable gas are set to be equal to those of air. By default, the mass fraction of non-condensable gas is set to 10^{-4} . This is a typical model value appropriated in most cases but it can be modified by the user in the range of $10^{-3} \dots 10^{-5}$.

The mass fraction of vapor y_v is computed numerically from the following non-linear equation for the full enthalpy gas-liquid mixture:

$$H = y_g h_g(T, P) + (1 - y_g - y_v) h_l(T, P) + y_v h_v(T, P) + \frac{I_c v^2}{2} + \frac{5}{2} k,$$

where temperature of the mixture T is a function of pressure P and y_v . Here h_g , h_l , h_v are the enthalpies of non-condensable gas, liquid and vapor, respectively, k is the turbulent energy,

$$I_c = (\rho u_x)^2 + (\rho u_y)^2 + (\rho u_z)^2 \text{ is the squared impulse.}$$

The model has the following limitations and recommendations:

- Cavitation is available only for pre-defined water (when defining the project fluids you should select **Water** from the list of **Pre-Defined** liquids).
- For mixtures of different liquids the cavitation option cannot be selected.

- The temperature and pressure ranges in the cavitation area must be within the following bounds:
 $T = 280 - 583.15 \text{ K}$, $P = 800 - 10^7 \text{ Pa}$.
- The model does not describe the detailed structure of the cavitation area, i.e. parameters of individual vapor bubbles.
- The volume fraction of vapor is limited by 0.95. The parameters of the flow at the inlet boundary conditions must satisfy this requirement.
- The **Cavitation** option is not applicable if you calculate a water flow in the model without flow openings (inlet and outlet).
- The fluid region where cavitation occurs must be well resolved by the computational mesh.
- If the calculation has finished or has been stopped and the **Cavitation** option has been enabled or disabled, the calculation cannot be resumed or continued and must be restarted from the beginning.

Isothermal cavitation model

This model provides a capability to analyze two-phase flows of industrial liquids which thermophysical properties are not described in details.

In the isothermal cavitation model the following assumptions are made:

- The process temperature is constant and the thermal effects are not considered.
- The liquid phase is an incompressible fluid.
- When liquid turns into vapor completely the vapor and non-condensable gas density is defined by the ideal gas law.
- The fluid contains non-condensable (dissolved) gas. One of the four gases can be used as dissolved gas: Air, Carbon dioxide, Helium and Methane. By default, the non-condensable gas is Air and the mass fraction is set to 10^{-4} . This is a typical model value appropriated in most cases but it can be modified by the user in the range of $10^{-2} \dots 10^{-6}$.

The density of the gas-liquid mixture is calculated as:

$$\rho = \frac{P - P_0^E(T_0)}{R_{univ} T_0} \frac{\mu_g}{y_g}, \quad P_V \leq P \leq P_L$$

where R_{univ} is the universal gas constant, P is the local static pressure, P_L is the local static pressure at which the vapor appears, P_V is the local static pressure at which the liquid turns into the vapor completely, T_0 is the local temperature, P_0^E is the saturation pressure at T_0 , y_g is the mass fraction of the non-condensable gas; μ_g is the molar mass of the non-condensable gas.

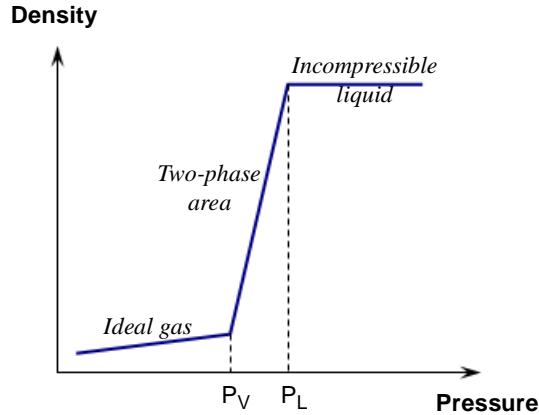


Fig.1.4 Density-pressure phase diagram

Two-phase (fluid + particles) Flows

Flow Simulation calculates two-phase flows as a motion of spherical liquid particles (droplets) or spherical solid particles in a steady-state flow field. Flow Simulation can simulate dilute two-phase flows only, where the particle's influence on the fluid flow (including its temperature) is negligible (e.g. flows of gases or liquids contaminated with particles). Generally, in this case the particles mass flow rate should be lower than about 30% of the fluid mass flow rate.

The particles of a specified (liquid or solid) material and constant mass are assumed to be spherical. Their drag coefficient is calculated with Henderson's formula (Ref. 3), derived for continuum and rarefied, subsonic and supersonic, laminar, transient, and turbulent flows over the particles, and taking into account the temperature difference between the fluid and the particle. The particle/fluid heat transfer coefficient is calculated with the formula proposed in Ref. 4. If necessary, the gravity is taken into account. Since the particle mass is assumed constant, the particles cooled or heated by the surrounding fluid change their size. The interaction of particles with the model surfaces is taken into account by specifying either full absorption of the particles (that is typical for liquid droplets impinging on surfaces at low or moderate velocities) or ideal or non-ideal reflection (that is typical for solid particles). The ideal reflection denotes that in the impinging plane defined by the particle velocity vector and the surface normal at the impingement point, the particle velocity component tangent to surface is conserved, whereas the particle velocity component normal to surface changes its sign. A non-ideal reflection is specified by the two particle velocity restitution (reflection) coefficients, e_n and e_τ , determining values of these particle velocity components after reflection, $V_{2,n}$ and $V_{2,\tau}$, as their ratio to the ones before the impingement, $V_{1,n}$ and $V_{1,\tau}$:

$$e_n = \frac{V_{2,n}}{V_{1,n}} \quad e_\tau = \frac{V_{2,\tau}}{V_{1,\tau}}$$

As a result of particles impingement on a solid surface, the total erosion mass rate, $R_{\Sigma erosion}$, and the total accretion mass rate, $R_{\Sigma accretion}$, are determined as follows:

$$R_{\Sigma erosion} = \sum_{i=1}^N \int_{M_{pi}} K_i \cdot V_{pi}^b \cdot f_{1i}(\alpha_{pi}) \cdot f_{2i}(d_{pi}) d\dot{m}_{pi},$$

$$R_{\Sigma accretion} = \sum_{i=1}^N M_{pi},$$

where:

N is the number of fractions of particles specified by user as injections in Flow Simulation (the user may specify several fractions of particles, also called injections, so that the particle properties at inlet, i.e. temperature, velocity, diameter, mass flow rate, and material, are constant within one fraction),

i is the fraction number,

M_{pi} is the mass impinging on the model walls in unit time for the i -th particle fraction,

K_i is the impingement erosion coefficient specified by user for the i -th particle fraction,

V_{pi} is the impingement velocity for the i -th particle fraction,

b is the user-specified velocity exponent ($b = 2$ is recommended),

$f_{1i}(\alpha_{pi})$ is the user-specified dimensionless function of particle impingement angle α_{pi} ,

$f_{2i}(d_{pi})$ is the user-specified dimensionless function of particle diameter d_{pi} .

Boundary Conditions and Engineering Devices

Internal Flow Boundary Conditions

For internal flows, i.e., flows inside models, Flow Simulation offers the following two options of specifying the flow boundary conditions: manually at the model inlets and outlets (i.e. model openings), or to specify them by transferring the results obtained in another Flow Simulation calculation in the same coordinate system (if necessary, the calculation can be performed with another model, the only requirement is the flow regions at the boundaries must coincide).

With the first option, all the model openings are classified into "**pressure**" openings, "**flow**" openings, and "**fans**", depending on the flow boundary conditions which you intend to specify on them.

A "**pressure**" opening boundary condition, which can be static pressure, or total pressure, or environment pressure is imposed in the general case when the flow direction and/or magnitude at the model opening are not known a priori, so they are to be calculated as part of the solution. Which of these parameters is specified depends on which one of them is known. In most cases the static pressure is not known, whereas if the opening connects the computational domain to an external space with known pressure, the total pressure at the opening is known. The Environment pressure condition is interpreted by Flow Simulation as a total pressure for incoming flows and as a static pressure for outgoing flows. If, during calculation, a vortex crosses an opening with the Environment pressure condition specified at it, this pressure considered as the total pressure at the part of opening through which the flow enters the model and as the static pressure at the part of opening through which the flow leaves the model.

Note that when inlet flow occurs at the "pressure" opening, the temperature, fluid mixture composition and turbulence parameters have to be specified also.

A "**flow**" opening boundary condition is imposed when dynamic flow properties (i.e., the flow direction and mass/volume flow rate or velocity/ Mach number) are known at the opening. If the flow enters the model, then the inlet temperature, fluid mixture composition and turbulence parameters must be specified also. The pressure at the opening will be determined as part of the solution. For supersonic flows the inlet pressure must be specified also.

A "**fan**" condition simulates a fan installed at a model opening. In this case the dependency of volume flow rate on pressure drop over the fan is prescribed at the opening. These dependencies are commonly provided in the technical documentation for the fans being simulated.

With the second option, you specify the boundary conditions by transferring the results obtained in another Flow Simulation calculation in the same coordinate system. If necessary, the calculation can be performed with another model, the only requirement is the flow regions at the boundaries must coincide. At that, you select the created boundary conditions' type: either as for external flows (so-called "ambient" conditions, see the next Section), or as for "*pressure*" or "*flow*" openings, see above. If a conjugate heat transfer problem is solved, the temperature at the part of the boundary lying in a solid body is transferred from the other calculation.

Naturally, the flow boundary conditions specified for an internal flow problem with the first and/or second options must be physically consistent with each other, so it is expedient to specify at least one "pressure"-type boundary condition and at least one "flow"-type boundary condition, if not only "ambient" boundary conditions are specified.

External Flow Boundary Conditions

For external problems such as flow over an aircraft or building, the parameters of the external incoming flow (so-called "ambient" conditions) must be defined. Namely the velocity, pressure, temperature, fluid mixture composition and turbulence parameters must be specified. Evidently, during the calculation they can be partly violated at the flow boundary lying downstream of the model.

Wall Boundary Conditions

In Flow Simulation the *default* velocity boundary condition at solid walls corresponds to the well-known *no-slip* condition. The solid walls are also considered to be *impermeable*. In addition, the wall surface's translation and/or rotation (without changing the model's geometry) can be specified. If a calculation is performed in a rotating coordinate system, then some of the wall surfaces can be specified as stationary, i.e. a backward rotation in this coordinate system (without changing the model geometry). Flow Simulation also provides the "*Ideal Wall*" condition that corresponds to the well-known slip condition. For example, Ideal Walls can be used to model planes of flow symmetry.

If the flow of non-Newtonian liquids is considered, then the following *slip* condition at all solid walls can be specified for each non-Newtonian liquid in the project separately: if the shear stress τ exceeds the yield stress value $\tau_{0,slip}$, then

a slip velocity v_{slip} is determined from $v_{slip} = C_1 (\phi - \phi_{0,slip})^{C_2}$, where C_1 and C_2 , as well as $\tau_{0,slip}$, are specified by user.

If conjugate heat transfer in fluid and solid media is not considered, one of the following boundary conditions can be imposed at solid walls: either the wall temperature

$$T = T_w, \quad (1.39)$$

Governing Equations

or the heat flux,

$$q = q_w \quad (1.40)$$

being positive for heat flows from fluid to solid, equal to zero for adiabatic (heat-insulated) walls, and negative for heat flows from solid to fluid.

When considering conjugate heat transfer in fluid and solid media, the heat exchange between fluid and solid is calculated by Flow Simulation, so heat wall boundary conditions are not specified at the walls.

Internal Flow Boundary Conditions

If one or several non-intersecting axisymmetric rotating regions (local rotating reference frames) are specified, the flow parameters are transferred from the adjacent fluid regions and circumferentially averaged over rotating regions' boundaries as boundary conditions.

Periodic Boundary Conditions

The "*periodicity*" condition may be applied if the model consist of identical geometrical features arranged in periodic linear order. Periodic boundary conditions are specified at the pair of computational domain boundaries for the selected direction in which a geometrical feature or a group of features repeats regularly over distance. Periodic boundary conditions allows to reduce the analysis time by calculating the fluid flow only for a small group of identical geometrical features or even just for one feature, but taking into account influence of other identical features in the pattern. Please note that the number of basic mesh cells along the direction in which the "*periodicity*" condition is applied must be no less than five.

Heat Pipes



This feature is available for the Electronics Cooling module users only.

"Heat Pipe" is a device (of arbitrary form: a tube, a plate, etc.) transferring heat from its hotter surface to its colder surface due to evaporating a liquid (water, etc.) and condensing its vapor in this device's inner hollow. This liquid evaporates near this hollow's hotter surface and its vapor condensates near this hollow's colder surface. The condensed liquid then returns to the hotter end due to gravity or by a wick. If such a device operates under its design conditions, the heat transfer rate provided by this device exceeds substantially any value achievable by a solid body of similar dimensions.

In Flow Simulation a "Heat Pipe" is modeled simplistically as an extremely heat-conducting body. To model real efficiency of a heat pipe, a non-zero thermal resistance can be assigned to it.

Thermal Joint

A thermal joint model implemented in Flow Simulation can be used to simplify the heat transfer simulation from one (hot) surface S_1 to the other (cold) surface S_2 with the actual thermal joint geometry excluded from the analysis. Here, to simulate heat transfer between these surfaces, the value of contact resistance θ (or its reciprocal, heat transfer coefficient α) is used. The resulting heat transfer rate from the hot surface to the cold surface is calculated as $Q = \alpha \cdot (T_1 - T_2)$, where T_1 and T_2 are the temperatures of the surfaces S_1 and S_2 .

Notice that once you select the faces to specify thermal joint between them, these faces become thermally insulated in respect to the surrounding medium and only participate in the heat exchange between each other.

Two-resistor Components



This feature is available for the Electronics Cooling module users only.

A two-resistor model implemented in Flow Simulation can be used for simplified solving of heat transfer problems in an electronic device with small electronic packages (chips, etc.). A small package is considered as consisting of two flat solid plates: **Junction** and **Case**, which are mounted on the **Board** (see Fig.1.5). The junction represents a die or a chip. The case represents the die's case. The heat conduction through the chip is calculated using the user-specified junction-to-case Q_{jc} (from the junction to the top surface of the package) and junction-to-board Q_{jb} (from the junction to the board on which it is mounted) thermal resistances (in K/W in SI). The Junction and Case plates are modeled as a high conductivity bodies with heat-insulating side walls, so the only Case's top and Junction's bottom transfer heat to the surroundings.

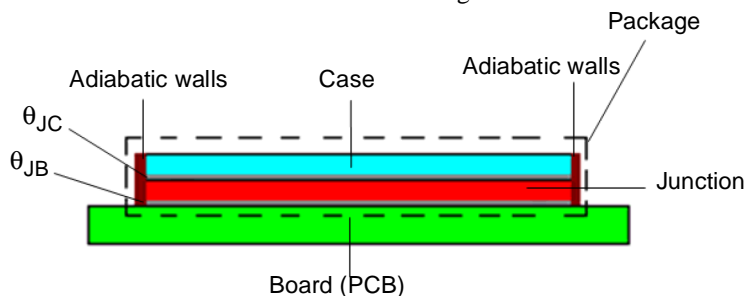


Fig.1.5 Flow Simulation representation of the two-resistor model.

Thermoelectric Coolers

Thermoelectric cooler (TEC) is a flat sandwich consisting of two plates covering a circuit of p-n semiconductor junctions inside. When a direct electric current (DC) i runs through this circuit, in accordance with the Peltier effect the $a \cdot i \cdot T_c$ heat, where a is the Seebeck coefficient, T_c is the TEC's "cold" surface temperature, is pumped from the TEC's "cold" surface to its "hot" surface (the "cold" and "hot" sides are determined from the DC direction). This heat pumping is naturally accompanied by the Joule (ohmic) heat release at both the TEC surfaces and the heat transfer from the hotter side to the colder (reverse to the Peltier effect). The ohmic heat release is defined as $R \cdot i^2 / 2$, where R is the TEC's electric resistance, while the heat transfer is defined as $k \cdot \Delta T$, where k is the TEC's thermal conductivity, $\Delta T = T_h - T_c$, T_h is the TEC's "hot" surface temperature. The net heat transferred from the TEC's "cold" surface to its "hot" surface, Q_c , is equal to

$$Q_c = a \cdot i \cdot T_c - R \cdot i^2 / 2 - k \cdot \Delta T ,$$

Correspondingly, the net heat released at the TEC's "hot" surface, Q_h , is equal to

$$Q_h = a \cdot i \cdot T_h + R \cdot i^2 / 2 - k \cdot \Delta T .$$

In Flow Simulation a TEC is specified by selecting a flat plate (box) in the model, assigning its "hot" face, and applying one of the TECs already defined by user in the Engineering Database. The following characteristics of TEC are specified in the Engineering Database:

- the maximum DC current, i_{max}
- the maximum heat Q_{cmax} transferred at this i_{max} at $\Delta T = 0$
- the maximum temperature difference ΔT_{max} , attained at $Q_c = 0$
- the voltage V_{max} corresponding to i_{max}

All of these characteristics are specified for two T_h values, in accordance with the information usually provided by the TEC suppliers. Proceeding from these characteristics, the $a(T)$, $R(T)$, and $k(T)$ linear functions are determined. The functional boundary conditions are specified automatically on the TEC's "cold" and "hot" surfaces, which must be free from other boundary conditions.

The temperature solution inside the TEC and on its surfaces is obtained using a special procedure differing from the standard Flow Simulation calculation procedure for heat conduction in solids.

The TEC's "hot" face must be in contact with other solids, i.e it must not be in contact with any fluid. In addition, it is required that the obtained TEC solution, i.e. T_h and ΔT , lie within the TEC's operating range specified by its manufacturer.

Local Mean Age

Local mean age (LMA) is the average time τ for fluid to travel from the selected inlet opening to the point with taking both the velocity and the diffusion into account. It is determined by solving the following equation:

$$\sum_{i=1}^3 \frac{\partial}{\partial x_i} \left(\rho \tau u_i - \left(\frac{\mu}{\sigma} + \frac{\mu_t}{\sigma_t} \right) \frac{\partial \tau}{\partial x_i} \right) = \rho ,$$

where x_i is the i -th coordinate, ρ is the density, u_i is the i -th velocity component, μ is the dynamic viscosity coefficient, μ_t is the turbulent eddy viscosity coefficient, σ and σ_t are the laminar and turbulent Schmidt numbers. The equation is solved under the $\tau = 0$ boundary condition on the inlet opening.

Dimensionless LMA is the LMA divided by the V/Q ratio, where V is the computational domain fluid volume, Q is the volume flow rate of the air entering this fluid volume.

LACI (Local Air Change Index) is equal to $1/(\text{Dimensionless LMA})$, i.e. reciprocal to the Dimensionless LMA.

By default, the calculation of these parameters is disabled. You can enable the calculation of LMA, Dimensionless LMA and LACI in the Calculation Control Options.

Comfort Parameters



These parameters are available for the HVAC module users only.

Flow Simulation has the capability to predict the general thermal sensation, degree of discomfort (thermal dissatisfaction) of people exposed to moderate thermal environments and estimate air quality by calculating comfort criteria (Ref. 5, Ref. 6, Ref. 7). These criteria are used when designing occupied spaces and their HVAC systems and are intended to determine whether environmental conditions are acceptable in terms of general thermal comfort and air quality or represent discomfort. The calculation of the comfort criteria assumes that the analyzed fluid is Air.

Mean Radiant Temperature (MRT) is the uniform surface temperature of an imaginary black enclosure in which an occupant would exchange the same amount of radiant heat as in the actual non-uniform space.

The mean radiant temperature T_r is defined as follows:

$$T_r^4 = \frac{1}{4\sigma} \int I_{diffuse}(\Omega) d\Omega + \frac{1}{4\sigma} \sum I_{sun} ,$$

Governing Equations

where $I_{diffuse}$ is the intensity of the diffuse (thermal) radiation ($W/m^2/rad$), I_{sun} is the intensity of the solar radiation (W/m^2), σ is the Stefan-Boltzmann constant.

To calculate the Mean Radiant Temperature, it is assumed that the emissivity of all the surfaces within the computational domain equals to unity.

Operative Temperature is the uniform temperature of an imaginary black enclosure, in which an occupant would exchange the same amount of heat by radiation plus convection as in the actual non-uniform environment.

The operative temperature T_c is defined as follows (Ref. 6):

$$T_c = \frac{T_r + T\sqrt{10V}}{1 + \sqrt{10V}},$$

where T_r is the mean radiant temperature ($^{\circ}C$), T is the fluid temperature ($^{\circ}C$), V is the fluid velocity (m/s).

Predicted Mean Vote (PMV) is an index that predicts the mean value of the votes of a large group of persons on the 7-point thermal sensation scale, based on the heat balance of the human body. Thermal balance is obtained when the internal heat production in the body is equal to the loss of heat to the environment. In a moderate environment, the human thermoregulatory system will automatically attempt to modify skin temperature and sweat secretion to maintain heat balance (Ref. 7).

cold	cool	slightly cool	neutral	slightly warm	warm	hot
-3	-2	-1	0	+1	+2	+3

The *PMV* is defined as follows:

$$PMV = (0.303e^{-0.036M} + 0.028) \cdot \left\{ \begin{aligned} &[(M - W) - 3.05 \cdot 10^{-3} [5733 - 6.99(M - W) - p_a]] \\ &- 0.42[(M - W) - 58.15] - 1.7 \cdot 10^{-5} M(5867 - p_a) - 0.0014M(34 - T_a) \\ &- 3.96 \cdot 10^{-8} f_{cl} [(T_{cl} + 273)^4 - (T_r + 273)^4] - f_{cl} h_c (T_{cl} - T_a) \end{aligned} \right\},$$

where

$$T_{cl} = 35.7 - 0.028(M - W) - I_{cl} \{ 3.96 \cdot 10^{-8} f_{cl} [(T_{cl} + 273)^4 - (T_r + 273)^4] + f_{cl} h_c (T_{cl} - T_a) \},$$

$$h_c = \max\{2.38(T_{cl} - T_a)^{0.25}, 12.1\sqrt{V}\}$$

$$f_{cl} = \begin{cases} 1.00 + 1.29I_{cl}, & \text{for } I_{cl} \leq 0.078 \frac{m^2}{kW} \\ 1.05 + 0.645I_{cl}, & \text{for } I_{cl} > 0.078 \frac{m^2}{kW} \end{cases},$$

where

M is the metabolic rate (W/m^2 of the body area).

It is the rate of transformation of chemical energy into heat and mechanical work by metabolic activities within an organism;

W is the external work (W/m^2 of the body area). It accounts for the effective mechanical power;

I_{cl} is the clothing thermal resistance (m^2K/W).

It is the resistance to sensible heat transfer provided by a clothing ensemble. The definition of clothing insulation relates to heat transfer from the whole body and, thus, also includes the uncovered parts of the body, such as head and hands. The typical values of thermal resistance for a certain clothing ensemble can be found in Ref. 7;

f_{cl} is the ratio of clothed surface area to nude surface area;

T_a is the air temperature ($^{\circ}C$);

T_r is the mean radiant temperature ($^{\circ}C$);

V is the relative air velocity (m/s);

p_a is the water vapor partial pressure (Pa) calculated in accordance with the saturation curve, the air temperature T_a and the Relative humidity (see "**Equilibrium volume condensation of water from steam**" on page 1-14);

h_c is the convective heat transfer coefficient ($W/m^2/K$);

T_{cl} is the clothing surface temperature ($^{\circ}C$).

Predicted Percent Dissatisfied (PPD) is an index that provides information on thermal discomfort or thermal dissatisfaction by predicting the percentage of people likely to feel too warm or too cool in a given environment (Ref. 7). It can be obtained from the PMV using the following equation:

$$PPD = 100 - 95 \exp(-0.03353 PMV^4 - 0.2179 PMV^2).$$

Draught Rate is the percentage of people predicted to be bothered by draught. The draught rate DR is defined as follows:

Governing Equations

$$DR = (34 - T_{a,l}) (\bar{v}_{a,l} - 0.05)^{0.62} (0.37 \cdot \bar{v}_{a,l} \cdot Tu + 3.14),$$

For $\bar{v}_{a,l} < 0.05$ m/s : $\bar{v}_{a,l} = 0.05$ m / s

For $T_{a,l} > 34^\circ\text{C}$: $T_{a,l} = 34^\circ\text{C}$

For $DR > 100\%$: $DR = 100\%$

where

$T_{a,l}$ is the local air temperature ($^\circ\text{C}$), 20°C to 26°C ;

$v_{a,l}$ is the local mean air velocity (m/s), < 0.5 m/s;

Tu is the local turbulence intensity (%), 10% to 60% . If the **Laminar Only** flow type is selected, Tu equals 40% .

This model applies to people at light, mainly sedentary activity with a thermal sensation for the whole body close to neutral and for prediction of draught at the neck. At the level of arms and feet, the model could overestimate the predicted draught rate. The sensation of draught is lower at activities higher than sedentary (> 1.2 met) and for people feeling warmer than neutral.

Draft Temperature is the difference in temperature between any point in the occupied zone and the control condition. "Draft" is defined as any localized feeling of coolness or warmth of any portion of the body due to both air movement and air temperature, with humidity and radiation considered constant. (Ref. 5).

The draft temperature T_d is defined as follows:

$$T_d = T - T_m - 7.6553 (V - 0.1524),$$

where:

T is the local fluid temperature ($^\circ\text{C}$);

T_m is the average fluid temperature within the control space ($^\circ\text{C}$);

V is the local fluid velocity (m/s).

Air Diffusion Performance Index (ADPI) is the percentage of the space in which the air speed is less than 0.35 m/s and the Draft Temperature falls between -1.7°C and 1.1°C (Ref. 5).

If the Draft Temperature or ADPI are calculated in Volume Parameters, then the "control space" will correspond to the specified volume region. In all other cases the "control space" corresponds to the whole computational domain.

Contaminant Removal Effectiveness (CRE) is an index that provides information on the effectiveness of a ventilation system in removing contaminated air from the whole space. For a perfect mixing system $\text{CRE}=1$. Values above 1 are good, values below 1 are poor.

This parameter is only available if more than one fluid is present in the control space.

Its value is defined as follows:

$$CRE = \frac{C_e}{<C>},$$

where:

C_e is the bulk average mass fraction of the contaminant calculated over all faces through which the fluids outflow from the computational domain;

$<C>$ is the bulk average mass fraction of the contaminant calculated over the whole computational domain.

Local Air Quality Index (LAQI) is an index that provides information on the effectiveness of a ventilation system in removing contaminated air from a point. For a perfect mixing system LAQI =1. For other systems, the higher the value at a point, the better the capability of the ventilation system in removing contaminated air from that point. This parameter is only available if more than one fluid is present in the control space. Its value is defined as follows:

$$LAQI = \frac{C_e}{C},$$

where:

C_e is the bulk average mass fraction of the contaminant calculated over all faces through which the fluids outflow from the computational domain;

C is the mass fraction of the contaminant at a point.

The Flow Angle shows the flow deviation from the design flow direction. Consider one of the axis of selected coordinate system as the design flow direction, the results can then be viewed as the deviation from the design. Typically, flow angles of less than 15° might be considered as good.

The flow angle components are defined as follows:

$$\text{Angle (X)} = \arccos(V_x/V)$$

$$\text{Angle (Y)} = \arccos(V_y/V),$$

$$\text{Angle (Z)} = \arccos(V_z/V)$$

where V_x , V_y , V_z are the X, Y, and Z components of the fluid velocity and V is the absolute value of the fluid velocity vector.

Tracer Study



This feature is available for the HVAC module users only.

Governing Equations

If a gaseous (or liquid) substance (e.g. a contaminant) diffuses in a gaseous (or liquid) fluid (if this fluid flows and carries this substance, this fluid is usually named the carrier fluid) and this substance's mass fraction y in the carrier fluid is too small, i.e. $y \ll 1$, so it can not influence the carrier fluid flow's properties (velocity, pressure, temperature), then distribution of this substance over the computational domain due to carrying it by the fluid flow and its diffusion in this fluid can be calculated with the **Tracer Study** option.

According to this option, this substance's diffusion is calculated in the previously calculated steady-state or unsteady carrier fluid flow by solving the following Tracer Study equation taking the substance's concentration non-uniformity and the carrier fluid flow's pressure gradient (for gaseous fluids only) into account:

$$\frac{\partial \rho y}{\partial t} + \frac{\partial}{\partial x_i} \left[\rho y u_i - \frac{\rho R T}{p m} \left(\frac{\mu}{Pr \cdot Le} + \frac{\mu_t}{Pr_t \cdot Le_t} \right) \frac{\partial y}{\partial x_i} \right] = \frac{\partial}{\partial x_i} \frac{m_1 m_2}{m^2} \left[\frac{\rho y v_1 - y}{p} \left(\frac{\mu}{Pr \cdot Le} + \frac{\mu_t}{Pr_t \cdot Le_t} \right) \frac{\partial p}{\partial x_i} \right],$$

where

ρ is the carrier fluid and the substance's mixture density (since $y \ll 1$, ρ can be considered as the carrier fluid's density),

t is time,

x_i is the i -th component of the used coordinate system,

u_i is the i -th component of the carrier fluid's velocity (the substance has the same velocity),

p is the carrier fluid's static pressure,

R is the universal gas constant,

m is the carrier fluid and the substance's mixture molar mass,

m_1 is the substance's molar mass,

m_2 is the carrier fluid's molar mass,

v_1 is the substance's specific volume,

μ is the carrier fluid's laminar viscosity,

μ_t is the carrier fluid's turbulent viscosity,

Pr, Pr_t are the carrier fluid's laminar and turbulent Prandtl numbers,

Le, Le_t are the carrier fluid's laminar and turbulent Lewis numbers.

The Tracer Study equation is solved after finishing the carrier fluid flow calculation, i.e. in the postprocessor, either as steady-state or as unsteady (time-dependent, with its own time).

The substance's physical properties required to solve the Tracer Study equation are specified in the **Engineering Database** as the substance's molar mass (m_I), binary (this

substance in the carrier fluid) diffusion coefficient $D = \frac{\mu}{Pr \cdot Le}$ ($D_t = \frac{\mu_t}{Pr_t \cdot Le_t} = D$ is

assumed) or Lewis number Le ($Le_t = Le$, $Pr_t = Pr$, $\mu_t = \mu$ are assumed), and saturation pressure curve vs. temperature (optional).

The Tracer Study equation is solved in the computational domain (or its subdomain) with the user-specified boundary conditions, initial conditions, and volume sources of the substance carried by the fluid flow. The substance's boundary conditions are superimposed on the carrier fluid flow boundary conditions and consist of the substance's surface sources and wall condition specified on the user-selected surfaces. The substance's surface sources are specified by the substance's mass fraction, or mass flow rate, or specific (i.e. per unit surface area) mass flow rate, or evaporation on the user-selected walls and/or by the substance's mass fraction on the user-selected inlet flow openings. At that the substance's evaporation can be specified (by enabling the **Liquid Surface** option) only for those substances whose saturation pressure curve has been specified in the **Engineering Database**. The substance's wall condition is the substance's condensation calculated on the user-selected model walls (only for those substances whose saturation pressure curve has been specified in the **Engineering Database**).

The substance's volume sources are specified by the substance's mass fraction, or mass generation rate (total over the source volume), or volumetric (i.e. per unit volume) mass generation rate in the user-selected fluid volumes.

To solve the Tracer Study equation the user must also specify the substance's initial conditions in the form of the substance's mass fraction (it may be zero) distribution over the computational domain (or its subdomain).

As a result of the Tracer Study calculation you can see the substance's mass fraction, mass flow rates (through the user-selected surfaces or in the user-selected volumes), CRE and LAQI (see **Comfort Parameters** above) distributions over the computational domain (or its subdomain).

The Tracer Study can be performed simultaneously for several substances in the same fluid flow carrying them.

Numerical Solution Technique

The numerical solution technique employed in Flow Simulation is robust and reliable, so it does not require any user knowledge about the computational mesh and the numerical methods employed. But sometimes, if the model and/or the problem being solved are too complicated, so that the Flow Simulation standard numerical solution technique requires extremely high computer resources (memory and/or CPU time) which are not available, it is expedient to employ Flow Simulation options which allow the adjustment of the automatically specified values of parameters governing the numerical solution technique. To employ these options properly and successfully, take into account the information presented below about Flow Simulation' numerical solution technique.

Briefly, Flow Simulation solves the governing equations with the finite volume (FV) method on a spatially rectangular computational mesh designed in the Cartesian coordinate system with the planes orthogonal to its axes and refined locally at the solid/fluid interface and, if necessary, additionally in specified fluid regions, at the solid/solid surfaces, and in the fluid region during calculation. Values of all the physical variables are stored at the mesh cell centers. Due to the FV method, the governing equations are discretized in a conservative form. The spatial derivatives are approximated with implicit difference operators of second-order accuracy. The time derivatives are approximated with an implicit first-order Euler scheme. The viscosity of the numerical scheme is negligible with respect to the fluid viscosity.

Computational Mesh

Flow Simulation computational mesh is rectangular everywhere in the computational domain, so the mesh cells' sides are orthogonal to the specified axes of the Cartesian coordinate system and are not fitted to the solid/fluid interface. As a result, the solid/fluid interface cuts the near-wall mesh cells. Nevertheless, due to special measures, the mass and heat fluxes are treated properly in these cells named **partial**.

The rectangular **computational domain** is automatically constructed (may be changed manually), so it encloses the solid body and has the boundary planes orthogonal to the specified axes of the Cartesian coordinate system. Then, the computational mesh is constructed in the following several stages.

First of all, a **basic mesh** is constructed. For that, the computational domain is divided into slices by the basic mesh planes, which are evidently orthogonal to the axes of the Cartesian coordinate system. The user can specify the number and spacing of these planes along each of the axes. The so-called control planes whose position is specified by user can be among these planes also. The basic mesh is determined solely by the computational domain and does not depend on the solid/fluid interfaces.

Then, the basic mesh cells intersecting with the solid/fluid interface are split uniformly into smaller cells in order to **capture the solid/fluid interface** with mesh cells of the specified size (with respect to the basic mesh cells). The following procedure is employed: each of the basic mesh cells intersecting with the solid/fluid interface is split uniformly into 8 child cells; each of the child cells intersecting with the interface is in turn split into 8 cells of next level, and so on, until the specified cell size is attained.

At the next stage of meshing, the mesh obtained at the solid/fluid interface with the previous procedure is refined (i.e. the cells are split further or probably merged) in accordance with **the solid/fluid interface curvature**. The criterion to be satisfied is established as follows: the maximum angle between the normals to the surface inside one cell should not exceeds certain threshold, otherwise the cell is split into 8 cells.

Finally, the mesh obtained with these procedures is refined in the computational domain to satisfy the so-called **narrow channel** criterion: for each cell lying at the solid/fluid interface, the number of the mesh cells (including the partial cells) lying in the fluid region along the line normal to the solid/fluid interface and starting from the center of this cell must not be less than the criterion value. Otherwise each of the mesh cells on this line is split into 8 child cells.

As a result of all these meshing procedures, a locally refined rectangular computational mesh is obtained and used then for solving the governing equations on it.

Since all the above-mentioned meshing procedures are performed before the calculation, the obtained mesh is unable to resolve all the solution features well. To overcome this disadvantage, the computational mesh can be refined further at the specified moments during the calculation in accordance with the solution spatial gradients (both in fluid and in solid, see User's Guide for details). As a result, in the low-gradient regions the cells are merged, whereas in the high-gradient regions the cells are split. The moments of the computational mesh refinement during the calculation are prescribed either automatically or manually.

Spatial Approximations

The cell-centered finite volume (FV) method is used to obtain conservative approximations of the governing equations on the locally refined rectangular mesh. The governing equations are integrated over a control volume which is a grid cell, and then approximated with the cell-centered values of the basic variables. The integral conservation laws may be represented in the form of the cell volume and surface integral equation:

$$\frac{\partial}{\partial t} \int \mathbf{U} dv + \oint \mathbf{F} \cdot d\mathbf{s} = \int \mathbf{Q} dv \quad (1.41)$$

are replaced by the discrete form

$$\frac{\partial}{\partial t}(\mathbf{U}_v) + \sum_{cell\ faces} \mathbf{F} \cdot \mathbf{S} = \mathbf{Q}_v \quad (1.42)$$

The second-order upwind approximations of fluxes \mathbf{F} are based on the implicitly treated modified Leonard's QUICK approximations (Ref. 8) and the Total Variation Diminishing (TVD) method (Ref. 9).

In Flow Simulation, especially consistent approximations for the convective terms, **div** and **grad** operators are employed in order to derive a discrete problem that maintains the fundamental properties of the parent differential problem in addition to the usual properties of mass, momentum and energy conservation.

Spatial Approximations at the Solid/fluid Interface

Considering equation (1.42) for **partial** mesh cells (i.e., for the mesh cells cut by the solid/fluid interface), we introduce the additional boundary faces and the corresponding boundary fluxes taking the boundary conditions and geometry into account (see Fig.1.6), as well as use a special calculation procedure for them. As a result, the solid/fluid interface influence on the problem solution both in the fluid and in the solid is calculated very accurately.

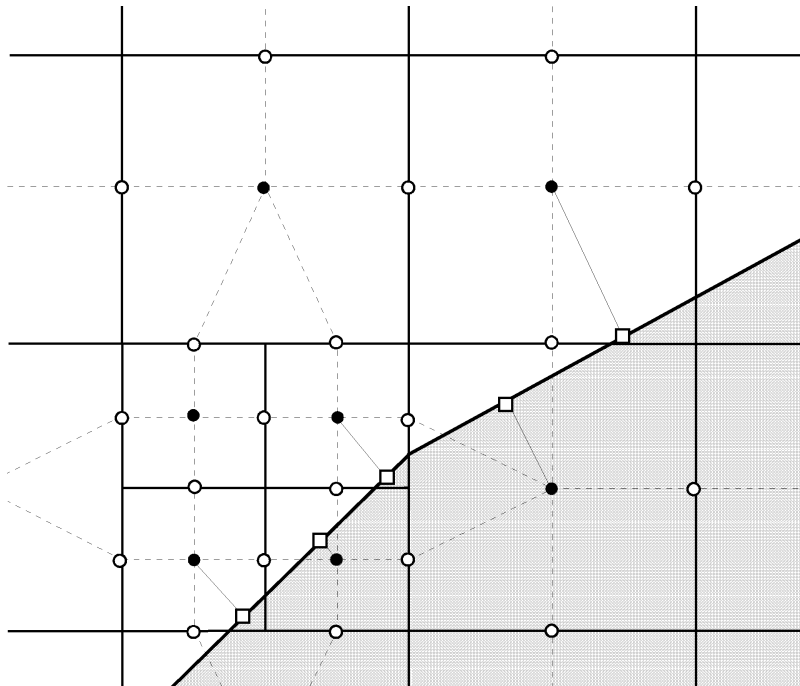


Fig.1.6Computational mesh cells at the solid/fluid interface.

Temporal Approximations

Time-implicit approximations of the continuity and convection/diffusion equations (for momentum, temperature, etc.) are used together with an operator-splitting technique (Ref. 10, Ref. 11, and Ref. 12). This technique is used to efficiently resolve the problem of pressure-velocity decoupling. Following the SIMPLE-like approach (Ref. 13), an elliptic type discrete pressure equation is derived by algebraic transformations of the originally derived discrete equations for mass and momentum, and taking into account the boundary conditions for velocity.

Form of the Numerical Algorithm

Let index 'n' denotes the time-level, and '*' denotes intermediate values of the flow parameters. The following numerical algorithm is employed to calculate flow parameters on time-level (n+1) using known values on time-level (n):

$$\frac{\mathbf{U}^* - \mathbf{U}^n}{\Delta t} + A_h(\mathbf{U}^n, p^n) \mathbf{U}^* = \mathbf{S}^n, \quad (1.43)$$

$$L_h \delta p = \frac{\text{div}_h(\rho \mathbf{u}^*)}{\Delta t} + \frac{1}{\Delta t} \frac{\rho^* - \rho^n}{\Delta t}, \quad (1.44)$$

$$\rho^* = \rho(p^n + \delta p, T^*, \mathbf{y}^*), \quad (1.45)$$

$$\rho \mathbf{u}^{n+1} = \rho \mathbf{u}^* - \Delta t \cdot \text{grad}_h \delta p, \quad (1.45)$$

$$p^{n+1} = p^n + \delta p, \quad (1.46)$$

$$\rho T^{n+1} = \rho T^*, \rho \kappa^{n+1} = \rho \kappa^*, \rho \varepsilon^{n+1} = \rho \varepsilon^*, \rho \mathbf{y}^{n+1} = \rho \mathbf{y}^*, \quad (1.47)$$

$$\rho^{n+1} = \rho(p^{n+1}, T^{n+1}, \mathbf{y}^{n+1}). \quad (1.48)$$

Here $\mathbf{U} = (\rho \mathbf{u}, \rho T, \rho \kappa, \rho \varepsilon, \rho \mathbf{y})^T$ is the full set of basic variables excluding pressure p , $\mathbf{u} = (u_1, u_2, u_3)^T$ is the velocity vector, $\mathbf{y} = (y_1, y_2, \dots, y_M)^T$ is the vector of component concentrations in fluid mixtures, and $\delta p = p^{n+1} - p^n$ is an auxiliary variable that is called a pressure correction. These parameters are discrete functions stored at cell centers. They are to be calculated using the discrete equations (1.43)-(1.48) that approximate the governing differential equations. In equations (1.43)-(1.48) A_h , div_h , grad_h and $L_h = \text{div}_h \text{grad}_h$ are discrete operators that approximate the corresponding differential operators with second order accuracy.

Equation (1.43) corresponds to the first step of the algorithm when fully implicit discrete convection/diffusion equations are solved to obtain the intermediate values of momentum and the final values of turbulent parameters, temperature, and species concentrations.

The elliptic type equation (1.44) is used to calculate the pressure correction δp . This equation is defined in such a way that the final momentum field $\rho \mathbf{u}^{n+1}$ calculated from (1.43) satisfies the discrete fully implicit continuity equation. Final values of the flow parameters are defined by equations (1.45)-(1.48).

Methods to Resolve Linear Algebraic Systems

Iterative Methods for Nonsymmetrical Problems

To solve the asymmetric systems of linear equations that arise from approximations of momentum, temperature and species equations (1.43), a preconditioned generalized conjugate gradient method (Ref. 14) is used. Incomplete LU factorization is used for preconditioning.

Iterative Methods for Symmetric Problems

To solve symmetric algebraic problem for pressure-correction (1.44), an original double-preconditioned iterative procedure is used. It is based on a specially developed multigrid method (Ref. 15).

Multigrid Method

The multigrid method is a convenient acceleration technique which can greatly decrease the solution time. Basic features of the multigrid algorithm are as follows. Based on the given mesh, a sequence of grids (grid levels) are constructed, with a decreasing number of nodes. On every such grid, the residual of the associated system of algebraic equations is restricted onto the coarser grid level, forming the right hand side of the system on that grid. When the solution on the coarse grid is computed, it is interpolated to the finer grid and used there as a correction to the result of the previous iteration. After that, several smoothing iterations are performed. This procedure is applied repeatedly on every grid level until the corresponding iteration meets the stopping criteria.

The coefficients of the linear algebraic systems associated with the grid are computed once and stored.

References

- 1 Reid R.C., Prausnitz J.M., Poling B.E. (1987). *The properties of gases and liquids, 4th edition*, McGraw-Hill Inc., NY, USA.
- 2 Idelchik, I.E. (1986). *Handbook of Hydraulic Resistance, 2nd edition*, Hemisphere, New York, USA.
- 3 Henderson, C.B. *Drag Coefficients of Spheres in Continuum and Rarefied Flows*. AIAA Journal, v.14, No.6, 1976.
- 4 Carlson, D.J. and Hoglund, R.F. *Particle Drag and Heat Transfer in Rocket Nozzles*. AIAA Journal, v.2, No.11, 1964.
- 5 ASHRAE Handbook–2001 Fundamentals.
- 6 ISO 7726:1998, Ergonomics of the Thermal Environment – Instruments for Measuring Physical Quantities.
- 7 ISO 7730:2005, Ergonomics of the thermal environment - Analytical determination and interpretation of thermal comfort using calculation of the PMV and PPD indices and local thermal comfort criteria.
- 8 Roache, P.J., (1998) *Technical Reference of Computational Fluid Dynamics*, Hermosa Publishers, Albuquerque, New Mexico, USA.
- 9 Hirsch, C., (1988). *Numerical computation of internal and external flows*. John Wiley and Sons, Chichester.
- 10 Glowinski, R. and P. Le Tallec, (1989). *Augmented Lagrangian Methods and Operator-Splitting Methods in Nonlinear Mechanics*. SIAM, Philadelphia.
- 11 Marchuk, G.I., (1982). *Methods of Numerical Mathematics*, Springer-Verlag, Berlin.
- 12 Samarskii, A.A., (1989). *Theory of Difference Schemes*, Nauka, Moscow (in Russian).
- 13 Patankar, S.V., (1980). *Numerical Heat Transfer and Fluid Flow*, Hemisphere, Washington, D.C.
- 14 Saad, Y. (1996). *Iterative methods for sparse linear systems*, PWS Publishing Company, Boston.
- 15 Hackbusch, W. (1985). *Multi-grid Methods and Applications*, Springer-Verlag, NY, USA.

Validation Examples

Introduction

A series of calculation examples presented below validate the ability of Flow Simulation to predict the essential features of various flows, as well as to solve conjugate heat transfer problems (i.e. flow problems with heat transfer in solids). In order to perform the validation accurately and to present clear results which the user can check independently, relatively simple examples have been selected. For each of the following examples, exact analytical expression or well-documented experimental results exist. Each of the examples focus on one or two particular physical phenomena such as: laminar flow with or without heat transfer, turbulent flows including vortex development, boundary layer separation and heat transfer, compressible gas flow with shock and expansion waves. Therefore, these examples validate the ability of Flow Simulation to predict fundamental flow features accurately. The accuracy of predictions can be extrapolated to typical industrial examples (encountered every day by design engineers and solved using Flow Simulation), which may include a combination of the above-mentioned physical phenomena and geometries of arbitrary complexity.

1 Flow through a Cone Valve

Let us see how Flow Simulation predicts incompressible turbulent 3D flows in a 3D cone valve taken from Ref.14 (the same in Ref.2) and having a complex flow passage geometry combining sudden 3D contractions and expansions at different turning angles ϕ (Fig. 1.1.). Following the Refs.2 and 14 recommendations on determining a valve's hydraulic resistance correctly, i.e. to avoid any valve-generated flow disturbances at the places of measuring the flow total pressures upstream and downstream of the valve, the inlet and outlet straight pipes of the same diameter D and of enough length (we take $7D$ and $17D$) are connected to the valve, so constituting the experimental rig model (see Fig. 1.2.). As in Ref.14, a water flows through this model. Its temperature of 293.2 K and fully developed turbulent inlet profile (see Ref.1) with mass-average velocity $U \approx 0.5$ m/s (to yield the turbulent flow's Reynolds number based on the pipe diameter $Re_D = 10^5$) are specified at the model inlet, and static pressure of 1 atm is specified at the model outlet.

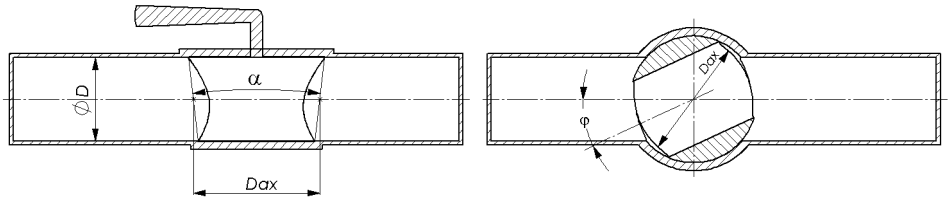


Fig. 1.1. The cone valve under consideration: $D = 0.206$ m, $D_{ax} = 1.515D$, $\alpha = 13^\circ 40'$.

The corresponding model used for these predictions is shown in Fig. 1.2.. The valve's turning angle ϕ is varied in the range of $0 \dots 55^\circ$ (the valve opening diminishes to zero at $\phi = 82^\circ 30'$).

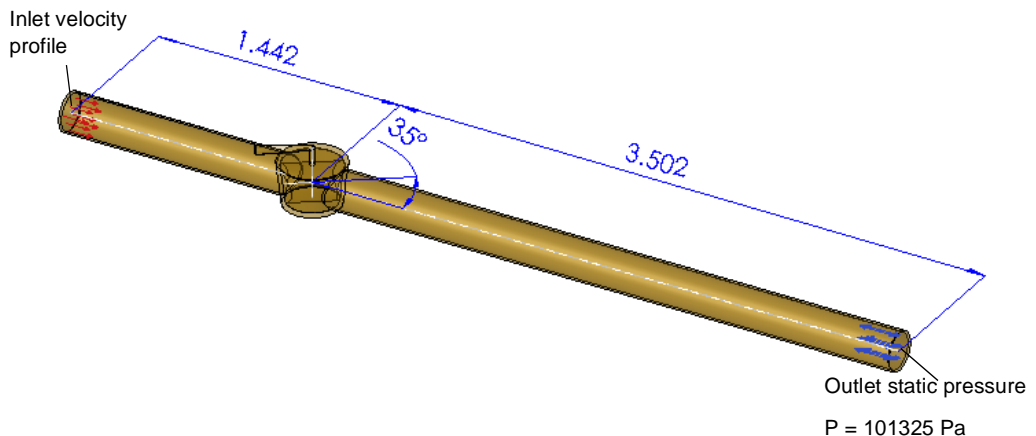


Fig. 1.2. The model for calculating the 3D flow in the cone valve.

The flow predictions performed with Flow Simulation are validated by comparing the valve's hydraulic resistance ζ_v and the dimensionless coefficient of torque M (see Fig. 1.1.) acting on the valve, m , to the experimental data of Ref.14 (Ref.2).

Since Ref.14 presents the valve's hydraulic resistance (i.e. the resistance due to the flow obstacle, which is the valve) ζ_v , whereas the flow calculations in the model (as well as the experiments on the rig) yield the total hydraulic resistance including both ζ_v and the tubes' hydraulic resistance due to friction, ζ_f , i.e. $\zeta = \zeta_v + \zeta_f$, then, to obtain ζ_v from the flow predictions (as well as from the experiments), ζ_f is calculated (measured in the experiments) separately, at the fully open valve ($\varphi = 0$); then $\zeta_v = \zeta - \zeta_f$.

In accordance with Ref.14, both ζ and ζ_f are defined as $(P_{o\ inlet} - P_{o\ outlet})/(\rho U^2/2)$, where $P_{o\ inlet}$ and $P_{o\ outlet}$ are the flow total pressures at the model's inlet and outlet, accordingly, ρ is the fluid density. The torque coefficient is defined as $m = M/[D^3 \cdot (\rho U^2/2) \cdot (1 + \zeta_v)]$, where M is the torque trying to slew the valve around its axis (vertical in the left picture in Fig. 1.1.) due to a non-uniform pressure distribution over the valve's inner passage (naturally, the valve's outer surface pressure cannot contribute to this torque). M is measured directly in the experiments and is integrated by Flow Simulation over the valve's inner passage.

The Flow Simulation predictions have been performed at result resolution level of 5 with manual setting of the minimum gap size to the valve's minimum passage in the $Y = 0$ plane and the minimum wall thickness to 3 mm (to resolve the valve's sharp edges).

Flow Simulation has predicted $\zeta_f = 0.455$, ζ_v shown in Fig. 1.3., and m shown in Fig. 1.4. It is seen that the Flow Simulation predictions well agree with the experimental data.

This cone valve's 3D vortex flow pattern at $\varphi = 45^\circ$ is shown in Fig. 1.5. by flow trajectories colored by total pressure. The corresponding velocity contours and vectors at the $Y = 0$ plane are shown in Fig. 1.6.

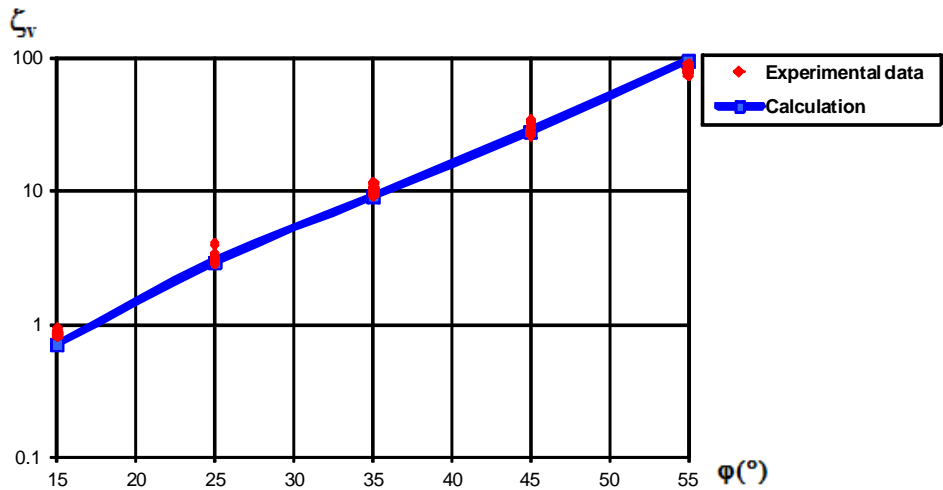


Fig. 1.3. Comparison of the Flow Simulation predictions with the Ref.14 experimental data on the cone valve's hydraulic resistance versus the cone valve turning angle.

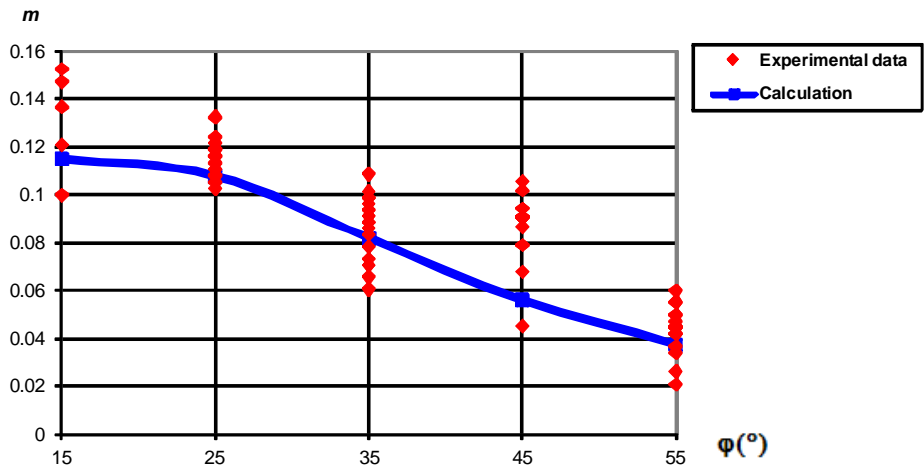


Fig. 1.4. Comparison of the Flow Simulation predictions with the Ref.14 experimental data on the cone valve's torque coefficient versus the cone valve turning angle.

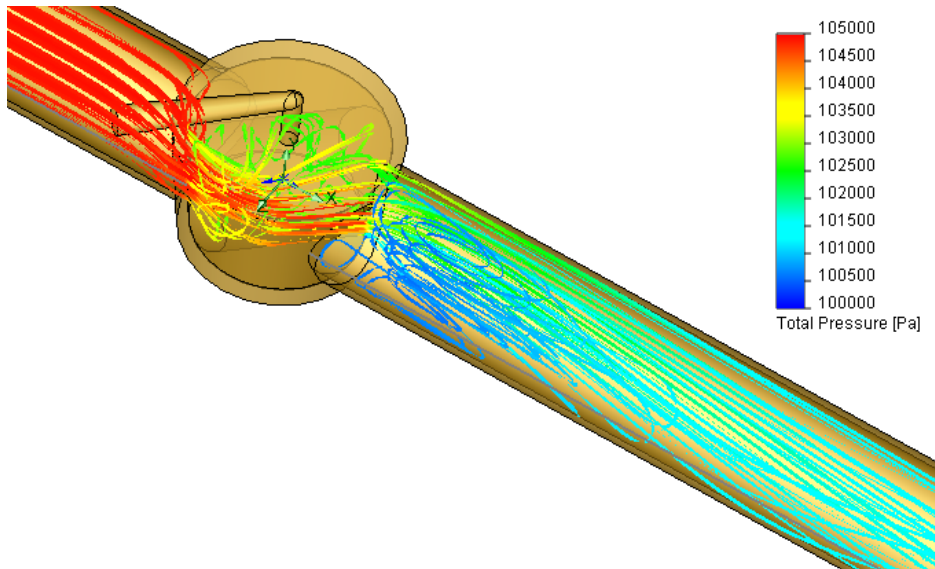


Fig. 1.5. Flow trajectories colored by total pressure at $\varphi = 45^\circ$.

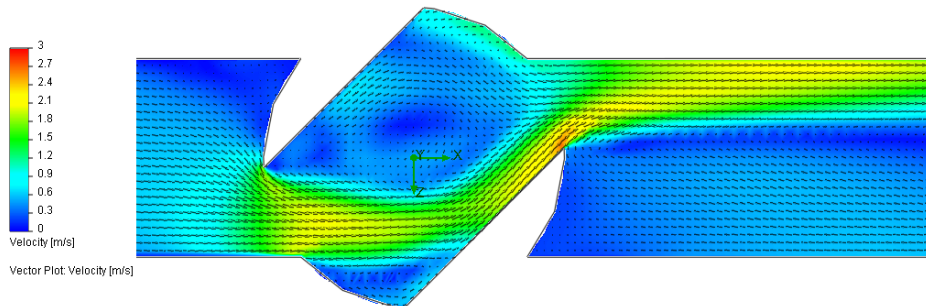


Fig. 1.6. The cone valve's velocity contours and vectors at $\varphi = 45^\circ$.

2 Laminar Flows Between Two Parallel Plates

Let us consider two-dimensional (planar) steady-state laminar flows of Newtonian, non-Newtonian, and compressible liquids between two parallel stationary plates spaced at a distance of $2h$ (see Fig. 2.1.).

In the case of Newtonian and non-Newtonian liquids the channel has a $2h = 0.01$ m height and a 0.2 m length, the inlet for these liquids have standard ambient temperature (293.2 K) and a uniform inlet velocity profile of $u_{average} = 0.01$ m/s (entrance disturbances are neglected). The inlet pressure is not known beforehand, since it will be obtained from the calculations in accordance with the specified channel exit pressure of 1 atm. (The fluids pass through the channel due to a pressure gradient.)

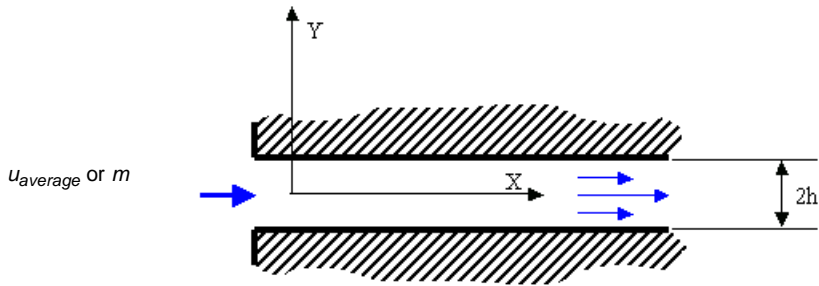


Fig. 2.1. Flow between two parallel plates.

Since the Reynolds number based on the channel height is equal to about $Re_{2h}=100$, the flow is laminar.

As for the liquids, let us consider water as a Newtonian liquid and four non-Newtonian liquids having identical density of 1000 kg/m^3 , identical specific heat of 4200 J/(kgK) and identical thermal conductivity of 10 W/(mK) , but obeying different non-Newtonian liquid laws available in Flow Simulation.

The considered non-Newtonian liquids' models and their governing characteristics are presented in Table 2.1. These models are featured by the function connecting the flow shear stress (τ) with the flow shear rate ($\dot{\gamma}$), i.e. $\tau = f(\dot{\gamma})$, or, following Newtonian liquids, the liquid dynamic viscosity (η) with the flow shear rate ($\dot{\gamma}$), i.e. $\tau = \eta(\dot{\gamma}) \cdot \dot{\gamma}$:

- 1 the Herschel-Bulkley model: $\tau = K \cdot (\dot{\gamma})^n + \tau_o$, where K is the consistency coefficient, n is the power-law index, and τ_o is the yield stress (a special case with $n = 1$ gives the Bingham model);
- 2 the power-law model: $\tau = K \cdot (\dot{\gamma})^n$, i.e., $\eta = K \cdot (\dot{\gamma})^{n-1}$, which is a special case of Herschel-Bulkley model with $\tau_o = 0$;
- 3 the Carreau model: $\tau = \eta \cdot \dot{\gamma}$, $\eta = \eta_\infty + (\eta_o - \eta_\infty) \cdot \left[1 + (K_1 \cdot \dot{\gamma})^2 \right]^{(n-1)/2}$, where η_∞ is the liquid dynamic viscosity at infinite shear rate, i.e. the minimum dynamic viscosity, η_o is the liquid dynamic viscosity at zero shear rate, i.e. the maximum

dynamic viscosity, K_I is the time constant, n is the power-law index (this model is a smooth version of the power-law model).

Table 2.1

Non-Newtonian liquid No.	1	2	3	4
Non-Newtonian liquid model	Herschel-Bulkley	Bingham	Power law	Carreau
Consistency coefficient, K (Pa.s ⁿ)	0.001	0.001	0.001	-
Power law index, n	1.5	1	0.6	0.4
Yield stress, τ_o (Pa)	0.001	0.001	-	-
Minimum dynamic viscosity, η_∞ (Pa.s)	-	-	-	10^{-4}
Maximum dynamic viscosity, η_o (Pa.s)	-	-	-	10^{-3}
Time constant, K_I (s)	-	-	-	1

In accordance with the well-known theory presented in Ref. 1, after some entrance length, the flow profile $u(y)$ becomes fully developed and invariable. It can be determined from

the Navier-Stokes x -momentum equation $\frac{dP}{dx} = \frac{d\tau}{dy} = \text{const} = \frac{\tau_w}{h}$ corresponding to

this case in the coordinate system shown in Fig. 2.1. ($y = 0$ at the channel's center plane,

$\frac{dP}{dx}$ is the longitudinal pressure gradient along the channel, $\dot{\gamma} = \frac{du}{dy}$ in the flow under consideration).

As a result, the fully developed $u(y)$ profile for a Newtonian fluid has the following form:

$$u(y) = -\frac{1}{2\eta} \frac{dP}{dx} (h^2 - y^2),$$

where η is the fluid dynamic viscosity and η is the half height of the channel,

$$\frac{dP}{dx} = -\frac{3\eta u_{average}}{h^2},$$

where $u_{average}$ is the flow's mass-average velocity defined as the flow's volume flow rate divided by the area of the flow passage cross section.

For a non-Newtonian liquid described by the power-law model the fully developed $u(y)$ profile and the corresponding pressure gradient can be determined from the following formulae:

$$u(y) = u_{average} \frac{2n+1}{n+1} \left(1 - \left(\frac{y}{h} \right)^{\frac{n+1}{n}} \right), \quad \frac{dP}{dx} = -\frac{K}{h} \cdot \left(\frac{u_{average}}{h} \cdot \frac{2n+1}{n} \right)^n.$$

For a non-Newtonian liquid described by the Herschel-Bulkley model the fully developed $u(y)$ profile can be determined from the following formulae:

$$u(y) = u_{\max} = \frac{h}{K^{1/n} \tau_w} \frac{n}{n+1} (\tau_w - \tau_o)^{\frac{n+1}{n}} \text{ at } |y| < \frac{\tau_o}{\tau_w} h ,$$

$$u(y) = u_{\max} \cdot \left(1 - \left(\frac{\tau_w \frac{y}{h} - \tau_o}{\tau_w - \tau_o} \right)^{\frac{n+1}{n}} \right) \text{ at } y > \frac{\tau_o}{\tau_w} h ,$$

where the unknown wall shear stress τ_w is determined numerically by solving the nonlinear equation

$$u_{\text{average}} = \frac{h}{K^{1/n} \tau_w} \cdot \frac{n}{n+1} \cdot (\tau_w - \tau_o)^{\frac{n+1}{n}} \cdot \left(1 - \frac{n}{2n+1} \frac{\tau_w - \tau_o}{\tau_w} \right) ,$$

e.g. with the Newton method, as described in this validation. The corresponding pressure

gradient is determined as $\frac{dP}{dx} = \frac{\tau_w}{h}$.

For a non-Newtonian liquid described by the Carreau model the fully developed $u(y)$ profile can not be determined analytically in an explicit form, so in this validation example it is obtained by solving the following parametric equation:

$$y = \frac{h}{\tau_w} p \left(\mu_{\infty} + (\mu_0 - \mu_{\infty}) (1 + \lambda^2 p^2)^{(n-1)/2} \right) ,$$

$$u = u_{\max} - \frac{h \mu_{\infty}}{2 \tau_w} p^2 - \frac{(\mu_0 - \mu_{\infty}) h}{(n+1) \tau_w} (1 + \lambda^2 p^2)^{(n-1)/2} \left(np^2 - \frac{1}{\lambda^2} \right) - \frac{(\mu_0 - \mu_{\infty}) h}{(n+1) \tau_w \lambda^2} ,$$

where p is a free parameter varied within the $\pm p_{\max}$ range,

$$\tau_w = p_{\max} \left(\mu_{\infty} + (\mu_0 - \mu_{\infty}) (1 + \lambda^2 p_{\max}^2)^{(n-1)/2} \right) ,$$

$$u_{\max} = \frac{h \mu_{\infty}}{2 \tau_w} p_{\max}^2 + \frac{(\mu_0 - \mu_{\infty}) h}{(n+1) \tau_w} (1 + \lambda^2 p_{\max}^2)^{(n-1)/2} \left(np_{\max}^2 - \frac{1}{\lambda^2} \right) + \frac{(\mu_0 - \mu_{\infty}) h}{(n+1) \tau_w \lambda^2}$$

The p value is varied to satisfy $hu_{average} = \int_0^h u dy = \int_0^{p_{max}} u \frac{dy}{dp} dp$.

The corresponding pressure gradient is equal to $\frac{dP}{dx} = \frac{\tau_w}{h}$.

The SolidWorks model for the 2D calculation is shown in Fig. 2.2.. The boundary conditions are specified as mentioned above and the initial conditions coincide with the inlet boundary conditions. The results of the calculations performed with Flow Simulation at result resolution level 5 are presented in Figs.2.3 - 2.8. The channel exit $u(y)$ profile and the channel $P(x)$ profile were obtained along the sketches shown by green lines in Fig. 2.2..

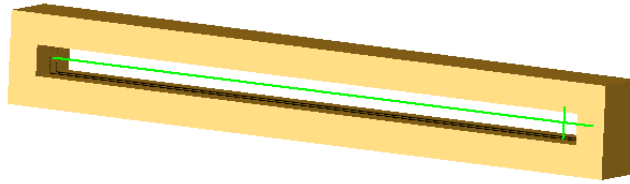


Fig. 2.2. The model for calculating 2D flow between two parallel plates with Flow Simulation.

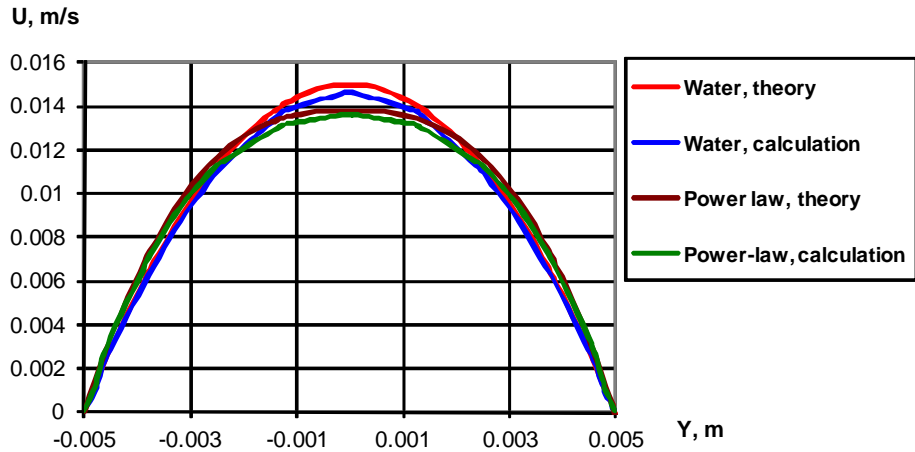


Fig. 2.3. The water and liquid #3 velocity profiles $u(y)$ at the channel outlet.

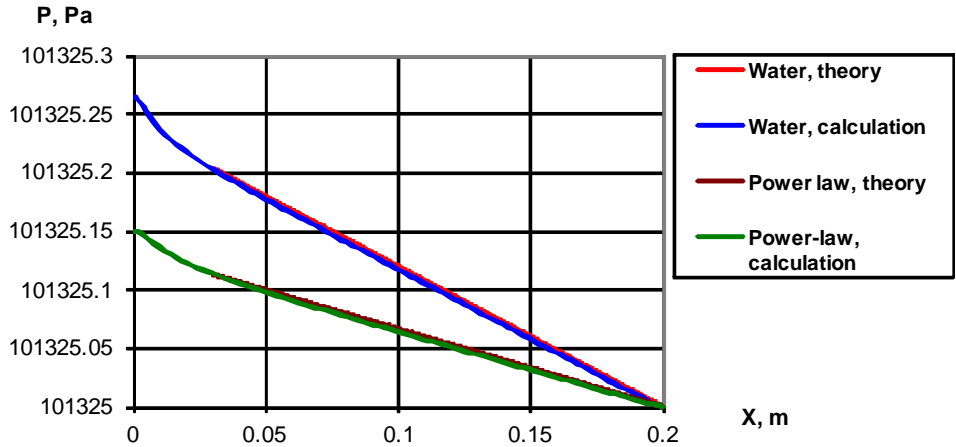


Fig. 2.4. The water and liquid #3 longitudinal pressure change along the channel, $P(x)$.

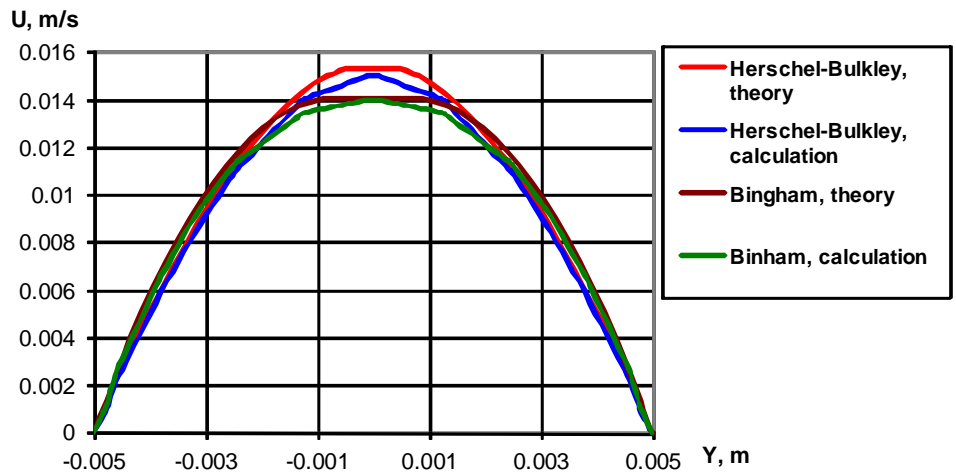


Fig. 2.5. The liquids #1 and #2 velocity profiles $u(y)$ at the channel outlet.

From Figs.2.4, 2.6, and 2.8 you can see that for all the liquids under consideration, after some entrance length of about 0.03 m, the pressure gradient governing the channel pressure loss becomes constant and nearly similar to the theoretical predictions. From Figs.2.3, 2.5, and 2.7 you can see that the fluid velocity profiles at the channel exit obtained from the calculations are close to the theoretical profiles.

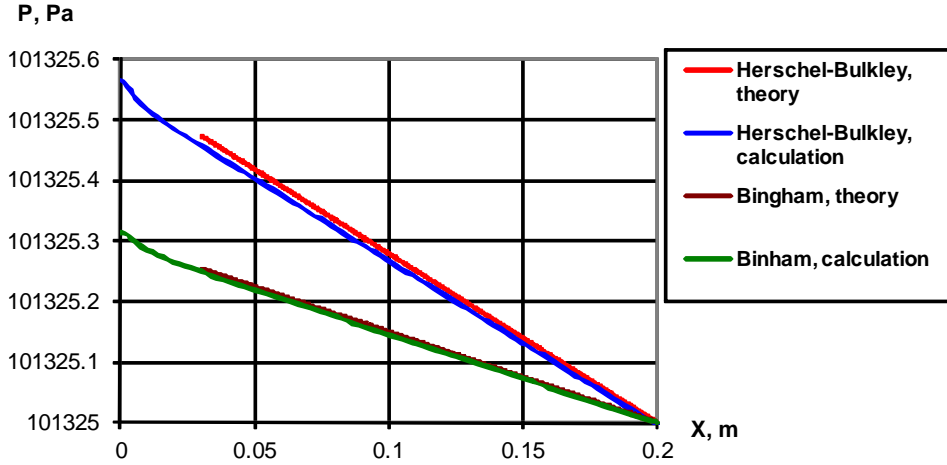


Fig. 2.6. The liquids #1 and #2 longitudinal pressure change along the channel, $P(x)$.

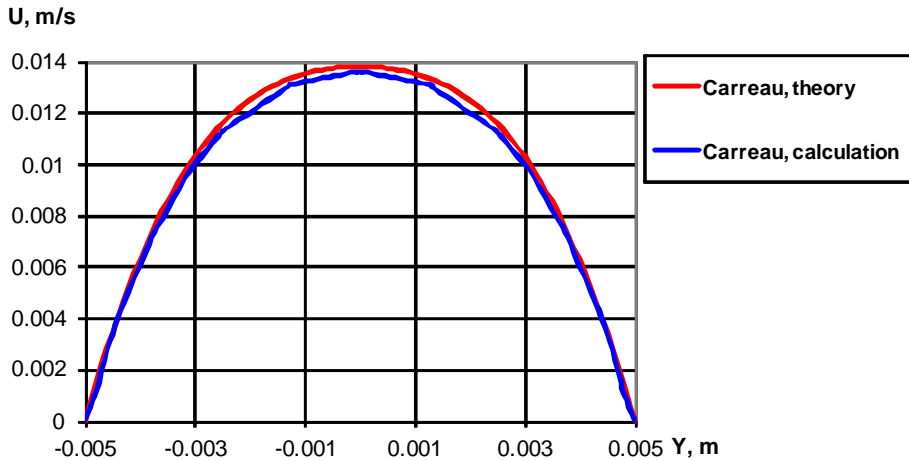


Fig. 2.7. The liquid #4 velocity profile $u(y)$ at the channel outlet.

In the case of compressible liquids the channel has the height of $2h = 0.001$ m and the length of 0.5 m, the liquids at its inlet had standard ambient temperature (293.2 K) and a uniform inlet velocity profile corresponding to the specified mass flow rate of $\dot{m} = 0.01$ kg/s.

The inlet pressure is not known beforehand, since it will be obtained from the calculations as providing the specified mass flow rate under the specified channel exit pressure of 1 atm. (The fluids pass through the channel due to the pressure gradient).

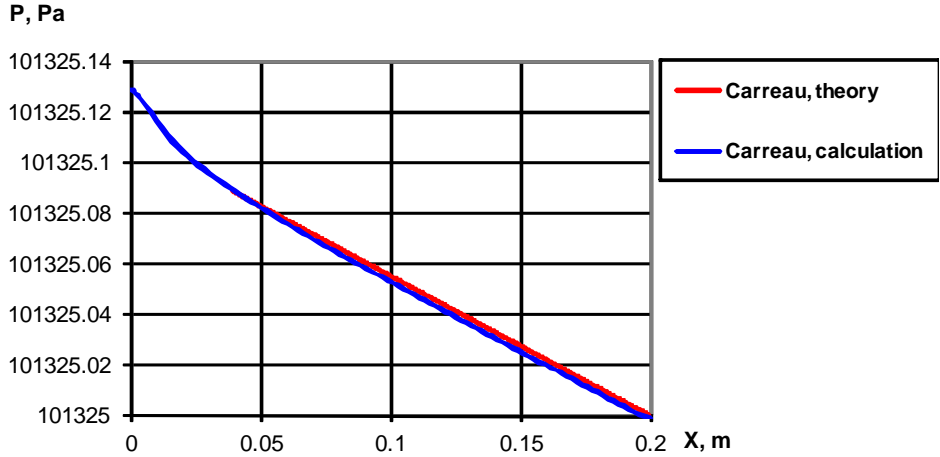


Fig. 2.8. The liquid #4 longitudinal pressure change along the channel, $P(x)$.

Let us consider two compressible liquids whose density obeys the following laws:

- the power law:

$$\left(\frac{\rho}{\rho_0}\right)^n = \frac{P+B}{P_0+B}, \text{ where } \rho_0, P_0, B \text{ and } n \text{ are specified: } \rho_0 \text{ is the liquid's density under the reference pressure } P_0, B \text{ and } n \text{ are constants,}$$

- the logarithmic law:

$$\rho = \frac{\rho_0}{1 - C \ln \frac{B+P}{B+P_0}}, \text{ where } \rho_0, P_0, B \text{ and } C \text{ are specified: } \rho_0 \text{ is the liquid's density under the reference pressure } P_0, B \text{ and } C \text{ are constants.}$$

In this validation example these law's parameters values have been specified as $\rho_0=10^3 \text{ kg/m}^3$, $P_0 = 1 \text{ atm}$, $B = 10^7 \text{ Pa}$, $n = 1.4$, $C = 1$, and these liquids have the $1 \text{ Pa}\cdot\text{s}$ dynamic viscosity.

Since this channel is rather long, the pressure gradient along it can be determined as

$$\frac{\partial P}{\partial x} = -\frac{3\eta}{h^2} \frac{\dot{m}}{S\rho}, \text{ where } \eta \text{ is the liquids' dynamic viscosity, } \dot{m} \text{ is the liquid mass flow rate, } S \text{ is the channel's width, } \rho \text{ is the liquid density.}$$

Therefore, by substitution the compressible liquids' $\rho(P)$ functions, we obtain the following equations for determining $P(x)$ along the channel:

- for the power-law liquid:

$$\frac{\partial P}{\partial x} = -\frac{3\mu}{h^2} \frac{\dot{m}}{S\rho_0} \left(\frac{P_0 + B}{P + B} \right)^{1/n}$$

its solution is

$$(P + B)^{1+1/n} \frac{n}{n+1} = \frac{3\mu\dot{m}}{h^2 S\rho_0} (P_0 + B)^{1/n} x + C_1 ,$$

where C_1 is a constant determined from the boundary conditions;

- for the logarithmic-law liquid:

$$\frac{\partial P}{\partial x} = -\frac{3\mu}{h^2} \frac{\dot{m}}{S\rho_0} \left(1 - C \ln \frac{P+B}{P_0+B} \right), \text{ this equation is solved numerically.}$$

Both the theoretical $P(x)$ distributions and the corresponding distributions computed within Flow Simulation on a 5*500 computational mesh are presented in Figs.2.9 and 2.10. It is seen that the Flow Simulation calculations agree with the theoretical distributions.

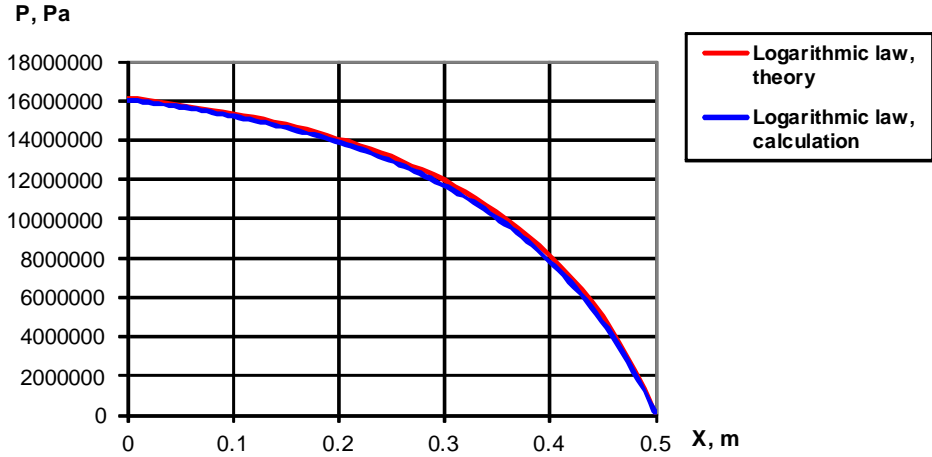


Fig. 2.9. The logarithmic-law compressible liquid's longitudinal pressure change along the channel, $P(x)$.

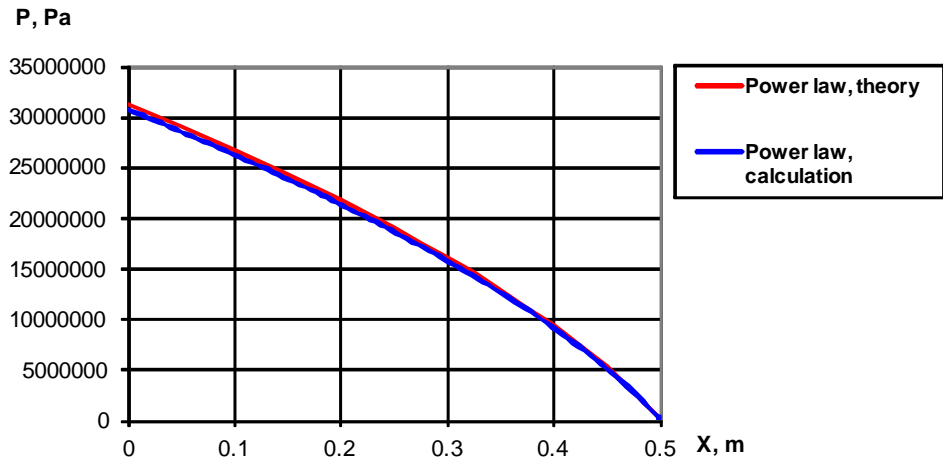


Fig. 2.10. The power-law compressible liquid's longitudinal pressure change along the channel, $P(x)$.

3 Laminar and Turbulent Flows in Pipes

Let us see how the 3D flow through a straight pipe is predicted. We consider water (at standard 293.2 K temperature) flowing through a long straight pipe with circular cross section of $d = 0.1$ m (see Fig. 3.1.). At the pipe inlet the velocity is uniform and equal to u_{inlet} . At the pipe outlet the static pressure is equal to 1 atm.

The SolidWorks model used for all the 3D pipe flow calculations is shown in Fig. 3.2. The initial conditions have been specified to coincide with the inlet boundary conditions. The computational domain is reduced to domain ($Z \geq 0$, $Y \geq 0$) with specifying the flow symmetry planes at $Z = 0$ and $Y = 0$.

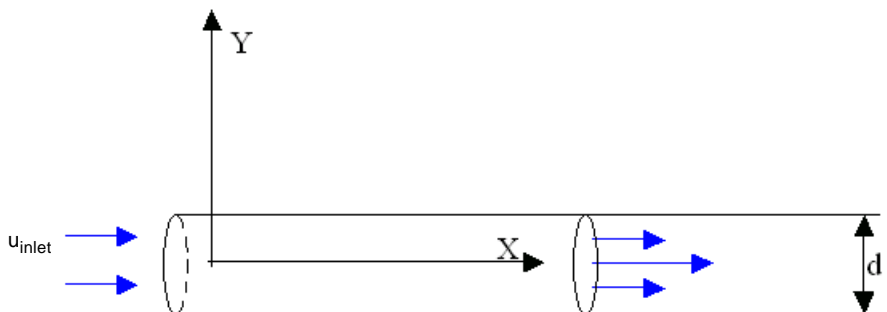


Fig. 3.1. Flow in a pipe.

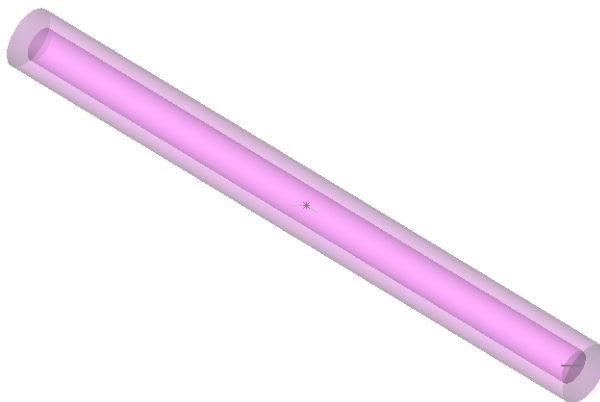


Fig. 3.2. The SolidWorks model for calculating 3D flow in a pipe with Flow Simulation.

According to theory (Ref.1), the pipe flow velocity profile changes along the pipe until it becomes a constant, fully developed profile at a distance of L_{inlet} from the pipe inlet. According to Ref.1, L_{inlet} is estimated as:

where $Re_d = \rho \cdot U \cdot d / \mu$ is the Reynolds number based on the pipe diameter d , U is the mass-average flow velocity, ρ is the fluid density, and μ is the fluid dynamic viscosity.

$$L_{inlet} = \begin{cases} 0.03 \cdot d \cdot Re_d \geq 3 \cdot d, & Re_d = 0.1...2500 \\ 100 \cdot d, & Re_d = 2500...6000 \\ 40 \cdot d, & Re_d = 6000...10^6 \end{cases}$$

Therefore, to provide a fully developed flow in the pipe at Re_d under consideration, we will study the cases listed in Table 3.2. Here, L_{pipe} is the overall pipe length. All the Flow Simulation predictions concerning the fully developed pipe flow characteristics are referred to the pipe section downstream of the inlet section.

Table 3.2 Pipe inlet velocities and lengths.

Re_d	u_{inlet} m/s	L_{inlet} m	L_{pipe} m
0.1	10^{-6}	0.3	0.45
100	0.001	0.3	0.45
1000	0.01	3	4.5
10^4	0.1	4 (5)*	6 (10)*
10^5	1	4 (5)*	6 (10)*
10^6	10	4 (5)*6	6 (10)*

*) the lengths in brackets are for the rough pipes.

The flow regime in a pipe can be laminar, turbulent, or transitional, depending on Re_d . According to Ref.1, $Re_d = 4000$ is approximately the boundary between laminar pipe flow and turbulent one (here, the transitional region is not considered).

Theory (Refs. 1 and 4) states that for laminar fully developed pipe flows (Hagen-Poiseuille flow) the velocity profile $u(y)$ is invariable and given by:

$$u(y) = -\frac{1}{4\mu} \frac{dP}{dx} (R^2 - y^2) \quad ,$$

where R is the pipe radius, and dP/dx is the longitudinal pressure gradient along the pipe, which is also invariable and equal to:

$$\frac{dP}{dx} = -\frac{8\mu u_{inlet}}{R^2} \quad .$$

The Flow Simulation predictions of dP/dx and $u(y)$ of the laminar fully developed pipe flow at $Re_d = 100$ performed at result resolution level 6 are presented in Fig. 3.3. and Fig. 3.4. The presented predictions relate to the smooth pipe, and similar ones not presented here have been obtained for the case of the rough tube with relative sand roughness of $k/d=0.2...0.4$ %, that agrees with the theory (Ref.1).

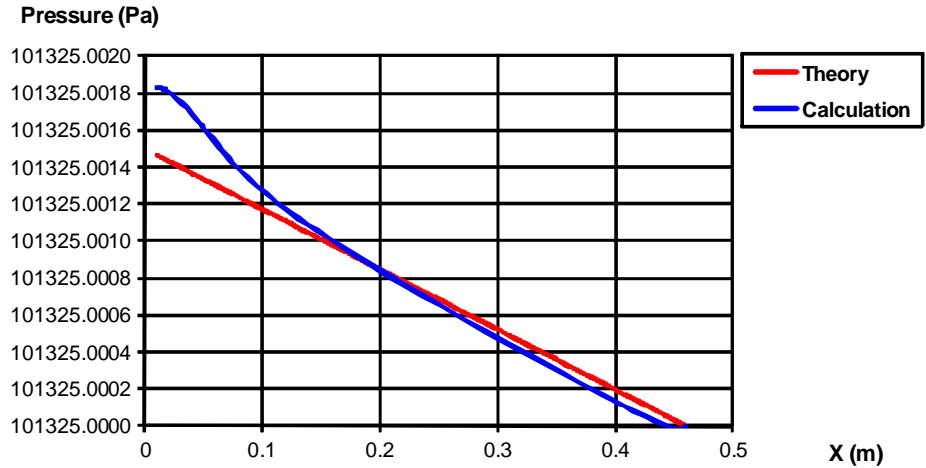


Fig. 3.3. The longitudinal pressure change (pressure gradient) along the pipe at $Re_d \approx 100$.

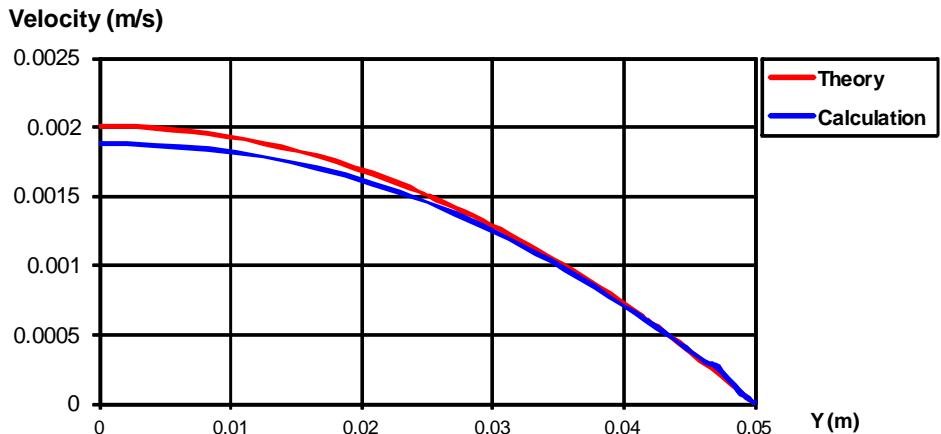


Fig. 3.4. The fluid velocity profile at the pipe exit for $Re_d \approx 100$.

From Fig. 3.3, one can see that after an entrance length of about 0.15 m the pressure gradient predicted by Flow Simulation coincides with the one predicted by theory. Therefore, the prediction of pipe pressure loss is excellent. As for local flow features, from Fig. 3.4, one can see that the fluid velocity profiles predicted at the pipe exit are rather close to the theoretical profile.

The velocity profile and longitudinal pressure distribution in a smooth pipe at $Re_d = 10^5$, i.e., in a turbulent pipe flow regime, predicted by Flow Simulation at result resolution level 6 are presented in Figs.3.5 and 3.6 and compared to theory (Ref.1, the Blasius law of pressure loss, the 1/7-power velocity profile).

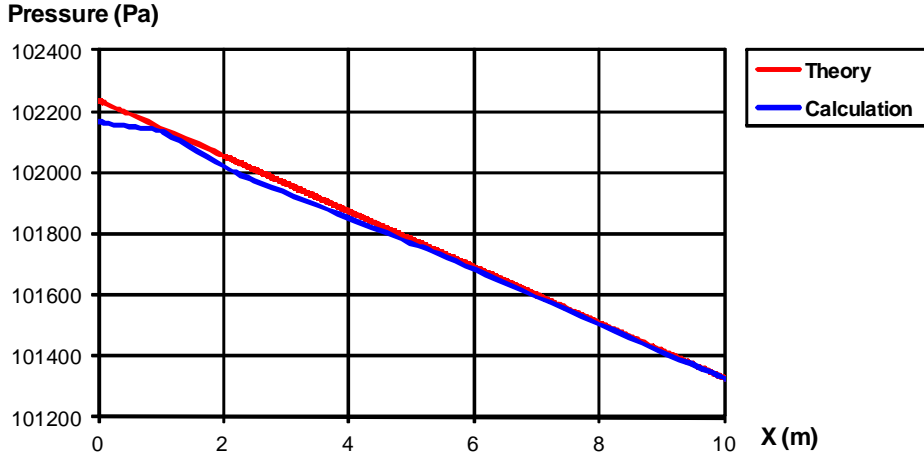


Fig. 3.5. The longitudinal pressure change (pressure gradient) along the pipe at $Re_d = 10^5$.

Then, to stand closer to engineering practice, let us consider the Flow Simulation predictions of the pipe friction factor used commonly and defined as:

$$f = \frac{\Delta P}{\rho \frac{u_{inlet}^2}{2}} \cdot \frac{d}{L} ,$$

where L is length of the pipe section with the fully developed flow, along which pressure loss ΔP is measured.

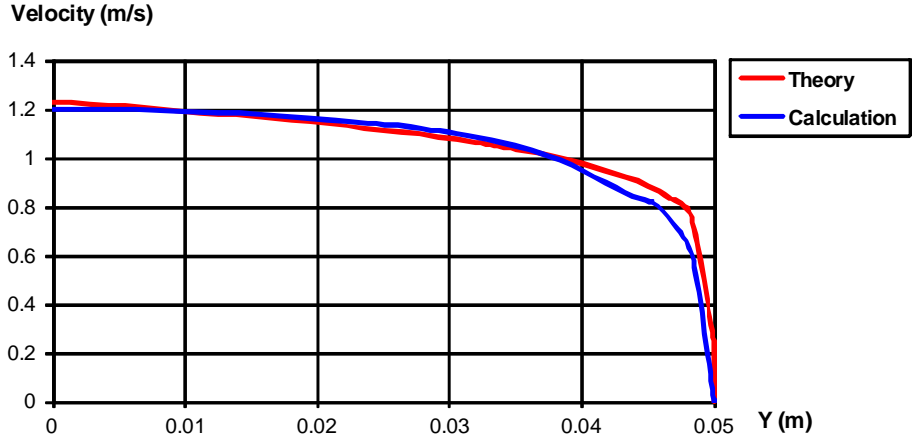


Fig. 3.6. The fluid velocity profile at the pipe exit at $Re_d = 10^5$.

In Figs. 3.7 and 3.8 (scaled up) you can see the Flow Simulation predictions performed at result resolution level 5 for the smooth pipes in the entire Re_d range (both laminar and turbulent), and compared with the theoretical and empirical values determined from the following formulae which are valid for fully-developed flows in smooth pipes (Refs.1, 2, and 4):

$$f = \begin{cases} \frac{64}{Re_d}, & Re_d \leq 2300 - \text{laminar flows}, \\ 0.316 \cdot Re_d^{-1/4}, & 4000 < Re_d < 10^5 - \text{turbulent flows}, \\ \left(1.8 \cdot \log \frac{Re_d}{6.9}\right)^{-2}, & Re_d \geq 10^5 - \text{turbulent flows} \end{cases}$$

It can be seen that the friction factor values predicted for smooth pipes, especially in the laminar region, are fairly close to the theoretical and empirical curve.

As for the friction factor in rough pipes, the Flow Simulation predictions for the pipes having relative wall roughness of $k/d=0.4\%$ (k is the sand roughness) are presented and compared with the empirical curve for such pipes (Refs.1, 2, and 4) in Fig. 3.8.. The underprediction error does not exceed 13%.

Additionally, in the full accordance with theory and experimental data the Flow Simulation predictions show that the wall roughness does not affect the friction factor in laminar pipe flows.

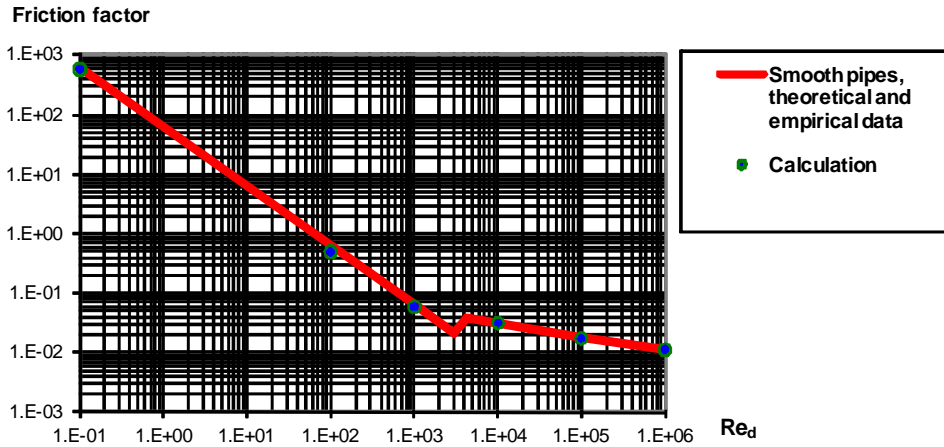


Fig. 3.7. The friction factor predicted by Flow Simulation for smooth pipes in comparison with the theoretical and empirical data (Refs.1, 2, and 4).

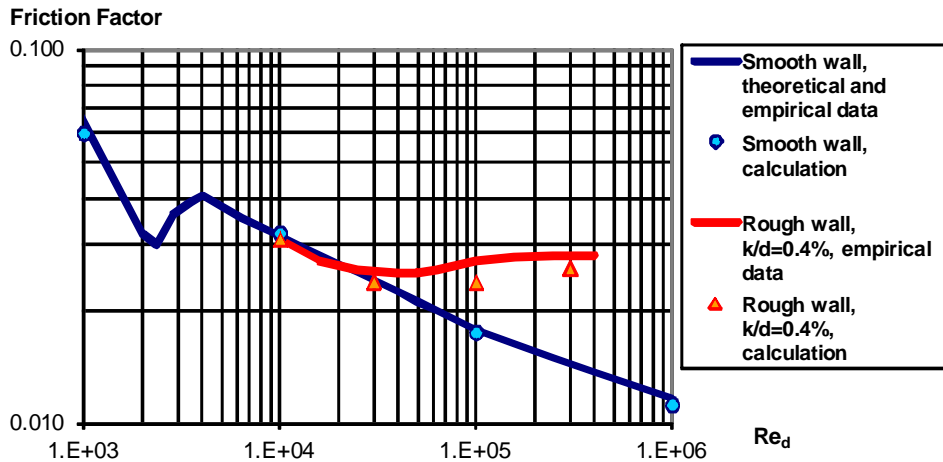


Fig. 3.8. The friction factor predicted by Flow Simulation for smooth and rough pipes in comparison with the theoretical and empirical data (Refs.1, 2, and 4).

4 Flows Over Smooth and Rough Flat Plates

Let us consider uniform flows over smooth and rough flat plates with laminar and turbulent boundary layers, so that Flow Simulation predictions of a flat plate drag coefficient are validated.

We consider the boundary layer development of incompressible uniform 2D water flow over a flat plate of length L (see Fig. 4.1.). The boundary layer develops from the plate leading edge lying at the upstream computational domain boundary. The boundary layer at the leading edge is considered laminar. Then, at some distance from the plate leading edge the boundary layer automatically becomes turbulent (if this distance does not exceed L).

The SolidWorks model is shown in Fig. 4.2.. The problem is solved as internal in order to avoid a conflict situation in the corner mesh cell where the external flow boundary and the model wall intersect. In the internal flow problem statement, to avoid any influence of the upper model boundary or wall on the flow near the flat plate, the ideal wall boundary condition has been specified on the upper wall. The plate length is equal to 10 m, the channel height is equal to 2 m, the walls' thickness is equal to 0.5 m.

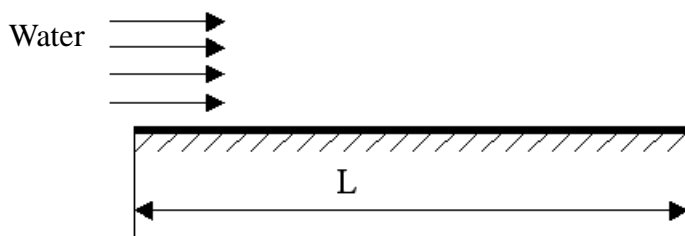


Fig. 4.1. Flow over a flat plate.

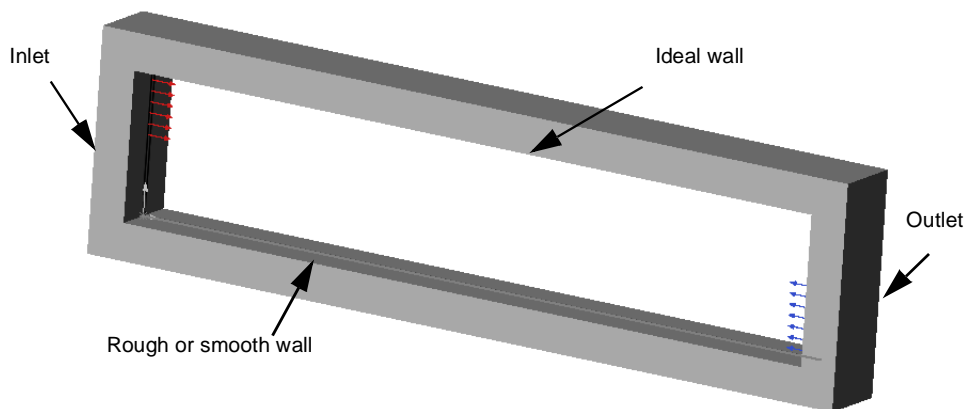


Fig. 4.2. The model for calculating the flow over the flat plate with Flow Simulation.

To solve the problem, an incoming uniform water flow of a certain velocity (see below), temperature of 293.2 K, turbulence intensity of 1%, and turbulence length of 0.01 m is specified at the channel inlet, whereas the water static pressure of 1 atm is specified at the channel outlet.

The flow computation is aimed at predicting the flat plate drag coefficient, defined as (see Refs. 1 and 4):

$$C_d = \frac{F}{\frac{\rho V^2}{2} A} ,$$

where F is the plate drag force, A is the plate surface area, ρ is fluid density, and V is the fluid velocity.

According to Refs.1 and 4, the plate drag coefficient value is governed by the Reynolds number, based on the distance L from the plate leading edge ($Re_L = \rho VL/\mu$, where ρ is the fluid density, V is the incoming uniform flow velocity, and μ is fluid dynamic viscosity), as well as by the relative wall roughness L/k , where k is the sand roughness. As a result, Refs.1 and 4 give us the semi-empirical flat plate $C_D(Re_L)$ curves obtained for different L/k from the generalized tubular friction factor curves and presented in Fig. 4.3.

(here, $\epsilon \equiv k$). If the boundary layer is laminar at the plate leading edge, then the wall roughness does not affect C_D until the transition from the laminar boundary layer to the turbulent one, i.e., the $C_D(Re_L)$ curve is the same as for a hydraulically smooth flat plate. The transition region's boundaries depend on various factors, the wall roughness among them. Here is shown the theoretical transition region for a hydraulically smooth flat plate. The transition region's boundary corresponding to fully turbulent flows (i.e., at the higher Re_L) is marked in Fig. 4.3. by a dashed line. At the higher Re_L , the semi-empirical theoretical curves have flat parts along which Re_L does not affect C_D at a fixed wall roughness. These flat parts of the semi-empirical theoretical curves have been obtained by a theoretical scaling of the generalized tubular friction factor curves to the flat plate conditions under the assumption of a turbulent boundary layer beginning from the flat plate leading edge.

To validate the Flow Simulation flat plate C_D predictions within a wide Re_L range, we have varied the incoming uniform flow velocity at the model inlet to obtain the Re_L values of 10^5 , $3 \cdot 10^5$, 10^6 , $3 \cdot 10^6$, 10^7 , $3 \cdot 10^7$, 10^8 , $3 \cdot 10^8$, 10^9 . To validate the wall roughness influence on C_D , the wall roughness k values of 0, 50, 200, 10^3 , $5 \cdot 10^3$, 10^4 μm have been considered. The Flow Simulation calculation results obtained at result resolution level 5 and compared with the semi-empirical curves are presented in Fig. 4.3..

As you can see from Fig. 4.3., $C_D(Re_L)$ of rough plates is somewhat underpredicted by Flow Simulation in the turbulent region, at $L/k \geq 1000$ the $C_D(Re_L)$ prediction error does not exceed about 12%.

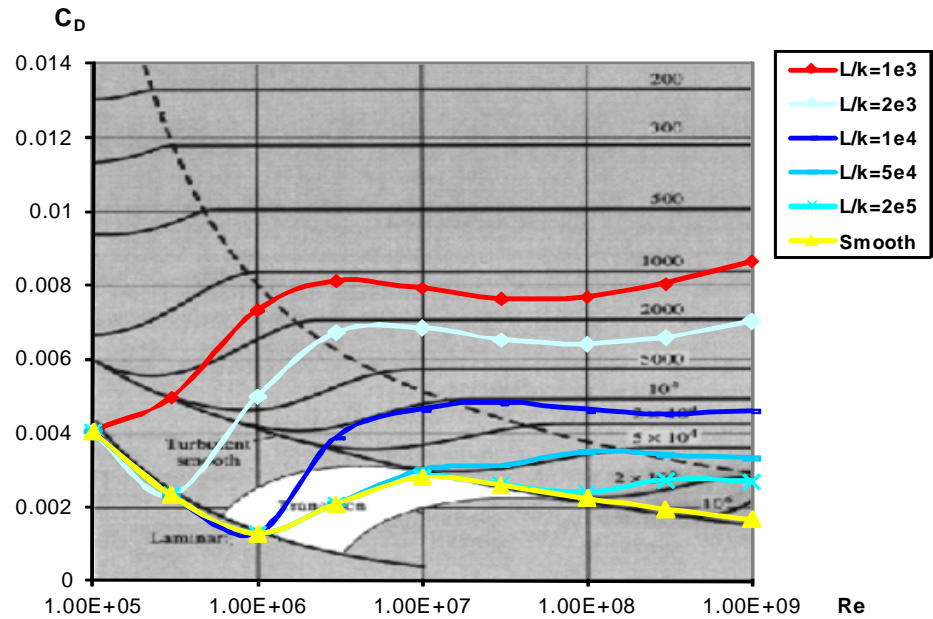


Fig. 4.3. The flat plate drag coefficient predicted with Flow Simulation for rough and hydraulically smooth flat plates in comparison with the semi-empirical curves (Refs.1 and 4).

5 Flow in a 90-degree Bend Square Duct

Following Ref.8, we will consider a steady-state flow of water (at 293.2 K inlet temperature and $U_{inlet} = 0.0198$ m/s inlet uniform velocity) in a 40x40 mm square cross-sectional duct having a 90°-angle bend with $r_i = 72$ mm inner radius ($r_o = 112$ mm outer radius accordingly) and attached straight sections of 1.8 m upstream and 1.2 m downstream (see Fig. 5.1.). Since the flow's Reynolds number, based on the duct's hydraulic diameter ($D=40$ mm), is equal to $Re_D = 790$, the flow is laminar.

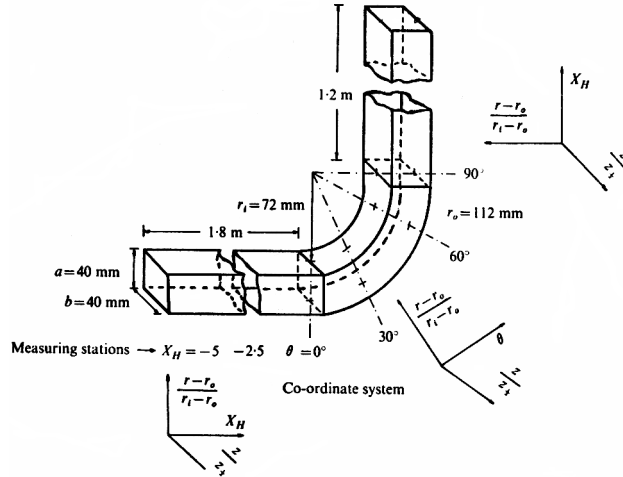


Fig. 5.1. The 90°-bend square duct's configuration indicating the velocity measuring stations and the dimensionless coordinates used for presenting the velocity profiles.

The predicted dimensionless (divided by U_{inlet}) velocity profiles are compared in Figs.5.2, 5.3 with the ones measured with a laser-Doppler anemometry at the following duct cross sections: $X_H = -5D, -2.5D, 0$ (or $\theta=0^\circ$) and at the $\theta=30^\circ, 60^\circ, 90^\circ$ bend sections. The z and

r directions are represented by coordinates $\frac{r - r_o}{r_i - r_o}$ and $\frac{z}{z_{1/2}}$, where $z_{1/2} = 20$ mm. The

dimensionless velocity isolines (with the 0.1 step) at the duct's $\theta= 60^\circ$ and 90° sections, both measured in Ref.8 and predicted with Flow Simulation, are shown in Figs.5.4 and 5.5.

It is seen that the Flow Simulation predictions are close to the Ref.8 experimental data.

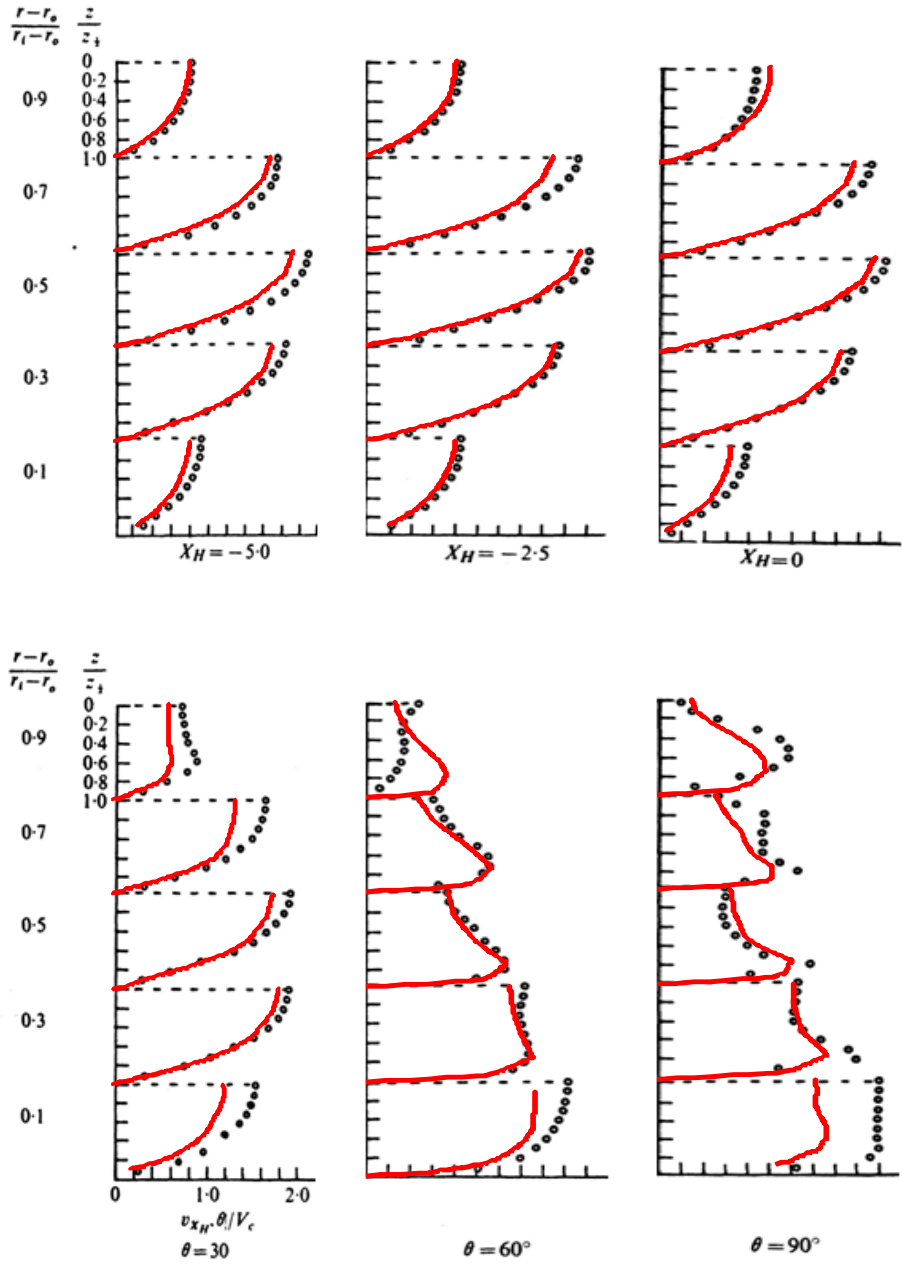
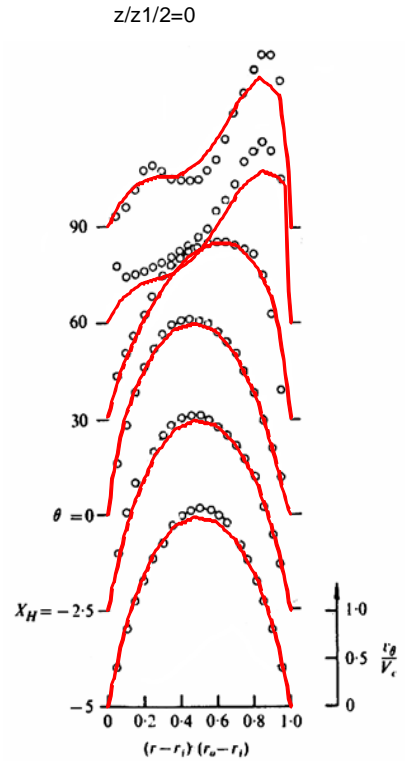
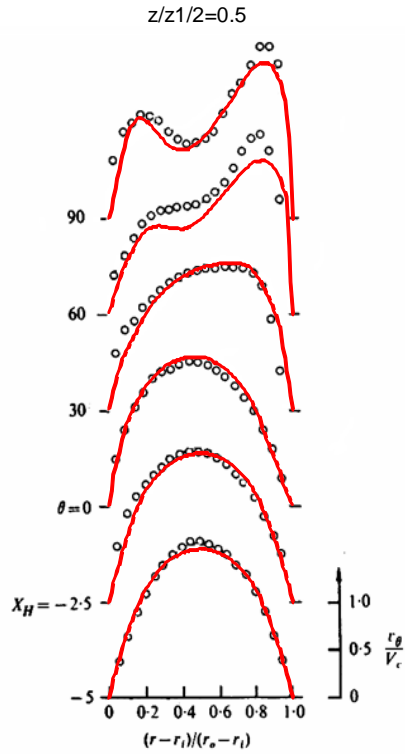


Fig. 5.2. The duct's velocity profiles predicted by Flow Simulation (red lines) in comparison with the Ref.8 experimental data (circles).



$z/z_{1/2}=0.5$

$z/z_{1/2}=0$

Fig. 5.3. The duct's velocity profiles predicted by Flow Simulation (red lines) in comparison with the Ref.8 experimental data (circles).

Isolines: V/Wc 60 []

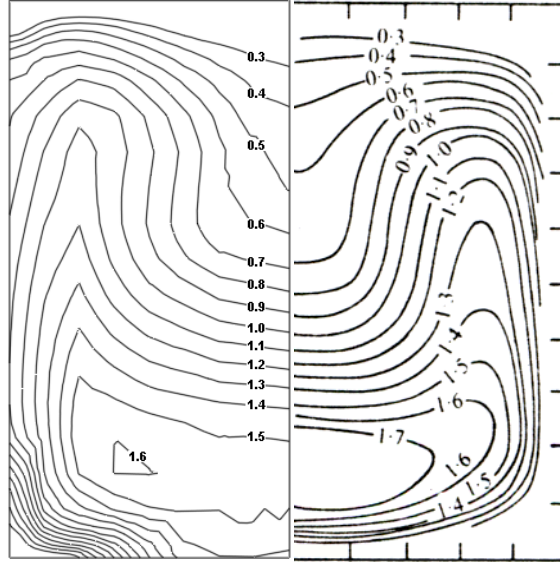


Fig. 5.4. The duct's velocity isolines at the $\theta = 60^\circ$ section predicted by Flow Simulation (left) in comparison with the Ref.8 experimental data (right).

Isolines: V/Wc 90 []

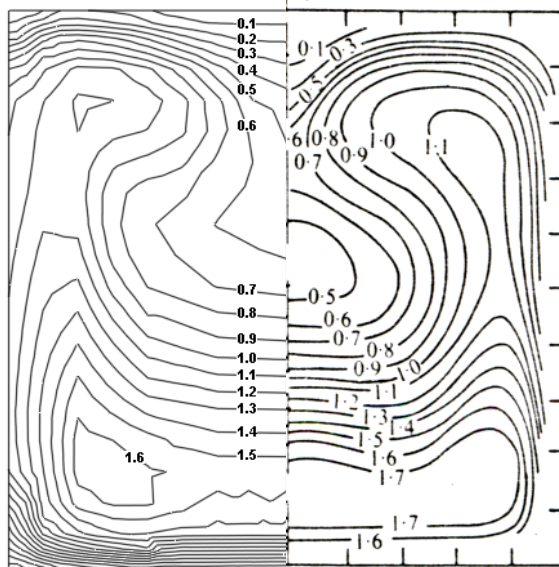


Fig. 5.5. The duct's velocity isolines at the $\theta = 90^\circ$ section predicted by Flow Simulation (left) in comparison with the Ref.8 experimental data (right).

6 Flows in 2D Channels with Bilateral and Unilateral Sudden Expansions

In this example we will consider both turbulent and laminar incompressible steady-state flows through 2D (plane) channels with bilateral and unilateral sudden expansions and parallel walls, as shown in Figs.6.1 and 6.2. At the 10 cm inlet height of the bilateral-sudden-expansion channels a uniform water stream at 293.2 K and 1 m/s is specified. The Reynolds number is based on the inlet height and is equal to $Re = 10^5$, therefore (since $Re > 10^4$) the flow is turbulent. At the 30 mm height inlet of the unilateral-sudden-expansion channel an experimentally measured water stream at 293.2 K and 8.25 mm/s mean velocity is specified, so the Reynolds number based on the inlet height is equal to $Re = 250$, therefore the flow is laminar. In both channels, the sudden expansion generates a vortex, which is considered in this validation from the viewpoint of hydraulic loss in the bilateral-expansion channel (compared to Ref.2) and from the viewpoint of the flow velocity field in the unilateral-expansion channel (compared to Ref.13).

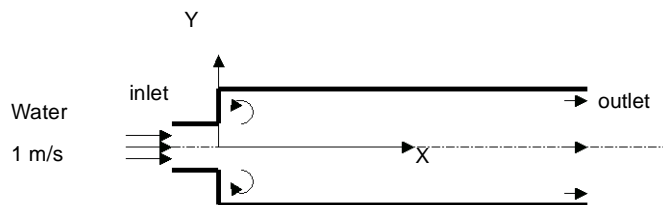


Fig. 6.1. Flow in a 2D (plane) channel with a bilateral sudden expansion.

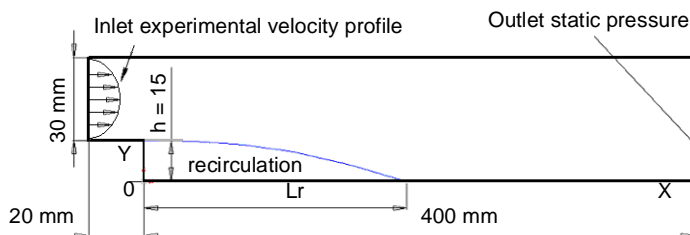


Fig. 6.2. Flow in a 2D (plane) channel with a unilateral sudden expansion.

Bilateral sudden expansion

In accordance with Ref.2, the local hydraulic loss coefficient of a bilateral sudden expansion (the so-called total pressure loss due to flow) for a turbulent ($Re > 10^4$) flow with a uniform inlet velocity profile depends only on the expansion area ratio and is determined from the following formula:

$$\zeta_s = \frac{P_0 - P_1}{\frac{\rho u_0^2}{2}} = \left(1 - \frac{A_0}{A_1}\right)^2,$$

where A_0 and A_1 are the inlet and outlet cross sectional areas respectively, P_0 and P_1 are the inlet and outlet total pressures, and $\rho u_0^2/2$ is the inlet dynamic head.

In a real sudden expansion the flow hydraulic loss coefficient is equal to $\zeta = \zeta_f + \zeta_s$, where ζ_f is the friction loss coefficient. In order to exclude ζ_f from our comparative analysis, we have imposed the ideal wall boundary condition on all of the channel walls.

In this validation example the channel expansion area ratios under consideration are: 1.5, 2.0, 3.0, and 6.0. To avoid disturbances at the outlet due to the sudden expansion, the channel length is 10 times longer than its height. The 1 atm static pressure is specified at the channel outlet.

The ζ_s values predicted by Flow Simulation at result resolution level 8 for different channel expansion area ratios A_0/A_1 are compared to theory in Fig. 6.3.

From Fig. 6.3., one can see that Flow Simulation overpredicts ζ_s by about 4.5...7.9 %.

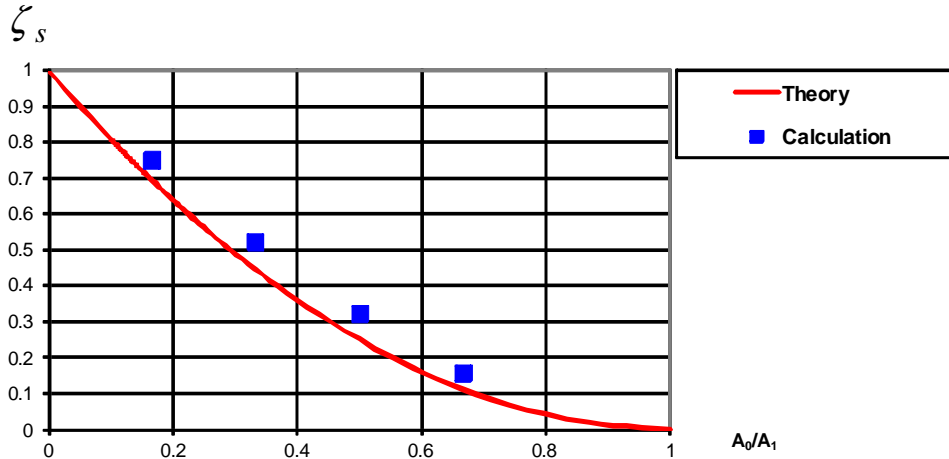


Fig. 6.3. Comparison of Flow Simulation calculations to the theoretical values (Ref.2) for the sudden expansion hydraulic loss coefficient versus the channel expansion area ratio.

Unilateral sudden expansion

The model used for the unilateral-sudden-expansion channel's flow calculation is shown in Fig. 6.4. The channel's inlet section has a 30 mm height and a 20 mm length. The channel's expanded section (downstream of the 15 mm height back step) has a 45 mm height and a 400 mm length (to avoid disturbances of the velocity field compared to the experimental data from the channel's outlet boundary condition). The velocity profile measured in the Ref.13 at the corresponding $Re_h = 125$ (the Reynolds number based on the step height) is specified as a boundary condition at the channel inlet. The 10^5 Pa static pressure is specified at the channel outlet.

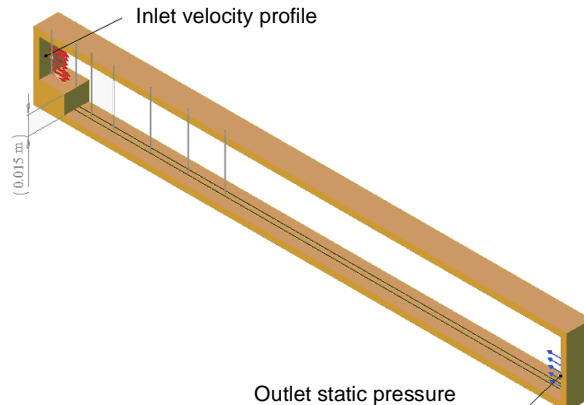


Fig. 6.4. The SolidWorks model for calculating the 2D flow in the unilateral-sudden-expansion channel with Flow Simulation.

The flow velocity field predicted by Flow Simulation at result resolution level 8 is compared in Figs.6.5, 6.6, and 6.7 to the values measured in Ref.13 with a laser anemometer. The flow X-velocity (u/U , where $U = 8.25$ mm/s) profiles at several $X = \text{const}$ (-20 mm, 0, 12 mm, ... 150 mm) cross sections are shown in Fig. 6.5. It is seen that the predicted flow velocity profiles are very close to the experimental values both in the main stream and in the recirculation zone. The recirculation zone's characteristics, i.e. its length L_R along the channel's wall, (plotted versus the Reynolds number Re_h based on the channel's step height h , where $Re_h = 125$ for the case under consideration), the separation streamline, and the vortex center are shown in Figs.6.6 and 6.7. It is seen that they are very close to the experimental data.

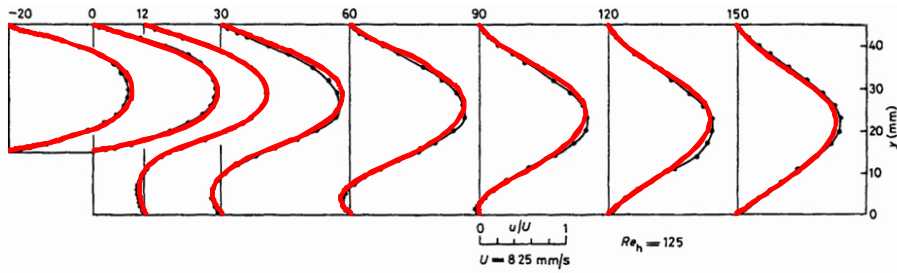


Fig. 6.5. The unilateral-sudden-expansion channel's velocity profiles predicted by Flow Simulation (red lines) in comparison with the Ref.13 experimental data (black lines with dark circles).

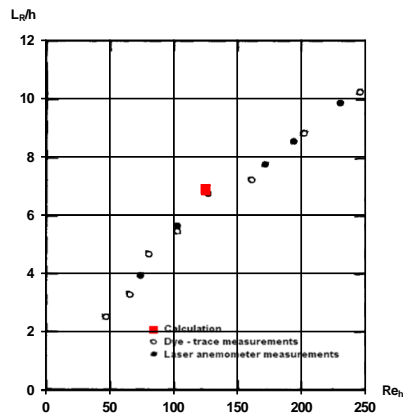


Fig. 6.6. The unilateral-sudden-expansion channel's recirculation zone length predicted by Flow Simulation (red square) in comparison with the Ref.13 experimental data (black signs).

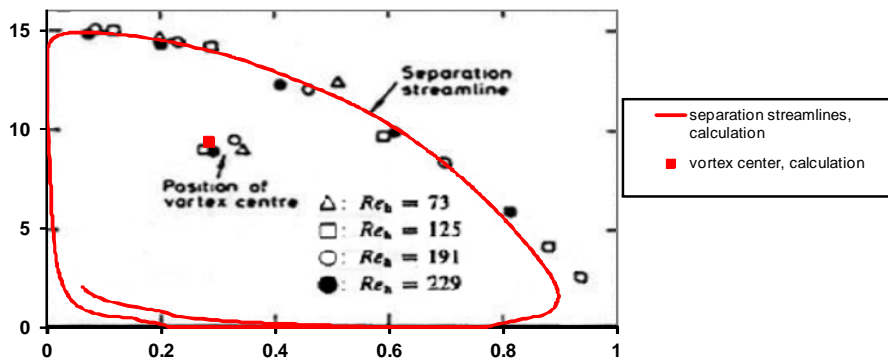


Fig. 6.7. The unilateral-sudden-expansion channel recirculation zone's separation streamlines and vortex center, both predicted by Flow Simulation (red lines and square) in comparison with the Ref.13 experimental data (black signs).

As one can see, both the integral characteristics (hydraulic loss coefficient) and local values (velocity profiles and recirculation zone geometry) of the turbulent and laminar flow in a 2D sudden expansion channel under consideration are adequately predicted by Flow Simulation.

7 Flow over a Circular Cylinder

Let us now consider an external incompressible flow example. In this example, water at a temperature of 293.2 K and a pressure of 1 atm flows over a cylinder of 0.01 m or 1 m diameter. The flow pattern of this example substantially depends on the Reynolds number which is based on the cylinder diameter. At low Reynolds numbers ($4 < Re < 60$) two steady vortices are formed on the rear side of the cylinder and remain attached to the cylinder, as it is shown schematically in Fig. 7.1. (see Refs.3).

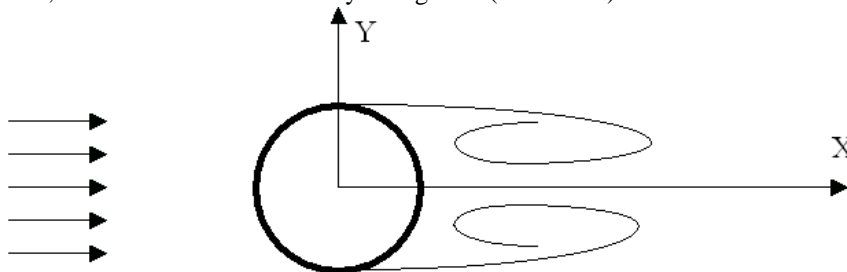


Fig. 7.1. Flow past a cylinder at low Reynolds numbers ($4 < Re < 60$).

At higher Reynolds numbers the flow becomes unstable and a von Karman vortex street appears in the wake past the cylinder. Moreover, at $Re > 60 \dots 100$ the eddies attached to the cylinder begin to oscillate and shed from the cylinder (Ref.3). The flow pattern is shown schematically in Fig. 7.2..

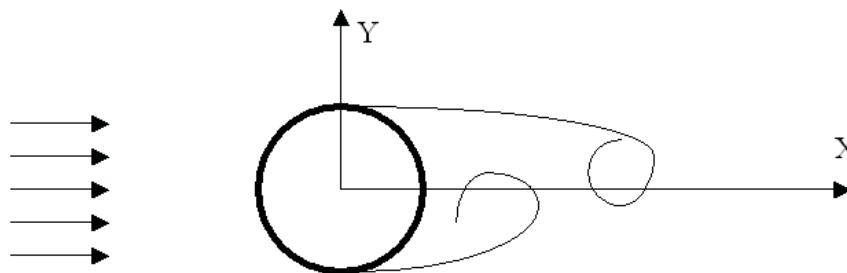


Fig. 7.2. Flow past a cylinder at Reynolds numbers $Re > 60 \dots 100$.

To calculate the 2D flow (in the X-Y plane) with Flow Simulation, the model shown in Fig. 7.3. has been created. The cylinder diameter is equal to 0.01 m at $Re \leq 10^4$ and 1 m at $Re > 10^4$. The incoming stream turbulence intensity has been specified as 0.1%. To take the flow's physical instability into account, the flow has been calculated by Flow Simulation using the time-dependent option. All the calculations have been performed at result resolution level 6.

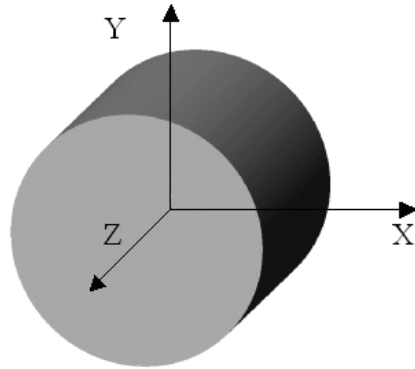


Fig. 7.3. The SolidWorks model used to calculate 2D flow over a cylinder.

In accordance with the theory, steady flow patterns have been obtained in these calculations in the low Re region. An example of such calculation at $Re=41$ is shown in Fig. 7.4. as flow trajectories over and past the cylinder in comparison with a photo of such flow from Ref.9. It is seen that the steady vortex past the cylinder is predicted correctly.

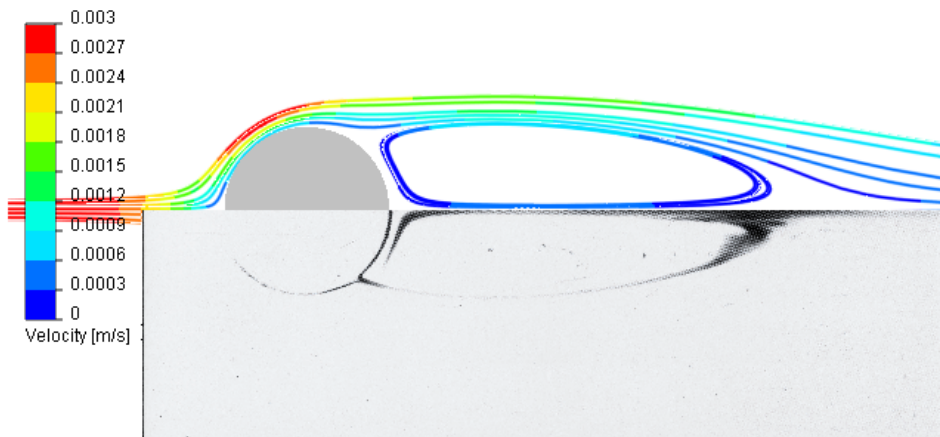


Fig. 7.4. Flow trajectories over and past a cylinder at $Re=41$ predicted with Flow Simulation (above) in comparison with a photo of such flow from Ref.9 (below).

The unsteady vortex shedding from a cylinder at $Re > 60..100$, yields oscillations of both drag and lateral forces acting on the cylinder and a von Karman vortex street is formed past the cylinder. An X-velocity field over and past the cylinder is shown in Fig. 7.5. The Flow Simulation prediction of the cylinder drag and lateral force oscillations' frequency in a form of Strouhal number ($Sh = D/(tU)$, where D is the cylinder diameter, t is the period of oscillations, and U is the incoming stream velocity) in comparison with experimental data for $Re \geq 10^3$ is shown in Fig. 7.6..

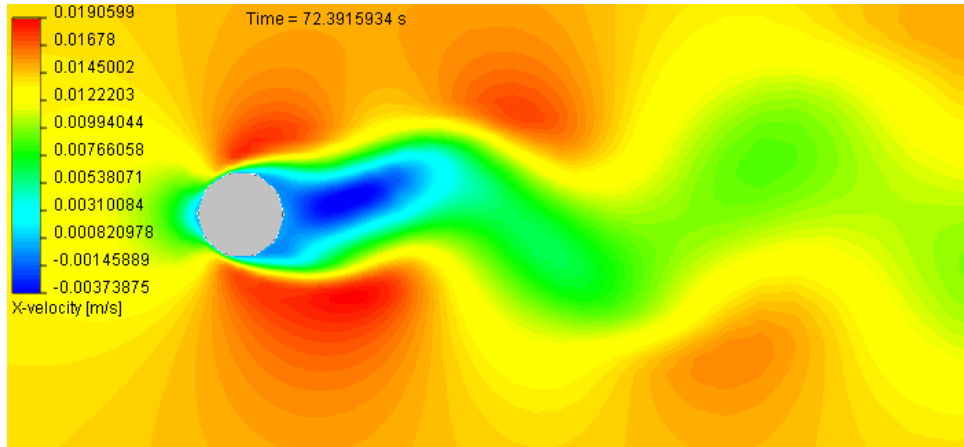


Fig. 7.5. Velocity contours of flow over and past the cylinder at $Re=140$.

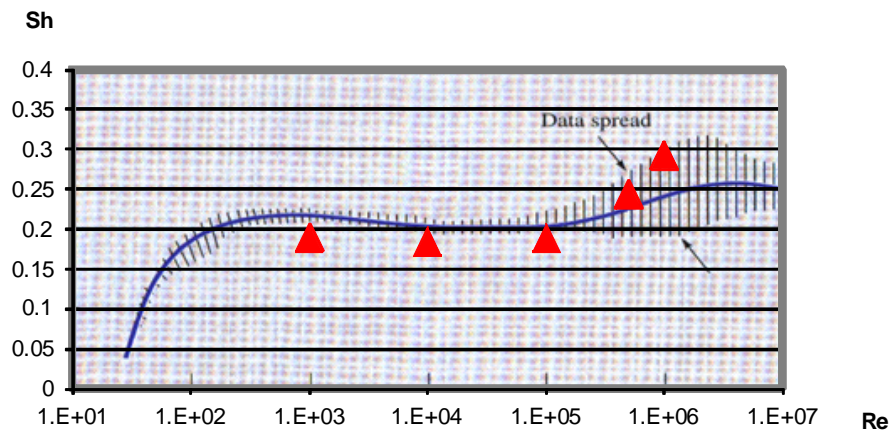


Fig. 7.6. The cylinder flow's Strouhal number predicted with Flow Simulation (red triangles) in comparison with the experimental data (blue line with dashes, Ref.4).

The time-averaged cylinder drag coefficient is defined as

$$C_D = \frac{F_D}{\frac{1}{2} \rho U^2 D L}$$

where F_D is the drag force acting on the cylinder, $\rho U^2/2$ is the incoming stream dynamic head, D is the cylinder diameter, and L is the cylinder length. The cylinder drag coefficient, predicted by Flow Simulation is compared to the well-known $C_D(\text{Re})$ experimental data in Fig. 7.7..

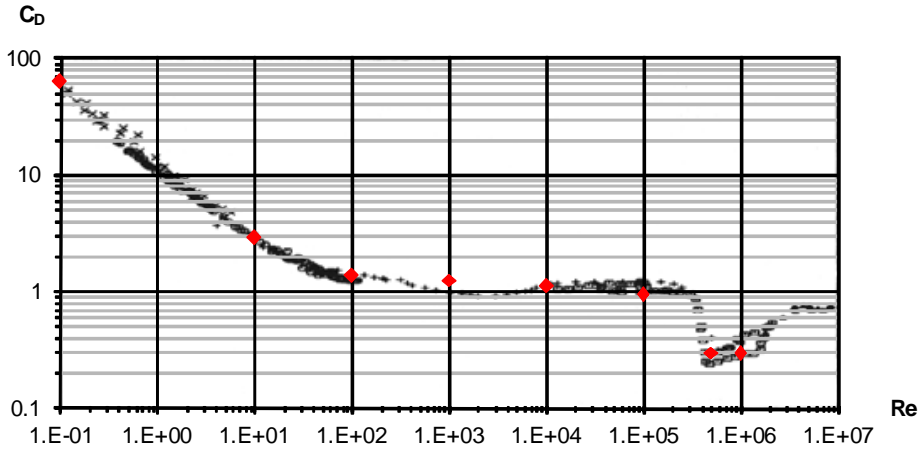


Fig. 7.7. The cylinder drag coefficient predicted by Flow Simulation (red diamonds) in comparison with the experimental data (black marks, Ref.3)

8 Supersonic Flow in a 2D Convergent-Divergent Channel

Now let us consider an external supersonic flow of air in a 2D (plane) convergent-divergent channel whose scheme is shown on Fig. 8.1.

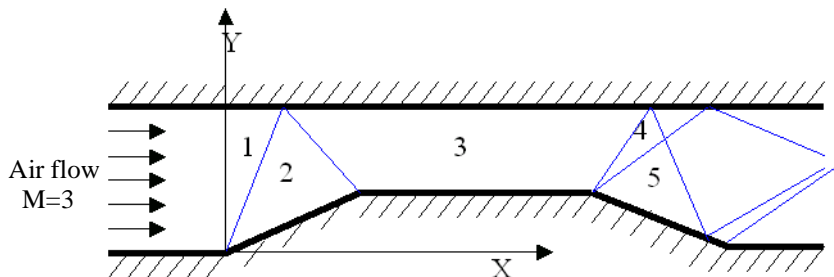


Fig. 8.1. Supersonic flow in a 2D convergent-divergent channel.

A uniform supersonic stream of air, having a Mach number $M=3$, static temperature of 293.2 K, and static pressure of 1 atm, is specified at the channel inlet between two parallel walls. In the next convergent section (see Fig. 8.2.) the stream decelerates through two oblique shocks shown schematically in Fig. 8.1. as lines separating regions 1, 2, and 3. Since the convergent section has a special shape adjusted to the inlet Mach number, so the shock reflected from the upper plane wall and separating regions 2 and 3 comes to the section 3 lower wall edge, a uniform supersonic flow occurs in the next section 3 between two parallel walls. In the following divergent section the supersonic flow accelerates thus forming an expansion waves fan 4. Finally, the stream decelerates in the exit channel section between two parallel walls when passing through another oblique shock.

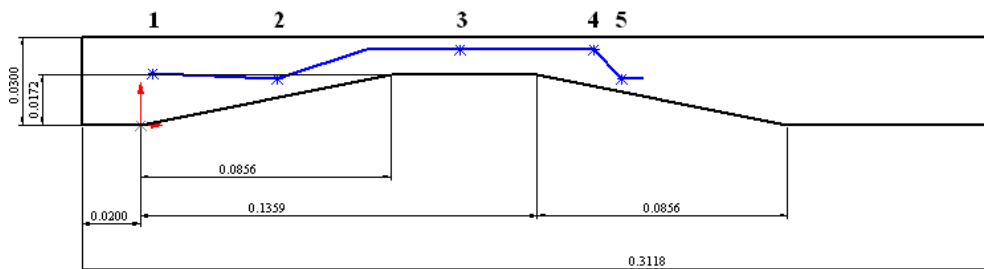


Fig. 8.2. Dimensions (in m) of the 2D convergent-divergent channel including a reference line for comparing the Mach number.

The SolidWorks model of this 2D channel is shown in Fig. 8.3.

Since the channel was designed for the inviscid flow of an ideal gas, the ideal wall boundary condition has been specified and the laminar only flow has been considered instead of turbulent. The computed Mach number along the reference line and at the reference points (1-5) are compared with the theoretical values in Fig. 8.4..

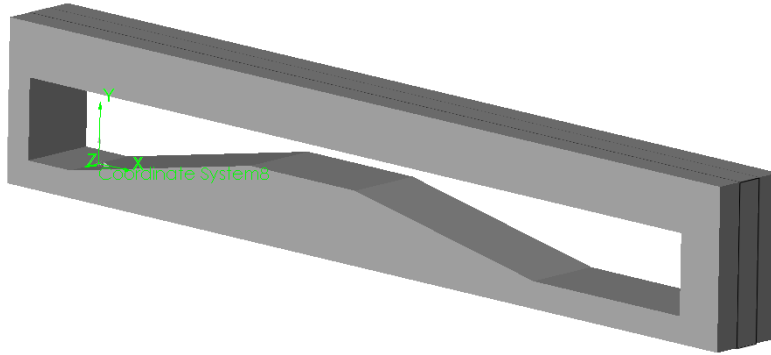


Fig. 8.3. The model for calculating the 2D supersonic flow in the 2D convergent-divergent channel with Flow Simulation.

To obtain the most accurate results possible with Flow Simulation, the calculations have been performed at result resolution level 6. The predicted Mach number at the selected channel points (1-5) and along the reference line (see Fig. 8.2.), are presented in Table 8.3 and Fig. 8.4. respectively.

Table 8.3 Mach number values predicted with Flow Simulation with comparison to the theoretical values at the reference points.

Point	1	2	3	4	5
X coordinate of point, m	0.0042	0.047	0.1094	0.155	0.1648
Y coordinate of point, m	0.0175	0.0157	0.026	0.026	0.0157
Theoretical M	3.000	2.427	1.957	2.089	2.365
Flow Simulation prediction of M	3.000	2.429	1.965	2.106	2.380
Prediction error, %	0.0	0.1	0.4	0.8	0.6

From Table 8.3 and Fig. 8.4. it can be seen that the Flow Simulation predictions are very close to the theoretical values. In Fig. 8.4. one can see that Flow Simulation properly predicts the abrupt parameter changes when the stream passes through the shock and a fast parameter change in the expansion fan.

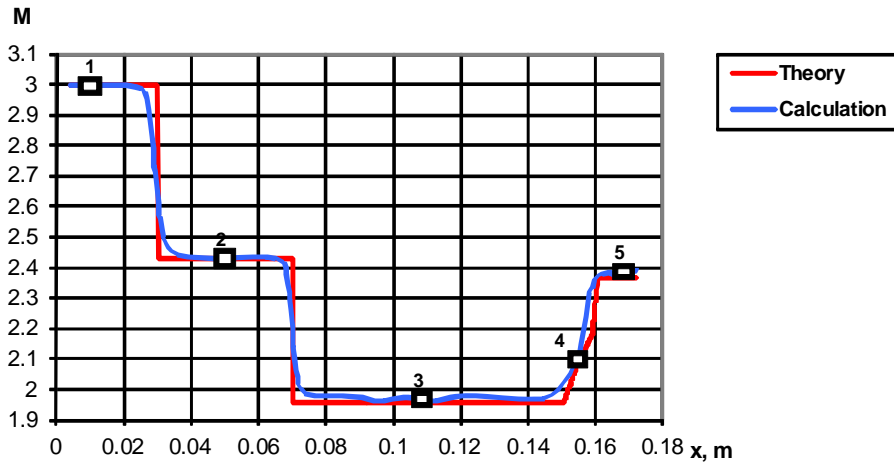


Fig. 8.4. Mach number values predicted with Flow Simulation along the reference line (the reference points on it are marked by square boxes with numbers) in comparison with the theoretical

To show the full flow pattern, the predicted Mach number contours of the channel flow are shown in Fig. 8.5..

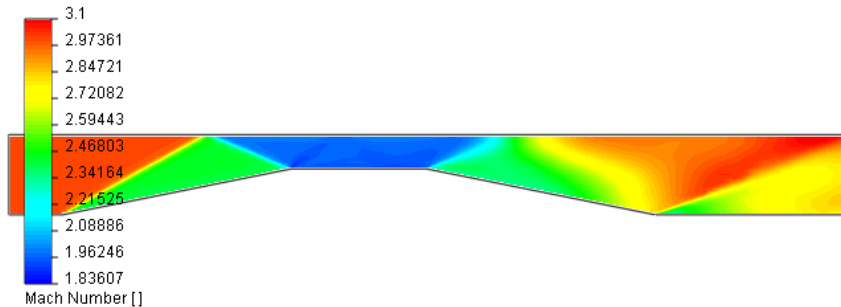


Fig. 8.5. Mach number contours predicted by Flow Simulation.

This example illustrates that Flow Simulation is capable of capturing shock waves with a high degree of accuracy. This high accuracy is possible due to the Flow Simulation solution adaptive meshing capability. Solution adaptive meshing automatically refines the mesh in regions with high flow gradients such as shocks and expansion fans.

9 Supersonic Flow over a Segmental Conic Body

Now let us consider an external supersonic flow of air over a segmental conic body shown in Fig. 9.1. The general case is that the body is tilted at an angle of α with respect to the incoming flow direction. The dimensions of the body whose longitudinal (in direction t , see Fig. 9.1.) and lateral (in direction n) aerodynamic drag coefficients, as well as longitudinal (with respect to Z axis) torque coefficient, were investigated in Ref.5 are presented in Fig. 9.2. They were determined from the dimensionless body sizes and the Reynolds number stated in Ref.5.

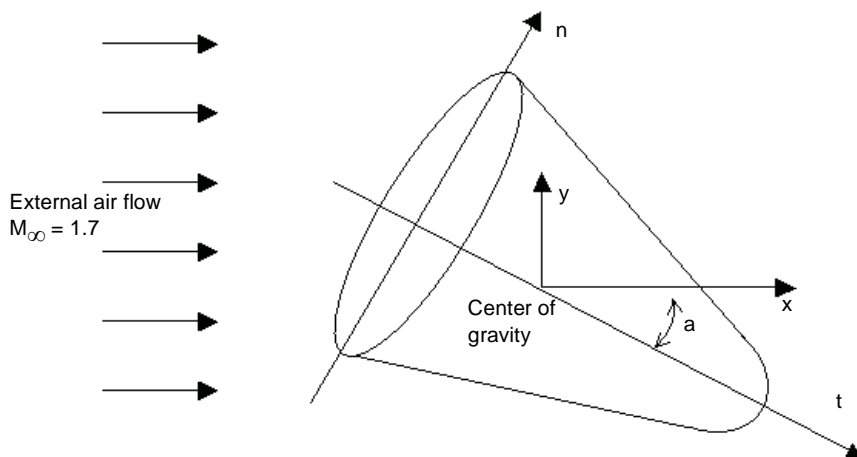


Fig. 9.1. Supersonic flow over a segmental conic body.

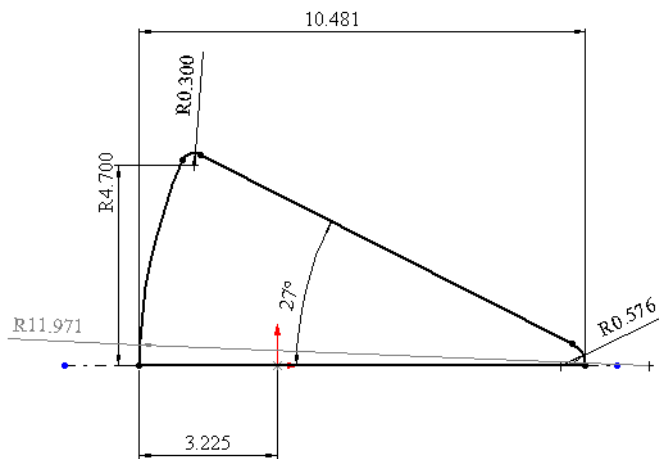


Fig. 9.2. Model sketch dimensioned in centimeters.

The model of this body is shown in Fig. 9.3..

To compare the Flow Simulation predictions with the experimental data of Ref.5, the calculations have been performed for the case of incoming flow velocity of Mach number 1.7. The undisturbed turbulent incoming flow has a static pressure of 1 atm, static temperature of 660.2 K, and turbulence intensity of 1%. The flow Reynolds number of 1.7×10^6 (defined with respect to the body frontal diameter) corresponds to these conditions, satisfying the Ref.5 experimental conditions.

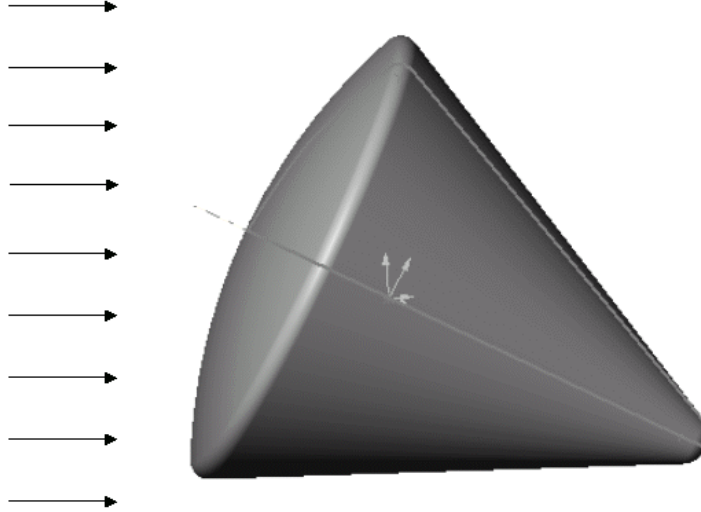


Fig. 9.3. The SolidWorks model for calculating the 3D flow over the 3D segmental conic body with Flow Simulation.

To compare the flow prediction with the experimental data of Ref.5, the calculations have been performed for the body tilted at $\alpha = 0^\circ, 30^\circ, 60^\circ, 90^\circ, 120^\circ, 150^\circ$ and 180° angles. To reduce the computational resources, the $Z = 0$ flow symmetry plane has been specified in all of the calculations. Additionally, the $Y = 0$ flow symmetry plane has been specified at $\alpha = 0^\circ$ and 180° .

The calculations have been performed at result resolution level 6.

The comparison is performed on the following parameters:

- longitudinal aerodynamic drag coefficient,

$$C_t = \frac{F_t}{\frac{1}{2} \rho U^2 S} ,$$

where F_t is the aerodynamic drag force acting on the body in the t direction (see Fig. 9.1.), $\rho U^2 / 2$ is the incoming stream dynamic head, S is the body frontal cross section (being perpendicular to the body axis) area;

- lateral aerodynamic drag coefficient,

$$C_n = \frac{F_n}{\frac{1}{2} \rho U^2 S} ,$$

where F_n is the aerodynamic drag force acting on the body in the n direction (see Fig. 9.1.), $\rho U^2/2$ is the incoming stream dynamic head, S is the body frontal cross section (being perpendicular to the body axis) area;

- on the longitudinal (with respect to Z axis) aerodynamic torque coefficient,

$$m_z = \frac{M_z}{\frac{1}{2} \rho U^2 S L} ,$$

where M_z is the aerodynamic torque acting on the body with respect to the Z axis (see Fig. 9.1.), $\rho U^2/2$ is the incoming stream dynamic head, S is the body frontal cross section (being perpendicular to the body axis) area, L is the reference length.

The calculation results are presented in Figs.9.4 and 9.5.

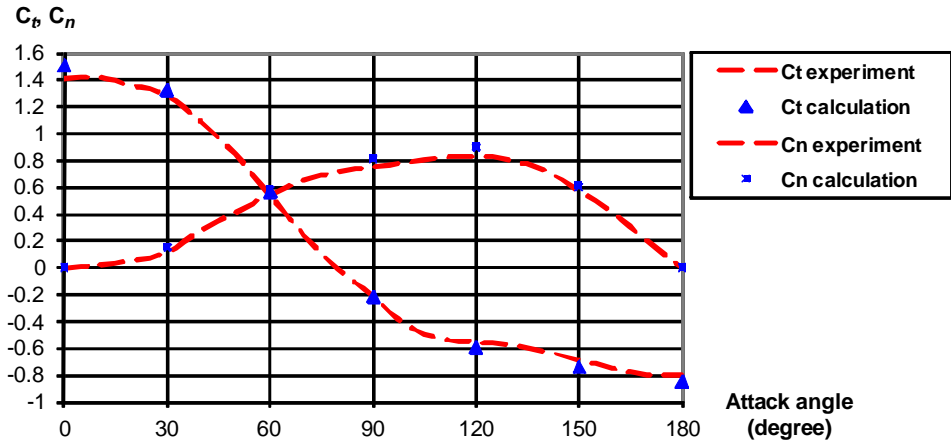


Fig. 9.4. The longitudinal and lateral aerodynamic drag coefficients predicted with Flow Simulation and measured in the experiments of Ref.5 versus the body tilting angle.

From Fig. 9.4., it is seen that the Flow Simulation predictions of both C_n and C_t are excellent.

As for the longitudinal aerodynamic torque coefficient (m_z) prediction, it is also close to the experimental data of Ref.5, especially if we take into account the measurements error.

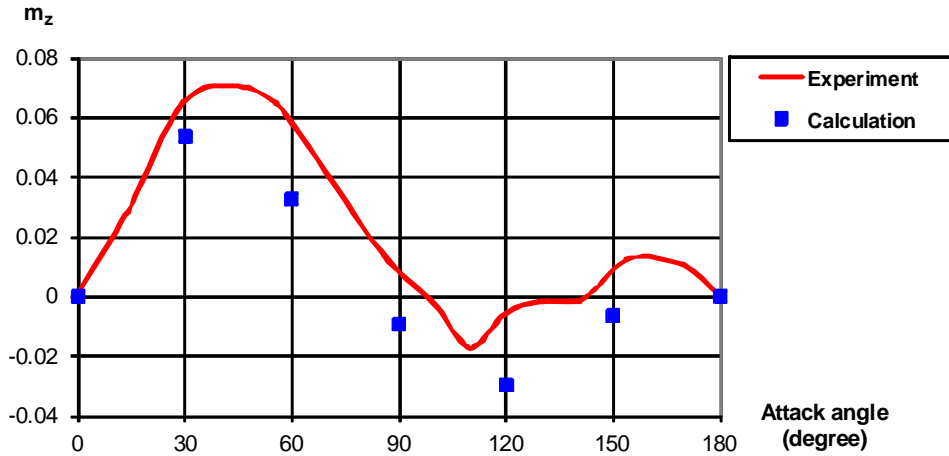


Fig. 9.5. The longitudinal aerodynamic torque coefficient predicted with Flow Simulation and measured in the experiments (Ref.5) versus the body tilting angle.

To illustrate the quantitative predictions with the corresponding flow patterns, the Mach number contours are presented in Figs. 9.6, 9.7, and 9.8. All of the flow patterns presented on the figures include both supersonic and subsonic flow regions. The bow shock consists of normal and oblique shock parts with the subsonic region downstream of the normal shock. In the head subsonic region the flow gradually accelerates up to a supersonic velocity and then further accelerates in the expansion fan of rarefaction waves. The subsonic wake region past the body can also be seen.

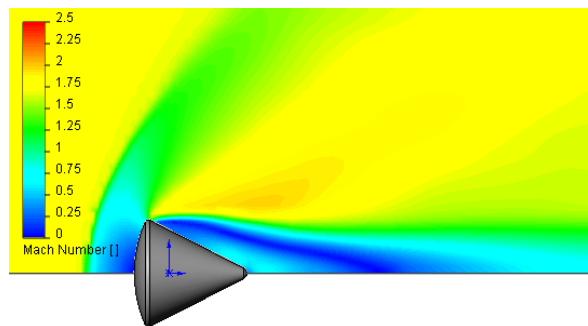


Fig. 9.6. Mach number contours at $\alpha = 0^\circ$.

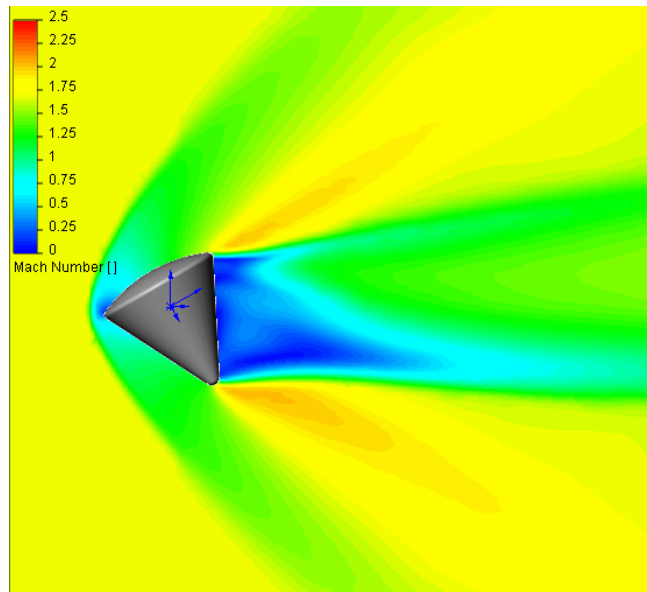


Fig. 9.7. Mach number contours at $\alpha = 60^\circ$.

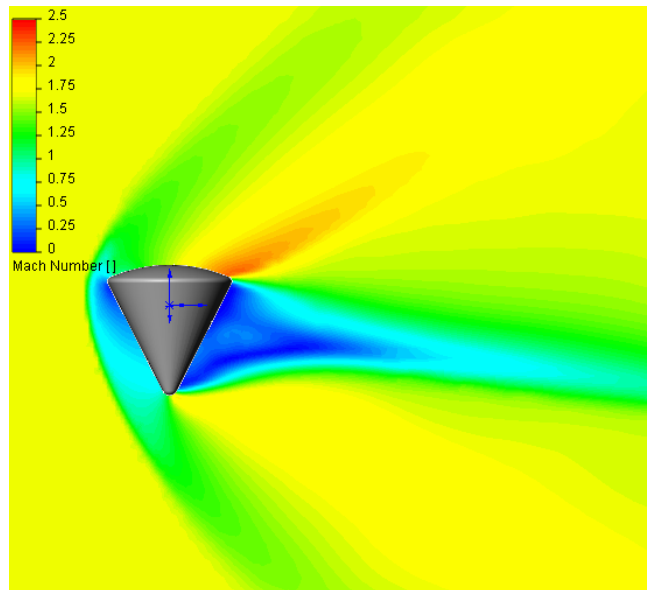


Fig. 9.8. Mach number contours at $\alpha = 90^\circ$.

As the forward part becomes sharper, the normal part of the bow shock and the corresponding subsonic region downstream of it become smaller. In the presented pictures, the smallest nose shock (especially its subsonic region) is observed at $\alpha = 60^\circ$.

10 Flow over a Heated Plate

Now let us consider a uniform 2D flows with a laminar boundary layer on a heated flat plate, see Fig. 10.1.. The incoming uniform air stream has a velocity of 1.5 m/s, a temperature of 293.2 K, and a static pressure of 1 atm. Thus, the flow Reynolds number defined on the incoming flow characteristics and on the plate length of 0.31 m is equal to $3.1 \cdot 10^4$, therefore the boundary layer beginning from the plate's leading edge is laminar (see Ref.6).

Then, let us consider the following three cases:

Case #1

The plate over its whole length (within the computational domain) is 10°C warmer than the incoming air (303.2 K), both the hydrodynamic and the thermal boundary layer begin at the plate's leading edge coinciding with the computational domain boundary;

Case #2

The upstream half of the plate (i.e. at $x \sim 0.15$ m) has a fluid temperature of 293.2 K, and the downstream half of the plate is 10°C warmer than the incoming air (303.2 K), the hydrodynamic boundary layer begins at the plate's leading edge coinciding with the computational domain boundary;

Case #3

Plate temperature is the same as in case #1, the thermal boundary layer begins at the inlet computational domain boundary, whereas the hydrodynamic boundary layer at the inlet computational domain boundary has a non-zero thickness which is equal to that in case #2 at the thermal boundary layer starting.

The calculation goal is to predict the local coefficient of heat transfer from the wall to the fluid, as well as the local skin-friction coefficient.

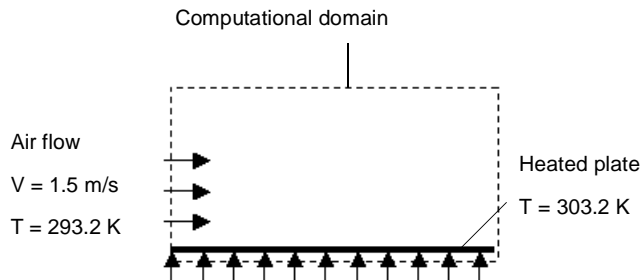


Fig. 10.1. Laminar flow over a heated flat plate.

The SolidWorks model used for calculating the 2D flow over the heated flat plate with Flow Simulation is shown in Fig. 10.2.. The problem is solved as internal in order to avoid the conflict situation when the external flow boundary with ambient temperature conditions intersects the wall with a thermal boundary layer.

To avoid any influence of the upper wall on the flow near the heated lower wall, the ideal wall boundary condition has been specified on the upper wall. To solve the internal problem, the incoming fluid velocity is specified at the channel inlet, whereas the fluid static pressure is specified at the channel exit. To specify the external flow features, the incoming stream's turbulent intensity is set to 1% and the turbulent length is set to 0.01 m, i.e., these turbulent values are similar to the default values for external flow problems.

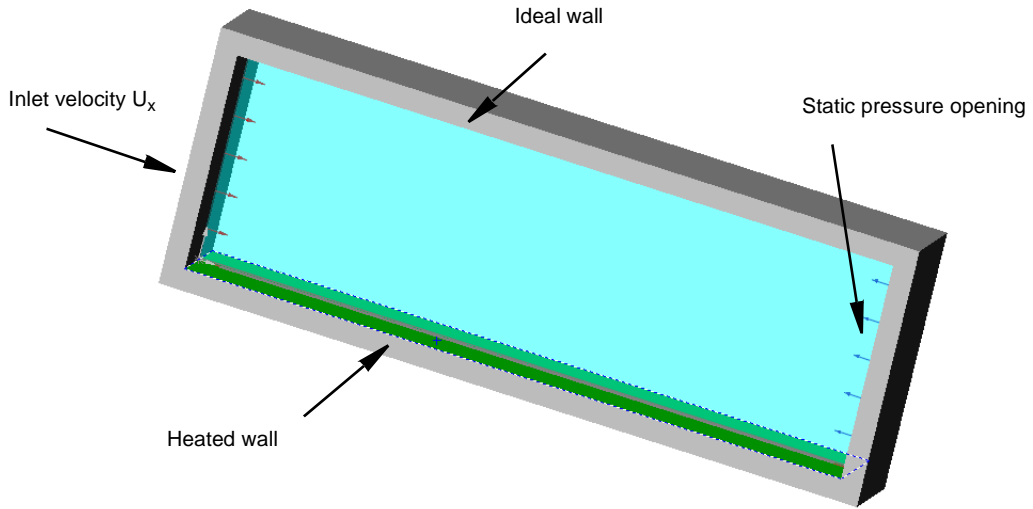


Fig. 10.2. The SolidWorks model used for calculating the 2D flow over heated flat plate with Flow Simulation.

The heat transfer coefficient h and the skin-friction coefficient C_f are Flow Simulation output flow parameters. The theoretical values for laminar flow boundary layer over a flat plate, in accordance with Ref.6 can be determined from the following equations:

$$h = \frac{kNu_x}{x} ,$$

where

k is the thermal conductivity of the fluid,

x is the distance along the wall from the start of the hydrodynamic boundary layer,

Nu_x is the Nusselt number defined on a heated wall as follows:

$$Nu_x = 0.332 \cdot Pr^{1/3} Re_x^{1/2}$$

for a laminar boundary layer if it's starting point coincides with the thermal boundary layer starting point, and

$$Nu_x = \frac{0.332 \cdot Pr^{1/3} Re_x^{1/2}}{\sqrt[3]{1 - (x_0/x)^{3/4}}}$$

for a laminar boundary layer if the thermal boundary layer begins at point x_0 lying downstream of the hydrodynamic boundary layer starting point, in this case Nu_x is defined at $x > x_0$ only;

where $Pr = \frac{\mu C_p}{k}$ is the Prandtl number, μ is the fluid dynamic viscosity, C_p is the

fluid specific heat at constant pressure, $Re_x = \frac{\rho V x}{\mu}$ is the Reynolds number

defined on x , ρ is the fluid density, and V is the fluid velocity;

$$C_{fx} = \frac{0,664}{\sqrt{Re_x}} \text{ at } Re_x \leq 5 \cdot 10^5, \text{ i.e., with a laminar boundary layer.}$$

As for the hydrodynamic boundary layer thickness δ needed for specification at the computational domain boundary in case #3, in accordance with Ref.6, it has been determined from the following equation: $\delta = 4.64 \cdot x / Re_x^{0.5}$, so $\delta = 0.00575$ m in this case. For these calculations all fluid parameters are determined at the outer boundary of the boundary layer.

The Flow Simulation predictions of h and C_f performed at result resolution level 7, and the theoretical curves calculated with the formulae presented above are shown in Figs.10.3 and 10.4. It is seen that the Flow Simulation predictions of the heat transfer coefficient and the skin-friction coefficient are in excellent agreement with the theoretical curves.

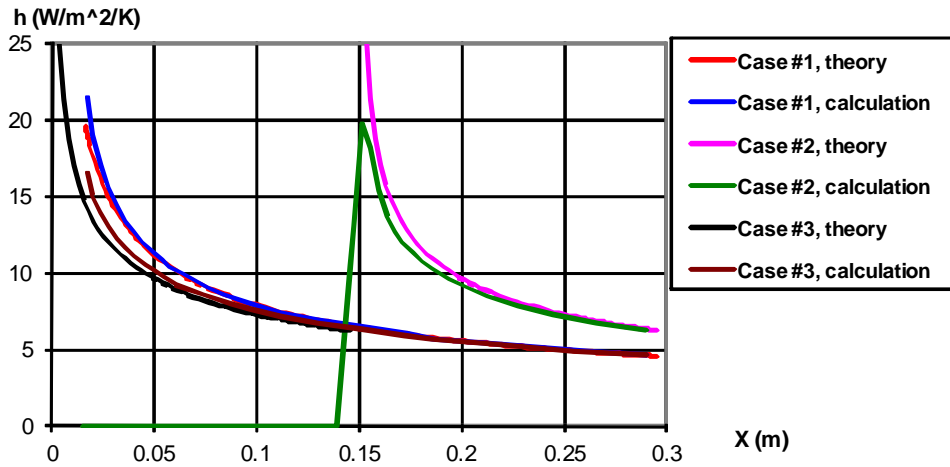


Fig. 10.3. Heat transfer coefficient change along a heated plate in a laminar boundary layer: Flow Simulation predictions compared to theory.

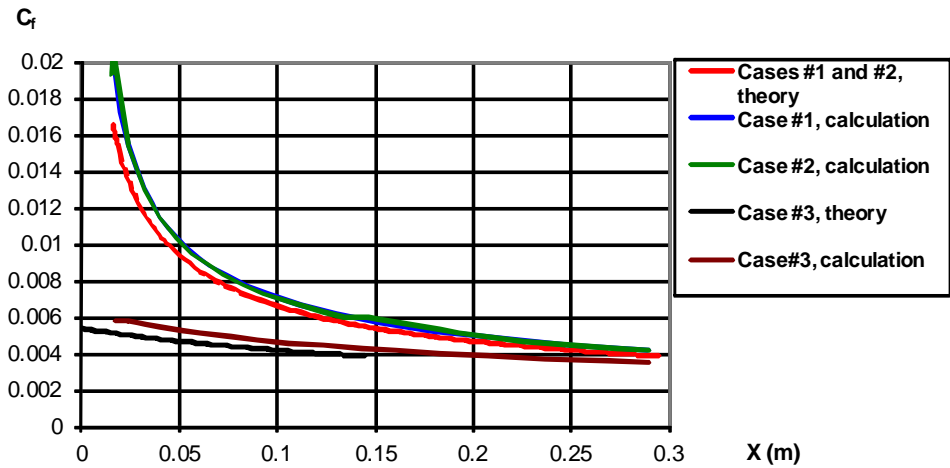


Fig. 10.4. Skin-friction coefficient change along a heated plate in a laminar boundary layer: Flow Simulation predictions compared to theory.

11 Convection and Radiation in an Annular Tube

We will now consider incompressible laminar flow in a portion of an annular tube, whose outer shell is a heat source having constant heat generation rate Q_1 with a heat-insulated outer surface, and whose central body fully absorbs the heat generated by the tube's outer shell (i.e. the negative heat generation rate Q_2 is specified in the central body); see Fig. 11.1.. (The tube model is shown in Fig. 11.2.). We will assume that this tube is rather long, so the tube's $L=1$ m portion under consideration has fully developed fluid velocity and temperature profiles at the inlet, and, since the fluid properties are not temperature-dependent, the velocity profile also will not be temperature-dependent.

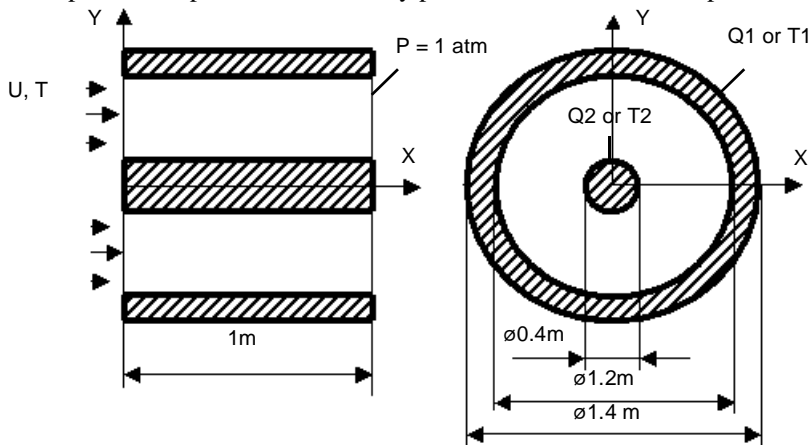


Fig. 11.1. Laminar flow in a heated annular tube.

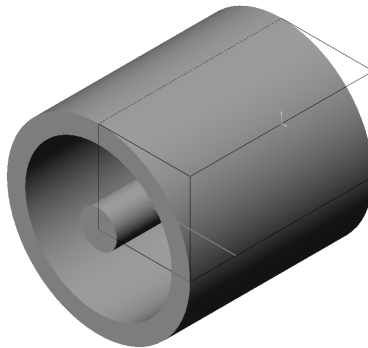


Fig. 11.2. A model created for calculating 3D flow within a heated annular tube using Flow Simulation.

To validate the Flow Simulation capability for solving conjugate heat transfer problems both with and without radiation, let us solve the following three problems: 1) a conjugate heat transfer problem with convection only, 2) radiation heat transfer only problem, and 3) a conjugate heat transfer problem with both convection and radiation.

In the first problem we specify $Q_2 = -Q_1$, so the convective heat fluxes at the tube inner and outer walls are constant along the tube. The corresponding laminar annular pipe flow's fully developed velocity and temperature profiles, according to Ref.6, are expressed analytically as follows:

$$u(r) = \varphi \cdot \left[\left(\frac{r}{r_2} \right)^2 - \left(\left(\frac{r_1}{r_2} \right)^2 - 1 \right) \frac{\ln(r/r_2)}{\ln(r_1/r_2)} - 1 \right],$$

$$T(r) = T_2 - \frac{q_2}{k} r_2 \ln \left(\frac{r}{r_2} \right),$$

$$\text{where } \varphi = \frac{2 \bar{u}}{\left(\left(\frac{r_1}{r_2} \right)^2 - 1 \right) / \ln(r_1/r_2) - \left(\frac{r_1}{r_2} \right)^2 - 1},$$

u is the fluid velocity,

T is the fluid temperature,

r is the radial coordinate,

r_1 and r_2 are the tube outer shell's inner radius and tube's central body radius, respectively,

\bar{u} is the volume-average velocity, defined as the volume flow rate divided by the tube cross-section area,

q_2 is the the heat flux from the fluid to the tube's central body,

k is the fluid thermal conductivity,

T_2 is the surface temperature of the central body.

The heat flux from the fluid to the tube's central body (negative, since the heat comes from the fluid to the solid) is equal to

$$q_2 = k \left(\frac{\partial T}{\partial r} \right)_{r=r_2} = \frac{Q_2}{2\pi \cdot r_2 \cdot L}$$

Let $Q_1 = -Q_2 = 107.235 \text{ W}$ and $\bar{u} \approx 13.59 \text{ m/s}$ ($\varphi = -10 \text{ m/s}$), the fluid has the following properties: $k = 0.5 \text{ W/(m}\cdot\text{K)}$, $C_p = 500 \text{ J/(kg}\cdot\text{K)}$, $\mu = 0.002 \text{ Pa}\cdot\text{s}$, $\rho = 0.1 \text{ kg/m}^3$. Since the corresponding (defined on the equivalent tube diameter) Reynolds number $Re_d \approx 815$ is rather low, the flow has to be laminar. We specify the corresponding velocity and temperature profiles as boundary conditions at the model inlet and as initial conditions, and $P_{\text{out}} = 1 \text{ atm}$ as the tube outlet boundary condition.

To reduce the computational domain, let us set $Y=0$ and $X=0$ flow symmetry planes (correspondingly, the specified Q_1 and Q_2 values are referred to the tube section's quarter lying in the computational domain). The calculation have been performed at result resolution level 6.

The fluid temperature profile predicted at 0.75 m from the tube model inlet is shown in Fig. 11.3. together with the theoretical curve.

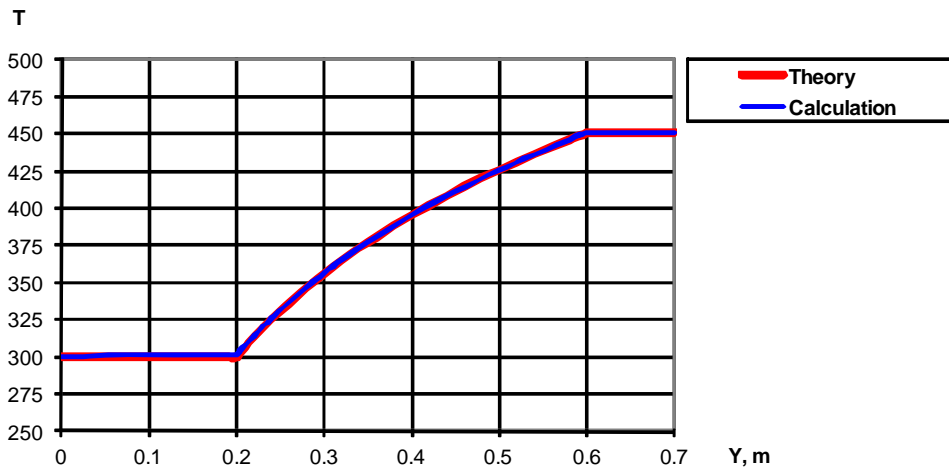


Fig. 11.3. Fluid temperature profiles across the tube in the case of convection only, predicted with Flow Simulation and compared to the theoretical curve.

It is seen that this prediction practically coincides with the theoretical curve.

Before solving the third problem coupling convection and radiation, let us determine the radiation heat fluxes between the tube's outer and inner walls under the previous problem's wall temperatures. In addition to holding the outer shell's temperature at 450 K and the central body's temperature at 300 K as the volume sources, let us specify the emissivity of $\epsilon_1 = 0.95$ for the outer shell and $\epsilon_2 = 0.25$ for the central body. To exclude any convection, let us specify the liquid velocity of 0.001 m/s and thermal conductivity of $10^{-20} \text{ W/(m}\cdot\text{K)}$.

Let J_2 denote the radiation rate leaving the central body, and G_2 denotes the radiation rate coming to the central body, therefore $Q_{2r} = J_2 - G_2$ (the net radiation rate from the central body). In the same manner, let J_1 denote the radiation rate leaving the outer shell's inner surface, and G_1 denote the radiation rate coming to the outer shell's inner surface, therefore $Q_{1r} = J_1 - G_1$ (the net radiation rate from the outer shell's inner surface). These radiation rates can be determined by solving the following equations:

$$\begin{aligned}
J_2 &= A_2 \sigma \epsilon_2 T_2^4 + G_2(1-\epsilon_2), \\
G_2 &= J_1 F_{1-2}, \\
J_1 &= A_1 \sigma \epsilon_1 T_1^4 + G_1(1-\epsilon_1), \\
G_1 &= J_2 F_{2-1} + J_1 F_{1-1},
\end{aligned}$$

where $\sigma = 5.669 \cdot 10^{-8} \text{ W/m}^2 \cdot \text{K}^4$ is the Stefan-Boltzmann constant, F_{1-2} , F_{2-1} , F_{1-1} are these surfaces' radiation shape factors, under the assumption that the leaving and incident radiation fluxes are uniform over these surfaces, Ref.6 gives the following formulas:

$$F_{1-2} = (1/X) - (1/\pi X) \{ \arccos(B/A) - (1/2/Y) [(A^2 + 4A - 4X^2 + 4)^{1/2} \arccos(B/X/A) + B \cdot \arcsin(1/X) - \pi A/2] \},$$

$$F_{1-1} = 1 - (1/X) + (2/\pi X) \arctan[2(X^2 - 1)^{1/2}/Y] - (Y/2/\pi X) \{ [(4X^2 + Y^2)^{1/2}/Y] \arcsin\{ [4(X^2 - 1) + (Y/X)^2(X^2 - 2)]/[Y^2 + 4(X^2 - 1)] \} - \arcsin[(X^2 - 2)/X^2] + (\pi/2)[(4X^2 + Y^2)^{1/2}/Y - 1] \}$$

$$F_{2-1} = F_{1-2} \cdot A_1/A_2, \text{ where } X = r_1/r_2, Y = L/r_2, A = X^2 + Y^2 - 1, B = Y^2 - X^2 + 1.$$

These net and leaving radiation rates (over the full tube section surface), both calculated by solving the equations analytically and predicted by Flow Simulation at result resolution level 6, are presented in Table .11.4.

Table .11.4 Radiation rates predicted with Flow Simulation with comparison to the theoretical values.

Parameter	Theory (Ref.6), W	Flow Simulation predictions	
		Value, W	Prediction error, %
Q2 r	-383.77	-388.30	1.2%
J2 r	1728.35	1744.47	0.9%
Q1 r	4003.68	3931.87	-1.8%
J1 r	8552.98	8596.04	0.5%

It is seen that the prediction errors are quite small. To validate the Flow Simulation capabilities on the third problem, which couples convection and radiation, let us add the theoretical net radiation rates, Q_{1r} and Q_{2r} scaled to the reduced computational domain, i.e., divided by 4, to the Q_1 and Q_2 values specified in the first problem. Let us specify $Q_1 = 1108.15 \text{ W}$ and $Q_2 = -203.18 \text{ W}$, so theoretically we must obtain the same fluid temperature profile as in the first considered problem.

The fluid temperature profile predicted at 0.75 m from the tube model inlet at the result resolution level 6 is shown in Fig. 11.4. together with the theoretical curve. It is seen that once again this prediction virtually coincides with the theoretical curve.

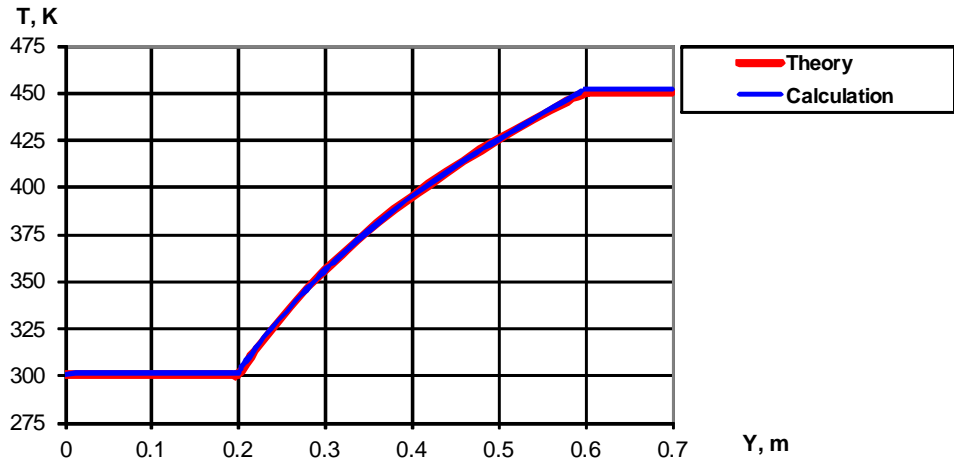


Fig. 11.4. Fluid temperature profiles across the tube in the case coupling convection and radiation, predicted with Flow Simulation and compared to the theoretical curve.

12 Pin-fin Heat Sink Cooling by Natural Convection

Heat sinks play an important role in electronics cooling. Following the experimental work presented in Ref. 14 and numerical study presented in Ref. 16, let us consider heat transfer from an electrically heated thermofoil which is mounted flush on a plexiglass substrate, coated by an aluminum pin-fin heat sink with a 9×9 pin fin array, and placed in a closed plexiglass box. In order to create more uniform ambient conditions for this box, it is placed into another, bigger, plexiglass box and attached to the heat-insulated thick wall, see Figs. 12.1, 12.2. Following Ref. 14, let us consider the vertical position of these boxes, as it is shown in Fig. 12.1. (c) (here, the gravity acts along the Y axis).

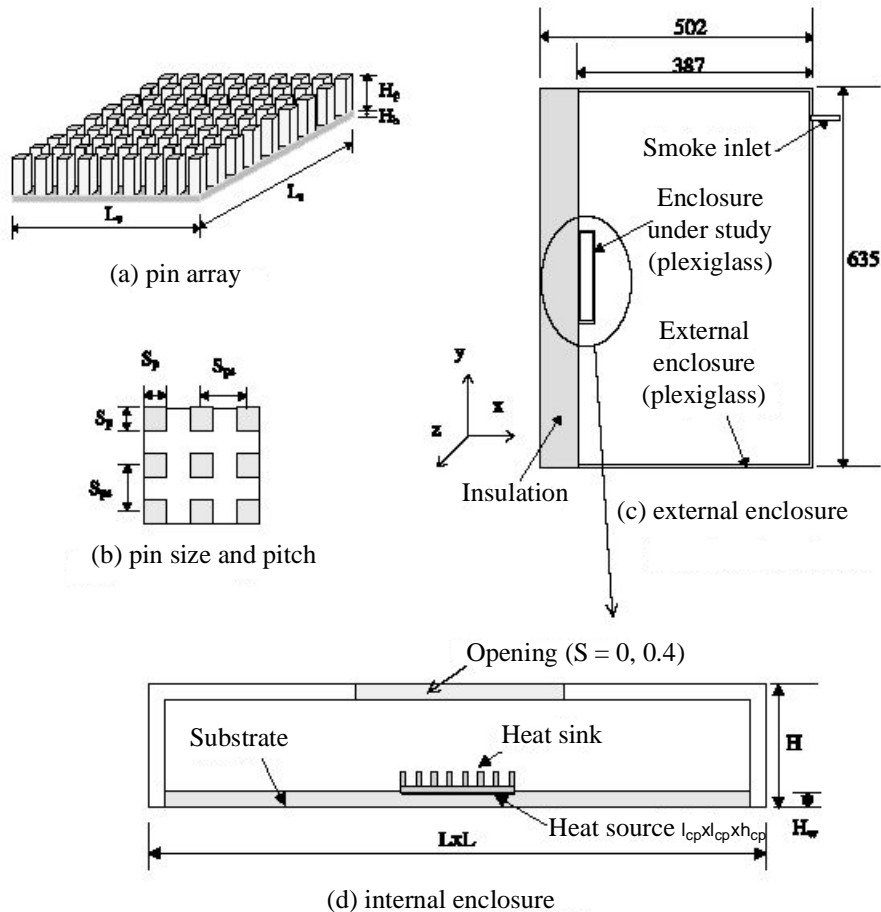


Fig. 12.1. The pin-fin heat sink nestled within two plexiglass boxes: $l_{cp}=L_s=25.4$ mm, $h_{cp}=0.861$ mm, $H_p=5.5$ mm, $H_b=1.75$ mm, $S_p=1.5$ mm, $S_{ps}=L_s/8$, $L=127$ mm, $H=41.3$ mm, $H_w=6.35$ mm (from Ref.19).

The corresponding model used in the calculations is shown in Fig. 12.2.. In this model's coordinate system the gravitational acceleration vector is directed along the X axis. The computational domain envelopes the outer surface of the external box, and the Z=0 symmetry plane is used to reduce the required computer resources.

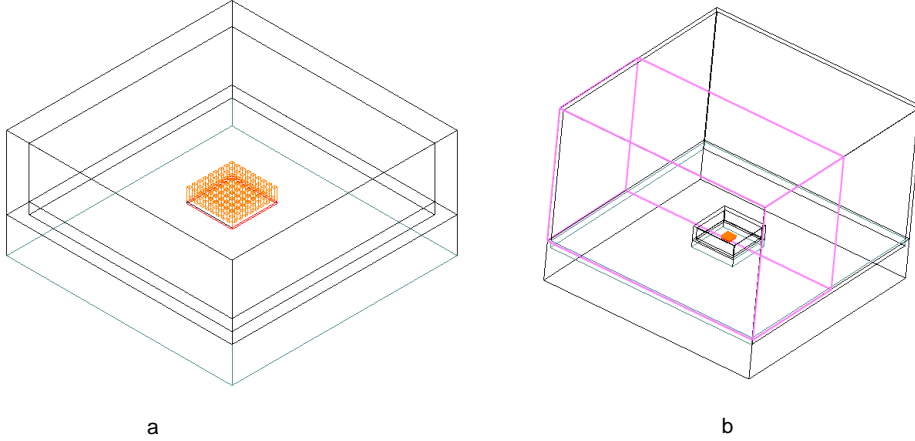


Fig. 12.2. A model created for calculating the heat transfer from the pin-fin heat sink through the two nested boxes into the environment: (a) the internal (smaller) box with the heat sink; (b) the whole model.

According to Ref. 14, both the heat sink and the substrate are coated with a special black paint to provide a surface emissivity of 0.95 (the other plexiglass surfaces are also opaque, diffuse and gray, but have an emissivity of 0.83).

The maximum steady-state temperature T_{max} of the thermofoil releasing the heat of known power Q was measured. The constant ambient temperature T_a was measured at the upper corner of the external box. As a result, the value of

$$R_{ja} = (T_{max} - T_a)/Q \quad (12.1)$$

was determined at various Q (in the 0.1...1 W range).

The ambient temperature is not presented in Ref. 14, so, proceeding from the suggestion that the external box in the experiment was placed in a room, we have varied the ambient temperature in the relevant range of 15...22°C. Since R_{ja} is governed by the temperature difference $T_{max} - T_a$, (i.e. presents the two boxes' thermal resistance), the ambient temperature range only effects the resistance calculations by 0.6°C/W at $Q = 1$ W, (i.e. by 1.4% of the experimentally determined R_{ja} value that is 43°C/W). As for the boundary conditions on the external box's outer surface, we have specified a heat transfer coefficient of 5.6 W/m² K estimated from Ref. 15 for the relevant wind-free conditions and an ambient temperature lying in the range of 15...22°C (additional calculations have shown that the variation of the constant ambient temperature on this boundary yield nearly identical results). As a result, at $Q = 1$ W (the results obtained at the other Q values are shown in Ref. 16) and $T_a = 20^\circ\text{C}$ we have obtained $R_{ja} = 41^\circ\text{C/W}$, i.e. only 5% lower than the experimental value.

The flow streamlines visualized in Ref. 14 using smoke and obtained in the calculations are shown in Fig. 12.3.

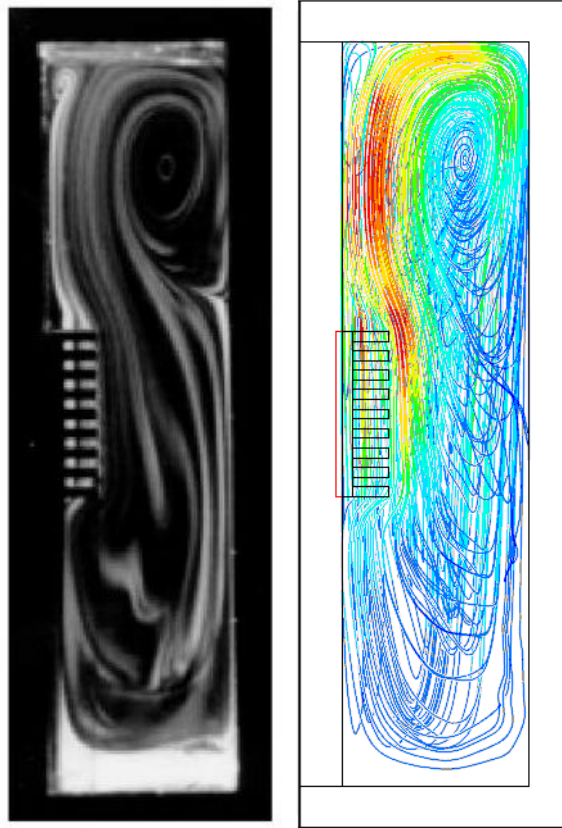


Fig. 12.3. Flow streamlines visualized by smoke in the Ref.19 experiments (left) and obtained in the calculations (colored in accordance with the flow velocity values) (right).

13 Plate Fin Heat Sink Cooling by Forced Convection

This validation example demonstrates Flow Simulation capabilities to simulate forced air cooling of plate fin heat sink placed in a wind tunnel. The calculations are based on the experimental results from Ref. 17, where several flow regimes were considered.

Heat sink geometry with its main dimensions is shown in Fig. 13.1. The dimension values were set as follows: fin height (H) of 10 mm, thickness of 1.5 mm and fin-to-fin distance (δ) of 5 mm while the heat sink width (B) and length were 52.8 mm and the base thickness was 3 mm. The wind tunnel width (CB), height (CH) and length were 160 mm, 15 mm and 200 mm respectively.

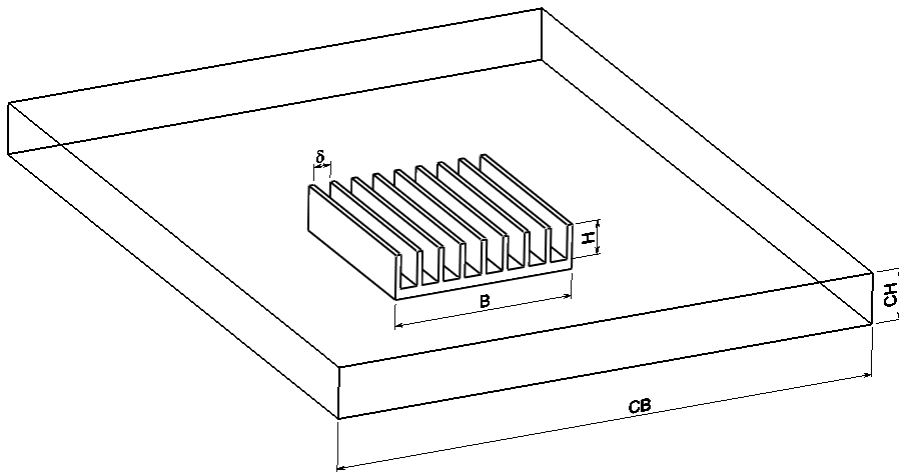


Fig. 13.1 Geometry model of the heat sink.

The model of heat sink is made of solid aluminum (thermal conductivity 200 W/(m·K)). It is heated by MINCO Thermofoil™ electrical heater with a heat load of 10 W. The bottom of the heated foil is insulated with a 25 mm Polystyrene brick (thermal conductivity 0.033 W/(m·K)). The heat sink is placed in a rectangular wind tunnel duct with the walls made of Plexiglass (thermal conductivity 0.2 W/(m·K)). It is mounted in such a way that the fin base is flush with the duct wall as shown in Fig. 13.2.

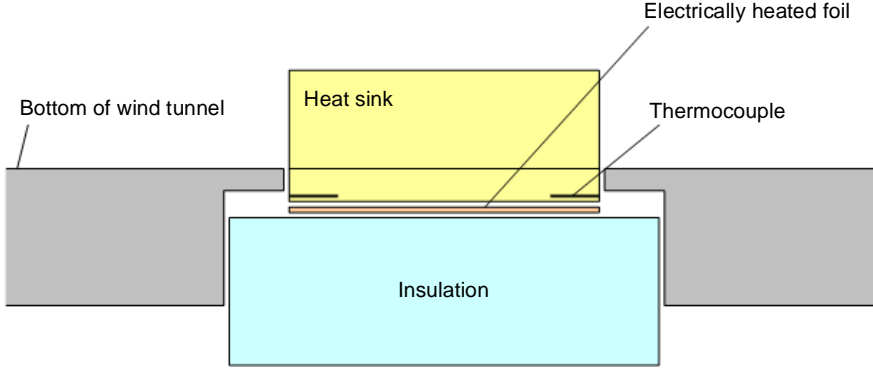


Fig. 13.2 Vertical cut view of heat sink.

The performance of the heat sink is estimated by a thermal resistance defined as

$$R_{th} = \frac{T_{hs} - T_0}{q},$$

where T_{hs} is the temperature of the heat sink base, T_0 is the temperature at the wind tunnel inlet and q is the total power input of the heat source (10 W). In Ref. 17, the T_{hs} value was measured by averaging the reading of four thermocouples (two of them can be seen in Fig. 13.2) placed symmetrically at the corners of the heat sink base.

Table 13.1 shows air inlet flow conditions specified for the calculations, inlet temperature is constant and equal 20°C. To perform the calculations, five cases are considered, each with a different inlet velocity u_{in} that was determined as follows:

$$u_{in} = \dot{V} / A,$$

where $A = 24 \text{ cm}^2$ is wind tunnel cross sectional area; \dot{V} is volumetric air flow rate at standard conditions defined as

$$w = \frac{\dot{V}}{A - A_{front}}, \quad Re_{dh} = \frac{\rho \cdot w \cdot d_h}{\mu}$$

where w is average air velocity; $A_{front} = 1.4 \text{ cm}^2$ is front area of the fins; Re_{dh} is the Reynolds duct number; d_h is hydraulic diameter of the wind tunnel; μ is dynamic viscosity of air; ρ is density of air.

Table 13.1 Inlet boundary conditions.

Case	u_{in} , m/s	Re_{dh}
1	0.903	1740
2	1.287	2480
3	1.583	3050
4	1.899	3660
5	3.633	7000

The outlet static pressure is set to 1 atm.

The heat exchange between the outer duct surfaces and the ambient medium with the temperature of 20°C is defined by a Newton's law of cooling with the heat-transfer coefficient of 3 W/m²·K.

Since the geometry model has a symmetry plane, only a half of the model is used to generate the computational mesh.

The automatically generated mesh with RRL=3 contained approximately 26 000 cells for cases 1-4 and with RRL=5 contained approximately 109 000 cells for case 5. Fig. 13.3 shows the mesh generated in the fluid region in one of the heat sink cross-sections. One can see that there only about 3-4 cells generated between two adjacent fins.

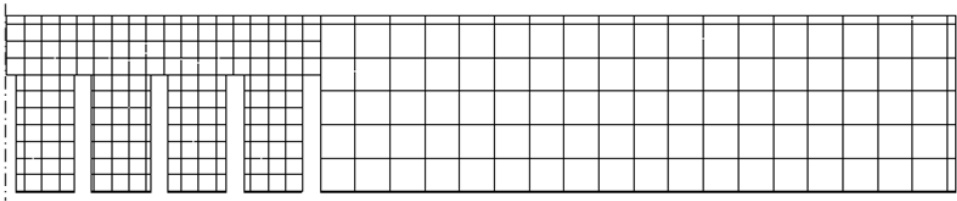


Fig. 13.3 The computational mesh (cases 1-4).

The values of thermal resistances predicted by Flow Simulation and the corresponding values measured experimentally are shown in Fig. 13.4. According to this plot, the difference between the calculations and the experimental measurements is less than 10%.

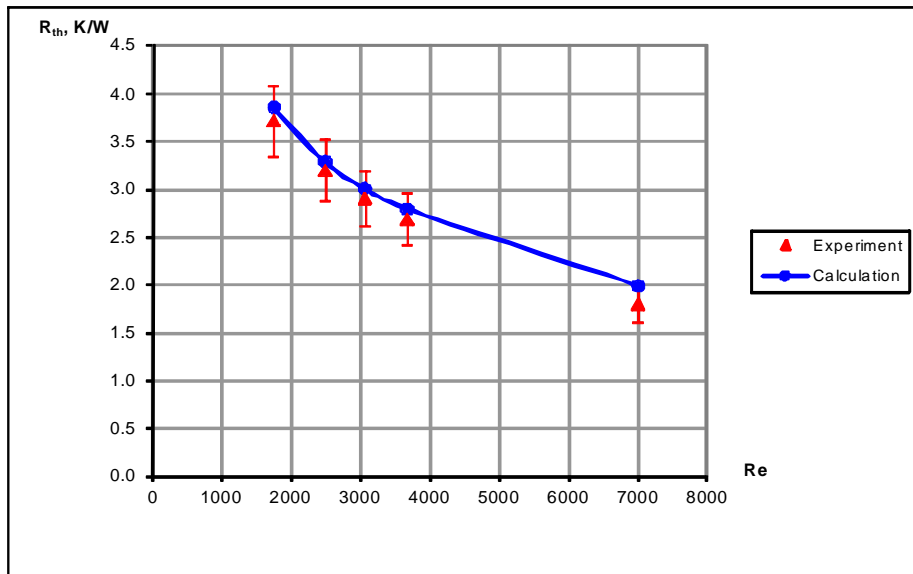


Fig. 13.4 Thermal resistance of the Heat Sink versus Reynold number in comparison with the experimental data (Ref. 17).

This indicates that the sufficient accuracy of the results is maintained even on a coarse mesh generated inside the narrow channels.

14 Unsteady Heat Conduction in a Solid

To validate heat conduction in solids (i.e., a conjugate heat transfer), let us consider unsteady heat conduction in a solid. To compare the Flow Simulation predictions with the analytical solution (Ref. 6), we will solve a one-dimensional problem.

A warm solid rod having the specified initial temperature and the heat-insulated side surface suddenly becomes and stays cold (at a constant temperature of $T_w=300$ K) at both ends (see Fig. 14.1.). The rod inner temperature evolution is studied. The constant initial temperature distribution along the rod is considered: $T_{\text{initial}}(x)=350$ K.

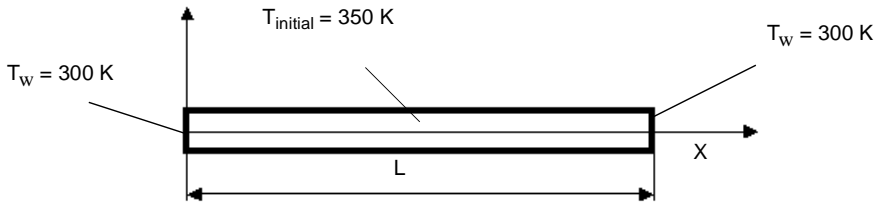


Fig. 14.1. A warm solid rod cooling down from an initial temperature to the temperature at the ends of the rod.

The problem is described by the following differential equation:

$$\frac{\partial^2 T}{\partial x^2} = \frac{\rho C}{k} \frac{\partial T}{\partial \tau} ,$$

where ρ , C , and k are the solid material density, specific heat, and thermal conductivity, respectively, and τ is the time, with the following boundary condition: $T=T_0$ at $x=0$ and at $x=L$.

In the general case, i.e., at an arbitrary initial condition, the problem has the following solution:

$$T = T_0 + \sum_{n=1}^{\infty} C_n e^{-(n\pi/L)^2 k \tau / (\rho C)} \sin \frac{n\pi x}{L} ,$$

where coefficients C_n are determined from the initial conditions (see Ref.6).

With the uniform initial temperature profile, according to the initial and boundary conditions, the problem has the following solution:

$$T = 300 + 50 \frac{4}{\pi} \sum_{n=1}^{\infty} \frac{1}{n} e^{-[n\pi/L]^2 k \tau / (\rho C)} \sin\left(\frac{n\pi x}{L}\right) \quad (\text{K}).$$

To perform the time-dependent analysis with Flow Simulation, a SolidWorks model representing a solid parallelepiped with dimensions 1x0.2x0.1 m has been created (see Fig. 14.2.).

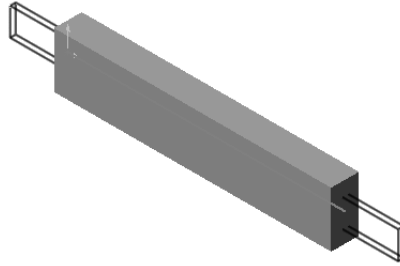


Fig. 14.2. The SolidWorks model used for calculating heat conduction in a solid rod with Flow Simulation (the computational domain envelopes the rod).

The evolution of maximum rod temperature, predicted with Flow Simulation and compared with theory, is presented in Fig. 14.3.. The Flow Simulation prediction has been performed at result resolution level 5. One can see that it coincide with the theoretical curve.

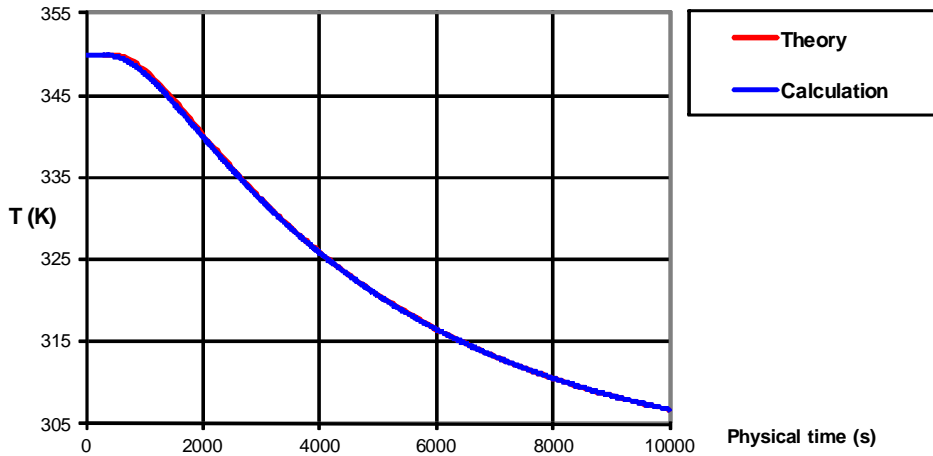


Fig. 14.3. Evolution of the maximum rod temperature, predicted with Flow Simulation and compared to theory.

The temperature profiles along the rod at different time moments, predicted by Flow Simulation, are compared to theory and presented in Fig. 14.4.. One can see that the Flow Simulation predictions are very close to the theoretical profiles. The maximum prediction error not exceeding 2K occurs at the ends of the rod and is likely caused by calculation error in the theoretical profile due to the truncation of Fourier series.

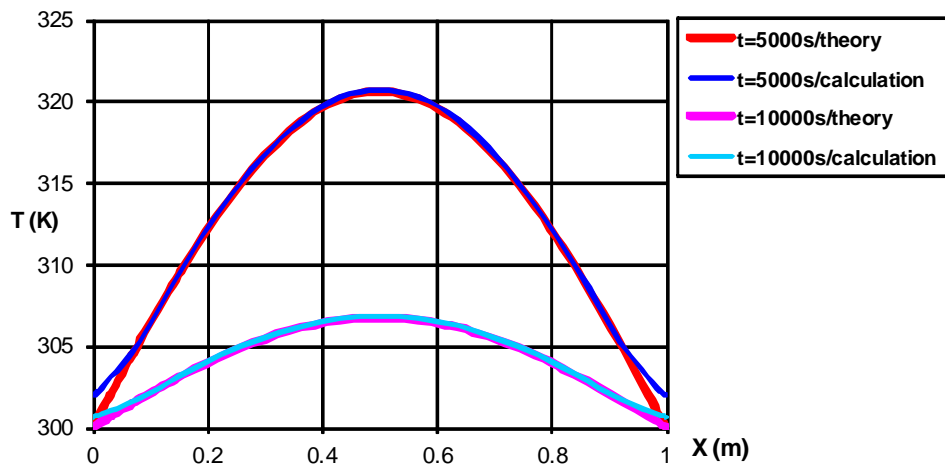


Fig. 14.4. Evolution of the temperature distribution along the rod, predicted with Flow Simulation and compared to theory.

15 Tube with Hot Laminar Flow and Outer Heat Transfer

Let us now consider an incompressible laminar flow of hot fluid through an externally cooled circular tube (Fig. 15.1.). The fluid flow has fully developed velocity and temperature profiles at the tube inlet, whereas the heat transfer conditions specified at the tube outer surface surrounded by a cooling medium sustain the self-consistent fluid temperature profile throughout the tube.

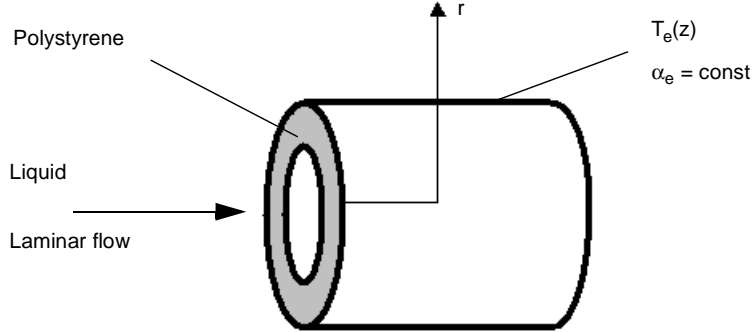


Fig. 15.1. Laminar flow in a tube cooled externally.

In accordance with Ref. 6, a laminar tube flow with a fully developed velocity profile has a self-consistent fully developed temperature profile if the following two conditions are satisfied: the fluid's properties are temperature-independent and the heat flux from the tube inner surface to the fluid (or vice versa) is constant along the tube. These conditions provide the following fully developed tube flow temperature profile:

$$T(r, z) = T(r=0, z=z_{inlet}) - \frac{q_w R_i}{k} \left[\left(\frac{r}{R_i} \right)^2 - \frac{1}{4} \left(\frac{r}{R_i} \right)^4 \right] + \frac{4q_w \cdot (z - z_{inlet})}{\rho C_p u_{max} R_i},$$

where

T is the fluid temperature,

r is a radial coordinate ($r = 0$ corresponds to the tube axis, $r = R_i$ corresponds to the tube inner surface, i.e., R_i is the tube inner radius),

z is an axial coordinate ($z = z_{inlet}$ corresponds to the tube inlet),

q_w is a constant heat flux from the fluid to the tube inner surface,

k is the fluid thermal conductivity,

ρ is the fluid density,

C_p is the fluid specific heat under constant pressure,

u_{max} is the maximum fluid velocity of the fully developed velocity profile

$$u(r) = u_{max} \left(1 - \left(\frac{r}{R_i} \right)^2 \right).$$

Since the tube under consideration has no heat sinks and is cooled by surrounding fluid medium, let us assume that the fluid medium surrounding the tube has certain fixed temperature T_e , and the heat transfer between this medium and the tube outer surface is determined by a specified constant heat transfer coefficient α_e .

By assuming a constant thermal conductivity of the tube material, k_s , specifying an arbitrary α_e , and omitting intermediate expressions, we can obtain the following expression for T_e :

$$T_e(z) = T(r=0, z=z_{inlet}) - q_w R_i \left(\frac{3}{4k} + \frac{1}{\alpha_e R_o} - \frac{1}{k_s} \ln \frac{R_i}{R_o} \right) + \frac{4q_w \cdot (z - z_{inlet})}{\rho C_p u_{max} R_i},$$

where R_o is the tube outer radius.

In the validation example under consideration (Fig. 15.2.) the following tube and fluid characteristics have been specified: $R_i = 0.05$ m, $R_o = 0.07$ m, $z - z_{inlet} = 0.1$ m, the tube material is polystyrene with thermal conductivity $k_s = 0.082$ W/(m·K), $u_{max} = 0.002$ m/s, $T(r=0, z=z_i) = 363$ K, $q_w = 147.56$ W/m², $k = 0.3$ W/(m·K), $C_p = 1000$ J/(kg·K), fluid dynamic viscosity $\mu = 0.001$ Pa·s, $\rho = 1000$ kg/m³ (these fluid properties provide a laminar flow condition since the tube flow Reynolds number based on the tube diameter is equal to $Re_d = 100$). The $T(r, z_{inlet})$ and $u(r)$ profiles at the tube inlet, the $T_e(z)$ distribution along the tube, $\alpha_e = 5$ W/(m²·K), and tube outlet static pressure $P_{out} = 1$ atm have been specified as the boundary conditions.

The inlet flow velocity and temperature profiles have been specified as the initial conditions along the tube.

To reduce the computational domain, the calculations have been performed with the Y=0 and X=0 flow symmetry planes. The calculations have been performed at result resolution level 7.

The fluid and solid temperature profiles predicted at $z = 0$ are shown in Fig. 15.3. together with the theoretical curve. It is seen that the prediction practically coincides with the theoretical curve (the prediction error does not exceed 0.4%).

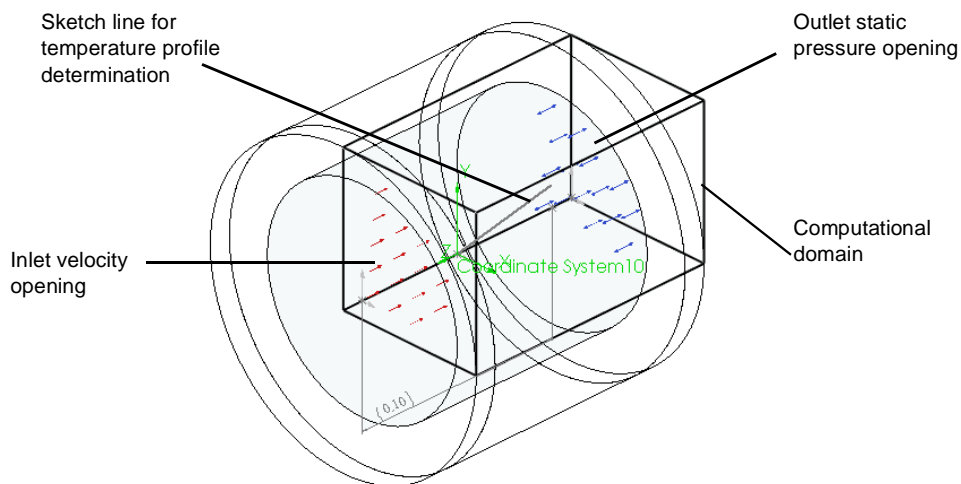


Fig. 15.2. The model used for calculating the 3D flow and the conjugate heat transfer in the tube with Flow Simulation.

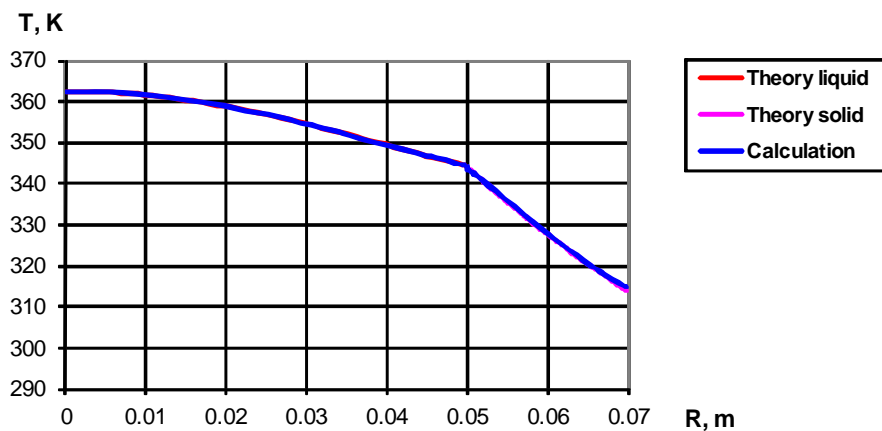


Fig. 15.3. Fluid and solid temperature profiles across the tube, predicted with Flow Simulation and compared with the theoretical curve.

16 Flow over a Heated Cylinder

Let us now return to the earlier validation example of incompressible flow over a cylinder and modify it by specifying a heat generation source inside the cylinder (see Fig. 16.1.). The cylinder is placed in an incoming air stream and will acquire certain temperature depending on the heat source power and the air stream velocity and temperature.

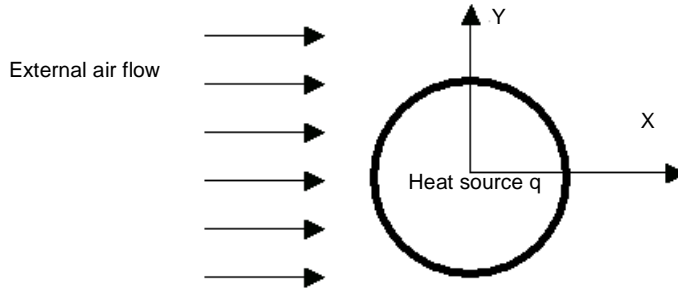


Fig. 16.1. 2D flow over a heated cylinder.

Based on experimental data for the average coefficient of heat transfer from a heated circular cylinder to air flowing over it (see Ref. 6), the corresponding Nusselt number can be determined from the following formula:

$$Nu_D = C \cdot (Re_D)^n \cdot Pr^{1/3} ,$$

where constants C and n are taken from the following table:

Re_D	C	n
0.4 - 4	0.989	0.330
4 - 40	0.911	0.385
40 - 4000	0.683	0.466
4000 - 40000	0.193	0.618
40000 - 400000	0.0266	0.805

Here, the Nusselt number, $Nu_D = (h \cdot D)/k$ (where h is the heat transfer coefficient averaged over the cylinder, and k is fluid thermal conductivity), the Reynolds number, $Re_D = (U \cdot D)/\mu$ (where U is the incoming stream velocity, and μ is fluid dynamic viscosity), and the Prandtl number, $Pr = \mu \cdot C_p/k$ (where μ is fluid dynamic viscosity, C_p is fluid specific heat at constant pressure, and k is fluid thermal conductivity) are based on the cylinder diameter D and on the fluid properties taken at the near-wall flow layer. According to Ref. 6, $Pr = 0.72$ for the entire range of Re_D .

To validate the Flow Simulation predictions, the air properties have been specified to provide $Pr = 0.72$; $k = 0.0251375 \text{ W/(m}\cdot\text{K)}$, $\mu = 1.8 \cdot 10^{-5} \text{ Pa}\cdot\text{s}$, specific heat at constant pressure $C_p = 1005.5 \text{ J/(kg}\cdot\text{K)}$. Then, the incoming stream velocity, U , has been specified to obtain $Re_D = 1, 10, 100, 10^3, 10^4, 5 \cdot 10^4, 10^5, 2 \cdot 10^5$, and $3 \cdot 10^5$ for a cylinder diameter of $D = 0.1 \text{ m}$ (see Table 16.5).

This validation approach consists of specifying the heat generation source inside the cylinder with a power determined from the desired steady-state cylinder temperature and the average heat transfer coefficient, $h = (Nu_D \cdot k)/D$. Nu_D is determined from the specified Re_D using the empirical formula presented above. The final cylinder surface temperature, that is also required for specifying the heat source power Q (see Table 16.5) is assumed to be 10°C higher than the incoming air temperature. The initial cylinder temperature and the incoming air temperature are equal to 293.15 K . The cylinder material is aluminum. Here, the heat conduction in the solid is calculated simultaneously with the flow calculation, i.e., the conjugate heat transfer problem is solved.

As a result of the calculation, the cylinder surface has acquired a steady-state temperature differing from the theoretical one corresponding to the heat generation source specified inside the cylinder. Multiplying the theoretical value of the Nusselt number by the ratio of the obtained temperature difference (between the incoming air temperature and the cylinder surface temperature) to the specified temperature difference, we have determined the predicted Nusselt number versus the specified Reynolds number. The values obtained by solving the steady-state and time dependent problems at result resolution level 5 are presented in Fig. 16.2. together with the experimental data taken from Ref. 6.

Table 16.5 The Flow Simulation specifications of U and Q for the problem under consideration.

Re_D	$U, \text{ m/s}$	$Q, \text{ W}$
1	1.5×10^{-4}	0.007
10	1.5×10^{-3}	0.016
10^2	0.015	0.041
10^3	0.15	0.121
10^4	1.5	0.405
10^5	15	1.994

From Fig. 16.2., it is seen that the predictions made with Flow Simulation, both in the time-dependent approach and in the steady-state one, are excellent within the whole Re_D range under consideration.

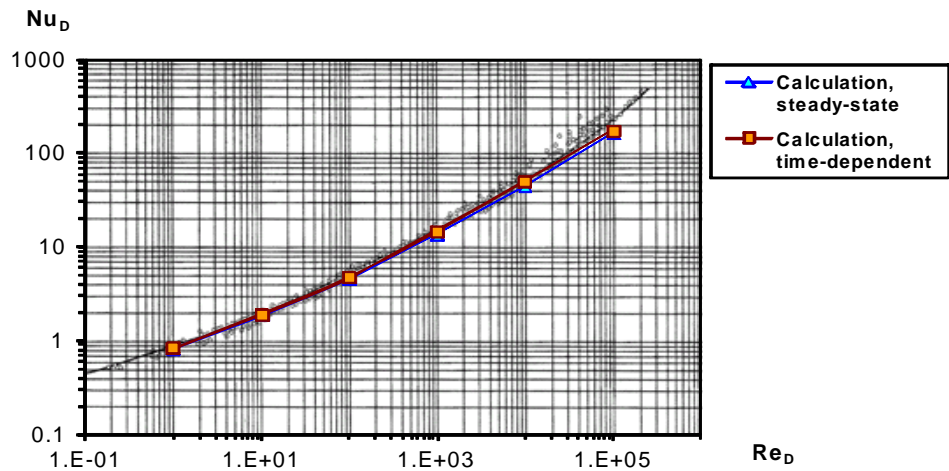


Fig. 16.2. Nusselt number for air flow over a heated cylinder: Flow Simulation predictions and the experimental data taken from Ref. 6.

17 Natural Convection in a Square Cavity

Here we will consider a 2D square cavity with a steady-state natural convection, for which a highly-accurate numerical solution has been proposed in Ref.10 and used as a benchmark for about 40 computer codes in Ref.11, besides it well agrees with the semi-empirical formula proposed in Ref.12 for rectangular cavities. This cavity's configuration and imposed boundary conditions, as well as the used coordinate system, are presented in Fig. 17.1.. Here, the left and right vertical walls are held at the constant temperatures of $T_1 = 305 \text{ K}$ and $T_2 = 295 \text{ K}$, accordingly, whereas the upper and bottom walls are adiabatic. The cavity is filled with air.

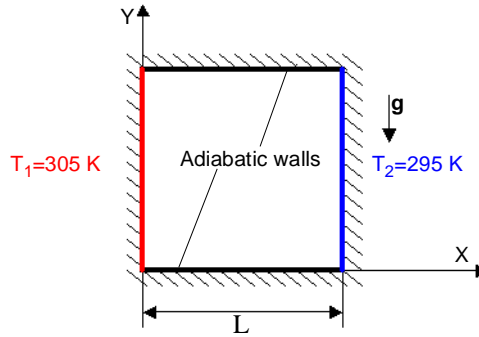


Fig. 17.1. An enclosed 2D square cavity with natural convection.

The square cavity's side dimension, L , is varied within the range of $0.0111...0.111 \text{ m}$ in order to vary the cavity's Rayleigh number within the range of $10^3...10^6$. Rayleigh number describes the characteristics of the natural convection inside the cavity and is defined as follows:

$$Ra = \frac{\beta g \rho^2 C_p L^3 \Delta T}{k \mu} ,$$

where $\beta = \frac{1}{T}$ is the volume expansion coefficient of air,

g is the gravitational acceleration,

C_p is the air's specific heat at constant pressure,

$\Delta T = T_1 - T_2 = 10 \text{ K}$ is the temperature difference between the walls,

k is the thermal conductivity of air,

μ is the dynamic viscosity of air.

The cavity's model is shown in Fig. 17.2..

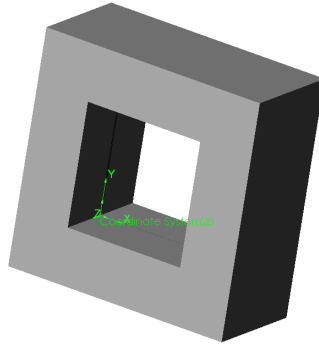


Fig. 17.2. The model created for calculating the 2D natural convection flow in the 2D square cavity using Flow Simulation.

Due to gravity and different temperatures of the cavity's vertical walls, a steady-state natural convection flow (vortex) with a vertical temperature stratification forms inside the cavity. The $Ra = 10^5$ flow's prediction performed with Flow Simulation is shown in Fig. 17.3..

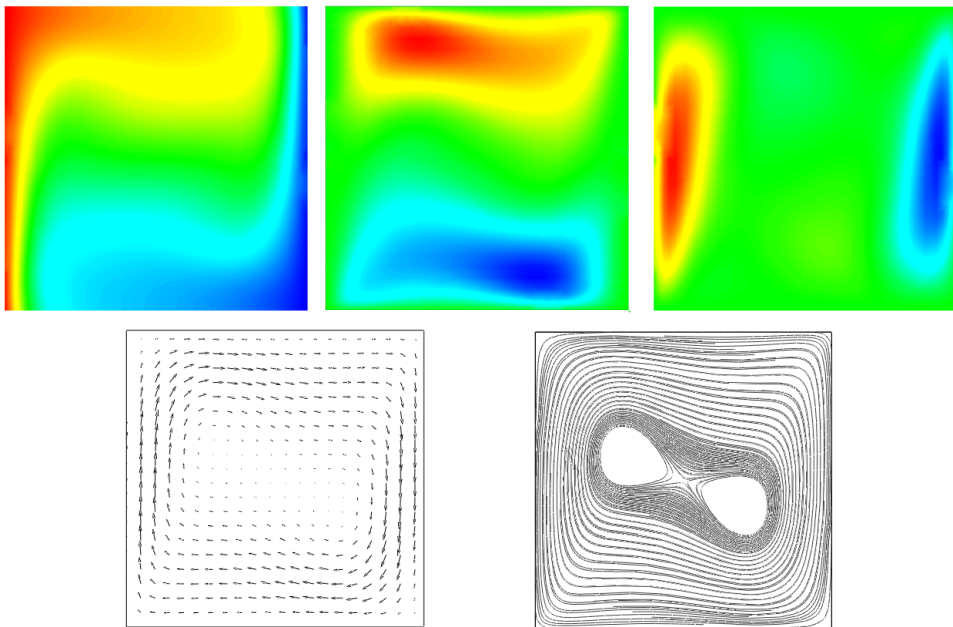


Fig. 17.3. The temperature, X-velocity, Y-velocity, the velocity vectors, and the streamlines, predicted by Flow Simulation in the square cavity at $Ra = 10^5$.

A quantitative comparison of the Flow Simulation predictions performed at result resolution level 8 with References.10, 11 (computational benchmark) and 12 (semi-empirical formula) for different Ra values is presented in Figs.17.4 - 17.6. The Nusselt number averaged over the cavity's hot vertical wall (evidently, the same value must be obtained over the cavity's cold vertical wall) $Nu_{av} = q_{w_{av}} \cdot L / (\Delta T \cdot k)$, where $q_{w_{av}}$ is the heat flux from the wall to the fluid, averaged over the wall, is considered in Fig. 17.4..

Here, the dash line presents the Ref.12 semi-empirical formula

$$Nu_{av} = 0.28 \cdot Ra^{1/4} (L/D)^{-1/4},$$

where D is the distance between the vertical walls and L is the cavity height ($D=L$ in the case under consideration). One can see that the Flow Simulation predictions practically coincide with the benchmark at $Ra \leq 10^5$ and are close to the semi-empirical data.

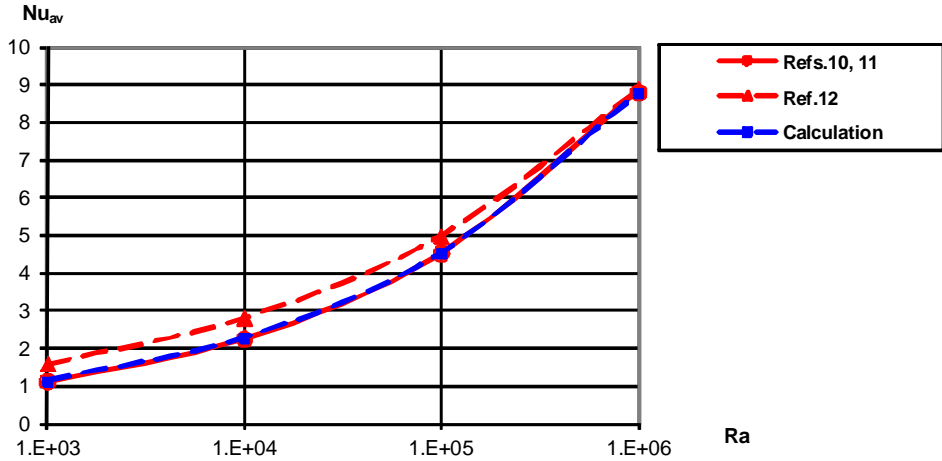


Fig. 17.4. The average sidewall Nusselt number vs. the Rayleigh number.

The dimensionless velocities of the natural convection flow in the X and Y directions,

$$\bar{U} = \frac{U \cdot L \cdot C_p \cdot \rho}{k} \quad \text{and} \quad \bar{V} = \frac{V \cdot L \cdot C_p \cdot \rho}{k} \quad (\text{which are maximum along the cavity's}$$

mid-planes, i.e., \bar{U}_{\max} along the vertical mid-plane and \bar{V}_{\max} along the horizontal

mid-plane) are considered in Fig. 17.5.. The dimensionless coordinates, $\bar{x} = \frac{x}{L}$ and

$\bar{y} = \frac{y}{L}$, of these maximums' locations (i.e., \bar{y} for \bar{U}_{\max} and \bar{x} for \bar{V}_{\max}) are

presented in Fig. 17.6.. One can see that the Flow Simulation predictions of the natural convection flow's local parameters are fairly close to the benchmark data at $Ra \leq 10^5$.

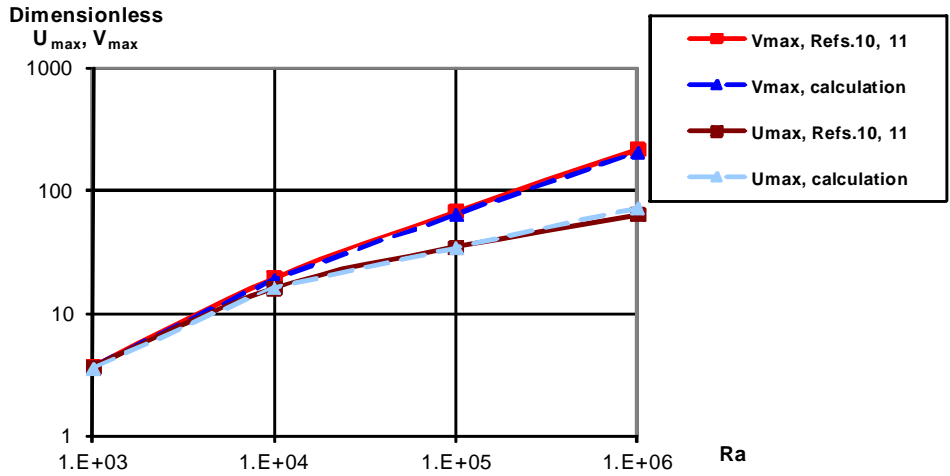


Fig. 17.5. Dimensionless maximum velocities vs. Rayleigh number.

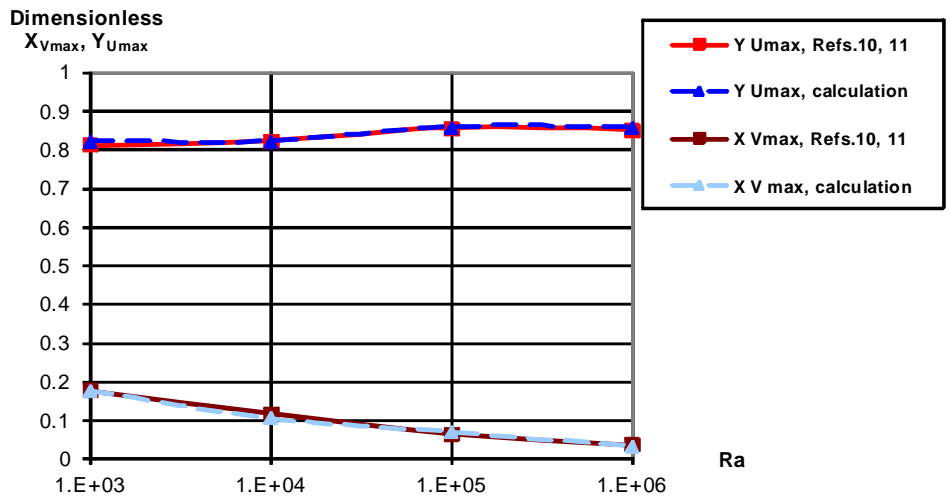


Fig. 17.6. Dimensionless coordinates of the maximum velocities' locations.

18 Particles Trajectories in Uniform Flows

Let us now consider the Flow Simulation capability to predict particles trajectories in a gas flow (i.e. two-phase flow of fluid + liquid droplets or solid particles).

In accordance with the particles motion model accepted in Flow Simulation, particle trajectories are calculated after completing a fluid flow calculation (which can be either steady or time-dependent). That is, the particles mass and volume flow rates are assumed substantially lower than those of the fluid stream, so that the influence of particles' motions and temperatures on the fluid flow parameters is negligible, and motion of the particles obeys the following equation:

$$m \frac{dV_p}{dt} = - \frac{\rho_f (V_f - V_p) \cdot |V_f - V_p|}{2} C_d A + F_g ,$$

where m is the particle mass, t is time, V_p and V_f are the particle and fluid velocities (vectors), accordingly, ρ_f is the fluid density, C_d is the particle drag coefficient, A is the particle frontal surface area, and F_g is the gravitational force.

Particles are treated as non-rotating spheres of constant mass and specified (solid or liquid) material, whose drag coefficient is determined from Henderson's semi-empirical formula (Ref. 18). At very low velocity of particles with respect to carrier fluid (i.e., at the relative velocity's Mach number $M \rightarrow 0$) this formula becomes

$$C_d = \frac{24}{Re} + \frac{4.12}{1 + 0.03 \cdot Re + 0.48 \sqrt{Re}} + 0.38$$

where Reynolds number is defined as

$$Re = \frac{\rho_f |V_f - V_p| d}{\mu} ,$$

d is the diameter of particles, and μ is the fluid dynamic viscosity.

To validate Flow Simulation, let us consider three cases of injecting a particle perpendicularly into an incoming uniform flow, Fig. 18.1.. Since both the fluid flow and the particle motion in these cases are 2D (planar), we will solve a 2D (i.e. in the XY-plane) flow problem.

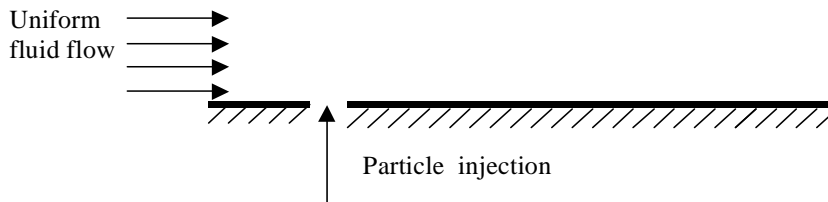


Fig. 18.1. Injection of a particle into a uniform fluid flow.

Due to the same reason as in the previous validation examples with flow over flat plates, we will solve this validation as an internal problem. The corresponding SolidWorks model is shown in Fig. 18.2.. Both of the walls are ideal, the channel has length of 0.233 m and height of 0.12 m, all the walls have thickness of 0.01 m. We specify the uniform fluid velocity V_{inlet} , the fluid temperature of 293.2 K, and the default values of turbulent flow parameters with the laminar boundary layer at the channel inlet, and the static pressure of 1 atm at the channel outlet. All the fluid flow calculations are performed at a result resolution level of 5.

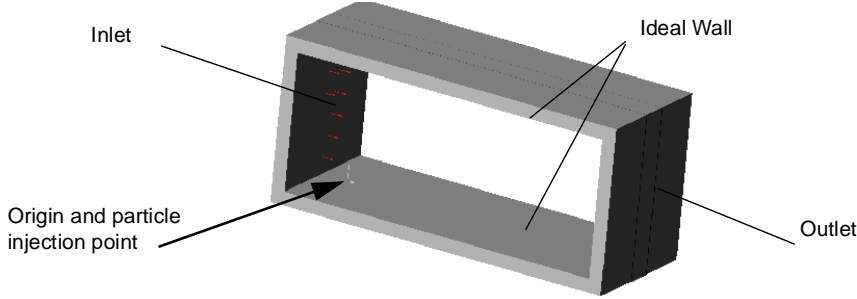


Fig. 18.2. The model.

To validate calculations of particles trajectories by comparing them with available analytical solutions of the particle motion equation, we consider the following three cases:

- a) the low maximum Reynolds number of $Re_{max} = 0.1$ (air flow with $V_{inlet} = 0.002$ m/s, gold particles of $d = 0.5$ mm, injected at the velocity of 0.002 m/s perpendicularly to the wall),
- b) the high maximum Reynolds number of $Re_{max} = 10^5$ (water flow with $V_{inlet} = 10$ m/s, iron particles of $d = 1$ cm, injected at the velocities of 1, 2, 3 m/s perpendicularly to the wall),
- c) a particle trajectory in the Y-directed gravitational field (gravitational acceleration $g_y = -9.8$ m/s², air flow with $V_{inlet} = 0.6$ m/s, an iron particle of $d = 1$ cm, injected at the 1.34 m/s velocity at the angle of 63.44° with the wall).

In the first case, due to small Re values, the particle drag coefficient is close to $C_d = 24/Re$ (i.e., obeys the Stokes law). Then, neglecting gravity, we obtain the following analytical solution for the particle trajectory:

$$X(t) = X|_{t=0} + V_{fx} \cdot t + \frac{d^2 \rho_p}{18\mu} (V_{px}|_{t=0} - V_{fx}) \cdot \exp\left(-\frac{18\mu}{d^2 \rho_p} t\right) ,$$

$$Y(t) = Y|_{t=0} + V_{fy} \cdot t + \frac{d^2 \rho_p}{18\mu} (V_{py}|_{t=0} - V_{fy}) \cdot \exp\left(-\frac{18\mu}{d^2 \rho_p} t\right) ,$$

where V_{fx} , V_{px} , V_{fy} , V_{py} are the X- and Y-components of the fluid and particle velocities, accordingly, ρ_p is the particle material density. The Flow Simulation calculation and the analytical solution are shown in Fig. 18.3.. It is seen that they are very close to one another. Special calculations have shown that the difference is due to the C_D assumptions only.

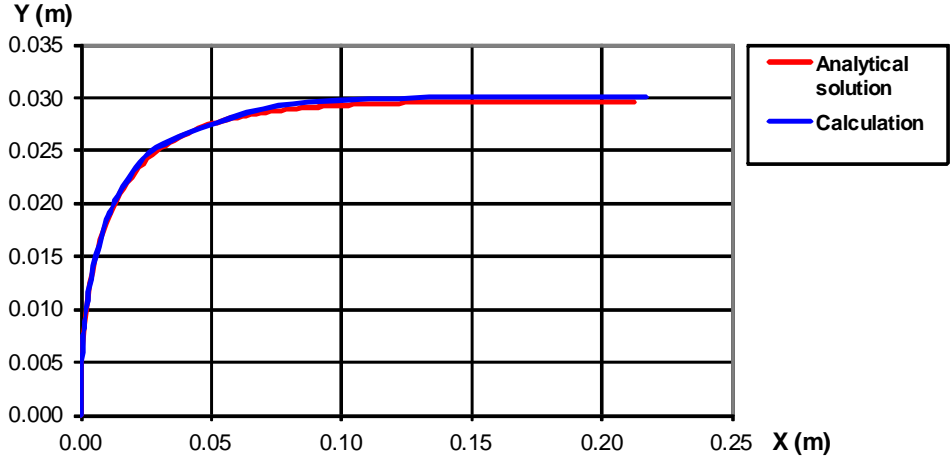


Fig. 18.3. Particle trajectories in a uniform fluid flow at $Re_{max} = 0.1$, predicted by Flow Simulation and obtained from the analytical solution.

In the second case, due to high Re values, the particle drag coefficient is close to $C_d=0.38$. Then, neglecting the gravity, we obtain the following analytical solution for the particle trajectory:

$$Y(t) = Y|_{t=0} + V_{fy} \cdot t + \frac{\rho_p d}{0.285 \rho} (V_{py}|_{t=0} - V_{fy}) \cdot \ln\left(1 + \frac{0.285 \rho}{\rho_p d} t\right) ,$$

$$X(t) = X|_{t=0} + V_{fx} \cdot t + \frac{\rho_p d}{0.285 \rho} (V_{px}|_{t=0} - V_{fx}) \cdot \ln\left(1 + \frac{0.285 \rho}{\rho_p d} t\right) .$$

The Flow Simulation calculations and the analytical solutions for three particle injection velocities, $V_{py}(t=0) = 1, 2, 3 \text{ m/s}$, are shown in Fig. 18.4.. It is seen that the Flow Simulation calculations coincide with the analytical solutions. Special calculations have shown that the difference is due to the C_D assumptions only.

In the third case, the particle trajectory is governed by the action of the gravitational force only, the particle drag coefficient is very close to zero, so the analytical solution is:

$$Y = Y|_{t=0} + V_{py}|_{t=0} t + g_y \cdot \frac{1}{2} \left(\frac{X - X|_{t=0}}{V_{px}} \right)^2 .$$

The Flow Simulation calculation and the analytical solution for this case are presented in Fig. 18.5.. It is seen that the Flow Simulation calculation coincides with the analytical solution.

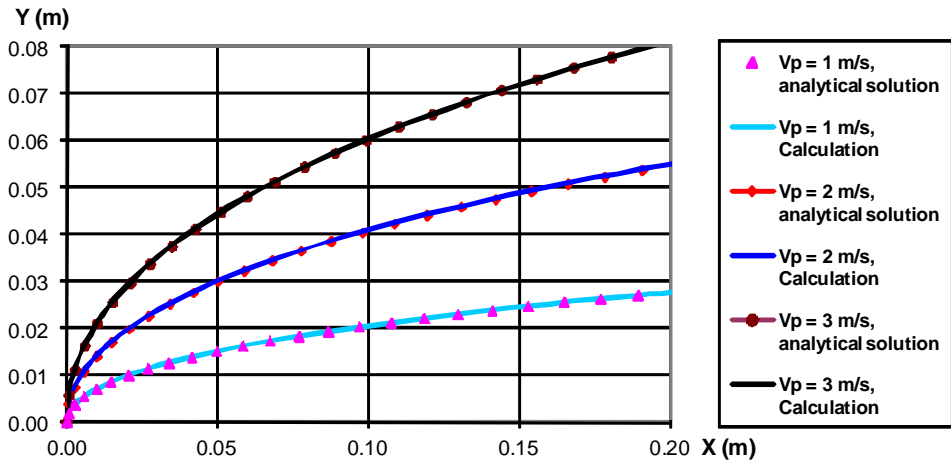


Fig. 18.4. Particle trajectories in a uniform fluid flow at $Re_{\max} = 10^5$, predicted by Flow Simulation and obtained from the analytical solution.

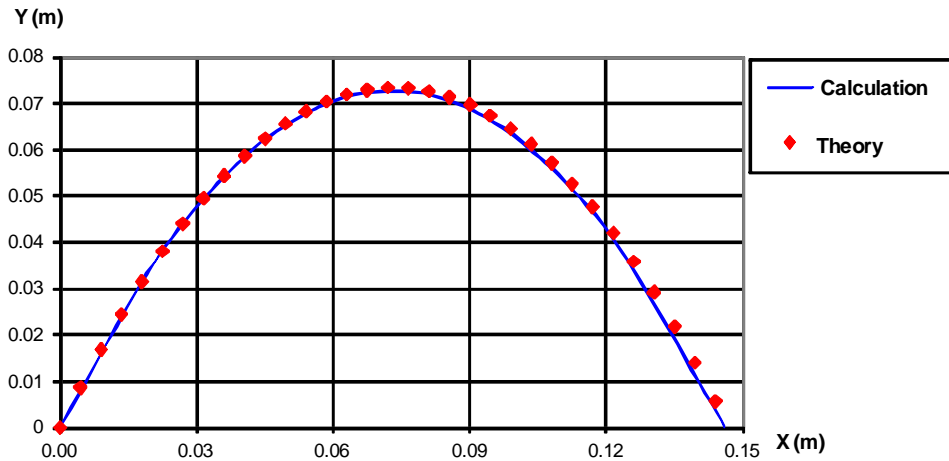


Fig. 18.5. Particle trajectories in the Y-directed gravity, predicted by Flow Simulation and obtained from the analytical solution.

19 Porous Screen in a Non-uniform Stream

Let us now validate the Flow Simulation capability to calculate fluid flows through porous media.

Here, following Ref. 2, we consider a plane cold air flow between two parallel plates, through a porous screen installed between them, see Fig. 19.1.. At the channel inlet the air stream velocity profile is step-shaped (specified). The porous screen (gauze) levels this profile to a more uniform profile. This effect depends on the screen drag, see Ref. 2.

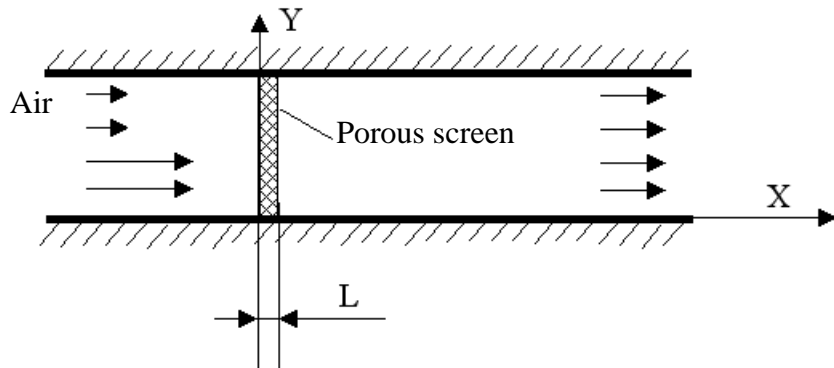


Fig. 19.1. Leveling effect of a porous screen (gauze) on a non-uniform stream.

The SolidWorks model used for calculating the 2D (in XY-plane) flow is shown in Fig. 19.2.. The channel has height of 0.15 m, the inlet (upstream of the porous screen) part of the 0.3 m length, the porous screen of the 0.01 m thickness, and the outlet (downstream of the porous screen) part of the 0.35 m length. All the walls have thickness of 0.01 m.

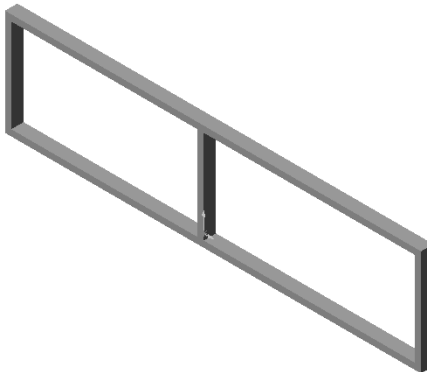


Fig. 19.2. The SolidWorks model used for calculating the 2D flow between two parallel plates and through the porous screen with Flow Simulation.

Following Ref. 2, we consider porous screens (gauzes) of different drag, ζ :

$\zeta = 0.95, 1.2, 2.8$, and 4.1 , defined as:

$$\zeta = \frac{2\Delta P}{\rho V^2} ,$$

where ΔP is the pressure difference between the screen sides, $\rho V^2/2$ is the dynamic pressure (head) of the incoming stream.

Since in Flow Simulation a porous medium's resistance to flow is characterized by parameter $k = -gradP/\rho V$, then for the porous screens $k = V \cdot \zeta / (2L)$, where V is the fluid velocity, L is the porous screen thickness. In Flow Simulation, this form of a porous medium's resistance to flow is specified as $k = (A \cdot V + B)/\rho$, so $A = \rho \cdot \zeta / (2L)$, $B = 0$ for the porous screens under consideration. Therefore, taking $L = 0.01$ m and $\rho = 1.2$ kg/m³ into account, we specify $A = 57, 72, 168$, and 246 kg/m⁻⁴ for the porous screens under consideration. In accordance with the screens' nature, their permeability is specified as isotropic.

According to the experiments presented in Ref.2, the step-shaped velocity profiles $V(Y)$ presented in Fig. 19.3. have been specified at the model inlet. The static pressure of 1 atm has been specified at the model outlet.

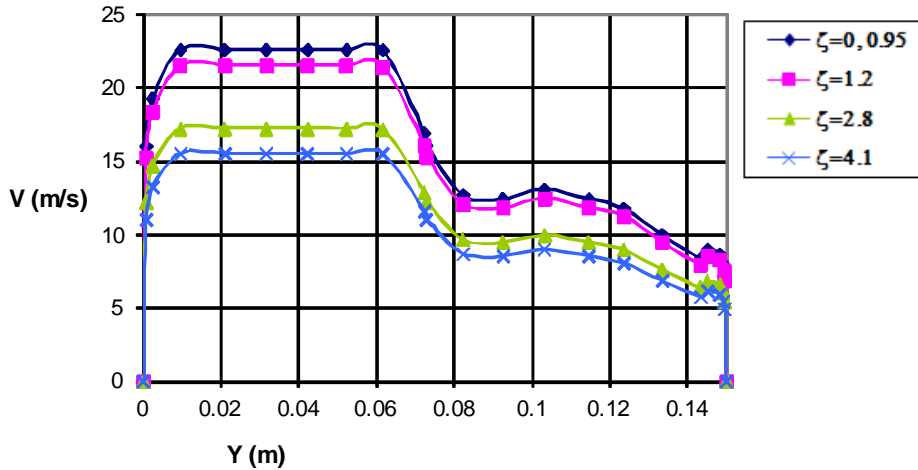


Fig. 19.3. Inlet velocity profiles.

The air flow dynamic pressure profiles at the 0.3 m distance downstream from the porous screens, both predicted by Flow Simulation at result resolution level 5 and measured in the Ref. 2 experiments, are presented in Fig. 19.4. for the $\zeta = 0$ case (i.e., without screen) and Figs.19.5-19.8 for the porous screens of different ζ .

It is seen that the Flow Simulation predictions agree well, both qualitatively and quantitatively, with the experimental data both in absence of a screen and for all the porous screens (gauzes) under consideration, demonstrating the leveling effect of the gauze screens on the step-shaped incoming streams. The prediction error in the dynamic pressure maximum does not exceed 30%.

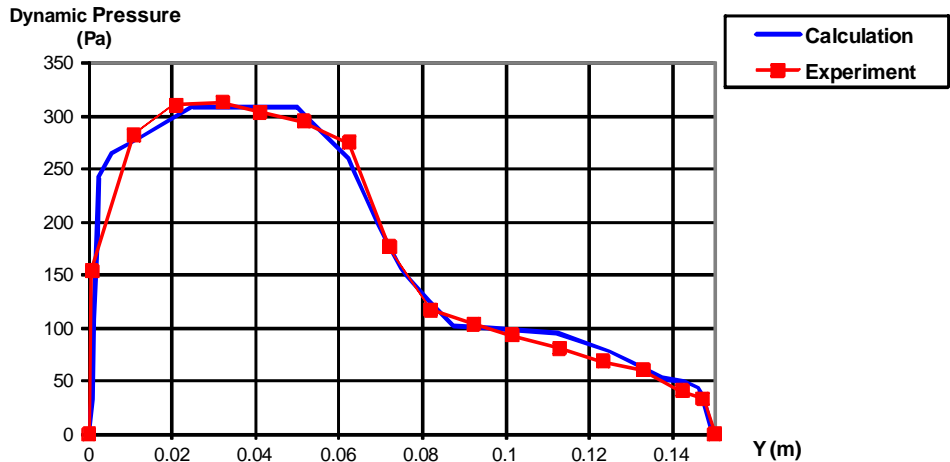


Fig. 19.4. The dynamic pressure profiles at $\zeta = 0$, predicted by Flow Simulation and compared to the Ref. 2 experiments.

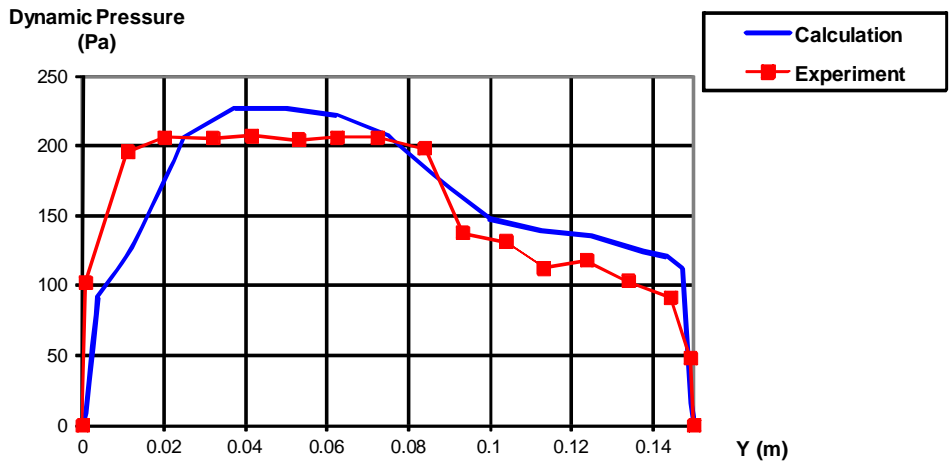


Fig. 19.5. The dynamic pressure profiles at $\zeta = 0.95$, predicted by Flow Simulation and compared to the Ref. 2 experiments.

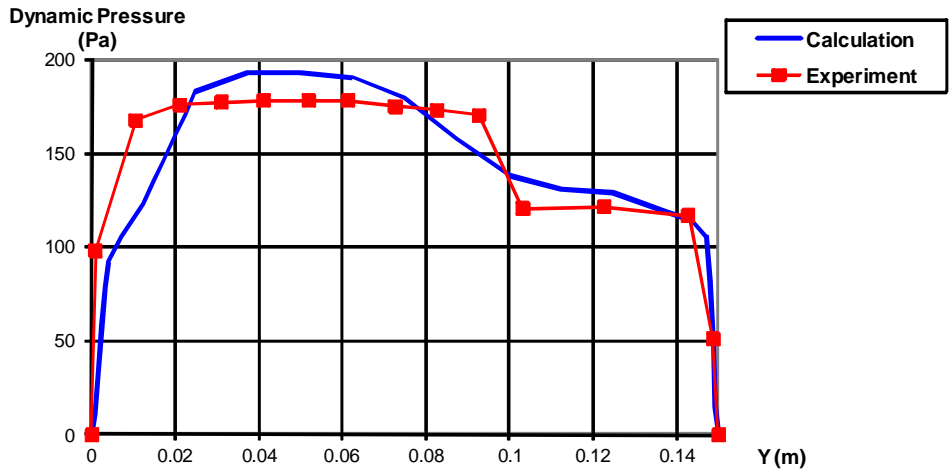


Fig. 19.6. The dynamic pressure profiles at $\zeta = 1.2$, predicted by Flow Simulation and compared to the Ref. 2 experiments.

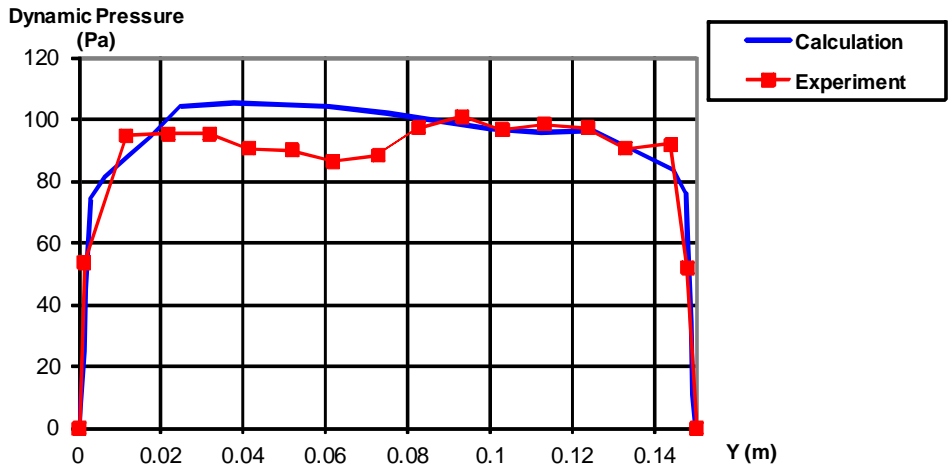


Fig. 19.7. The dynamic pressure profiles at $\zeta = 2.8$, predicted by Flow Simulation and compared to the Ref. 2 experiments.

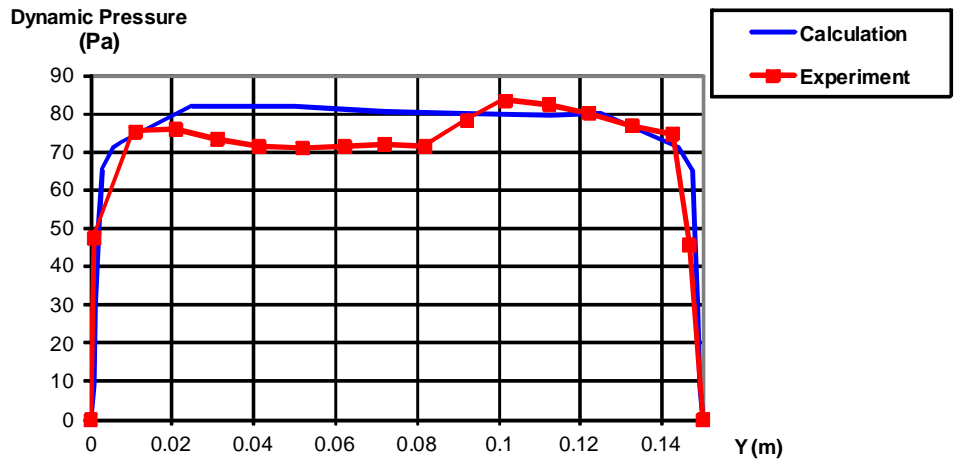


Fig. 19.8. The dynamic pressure profiles at $\zeta = 4.1$, predicted by Flow Simulation and compared to the Ref. 2 experiments.

20 Lid-driven Flows in Triangular and Trapezoidal Cavities

Let us now see how Flow Simulation predicts lid-driven (i.e., shear-driven) 2D recirculating flows in closed 2D triangular and trapezoidal cavities with one or two moving walls (lids) in comparison with the calculations performed in Ref. 21 and Ref. 20.

These two cavities are shown in Fig. 20.1.. The triangular cavity has a moving top wall, the trapezoidal cavity has a moving top wall also, whereas its bottom wall is considered in two versions: as motionless and as moving at the top wall velocity. The no-slip conditions are specified on all the walls.

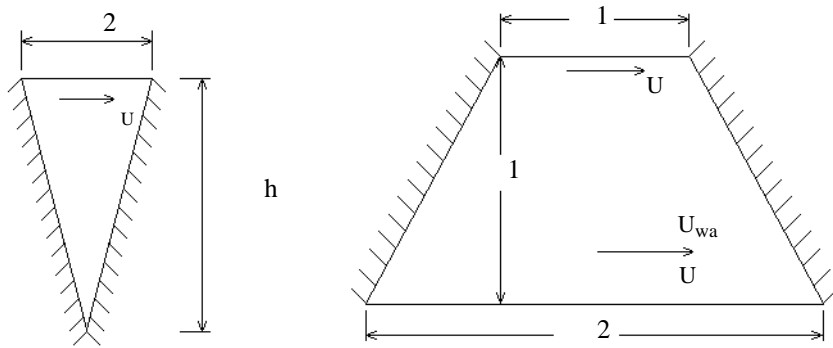


Fig. 20.1. The 2D triangular (left) and trapezoidal (right) cavities with the moving walls (the motionless walls are shown with dashes).

As shown in Ref. 21 and Ref. 20, the shear-driven recirculating flows in these cavities are fully governed by their Reynolds numbers $Re = \rho \cdot U_{wall} \cdot h / \mu$, where ρ is the fluid density, μ is the fluid dynamic viscosity, U_{wall} is the moving wall velocity, h is the cavity height. So, we can specify the height of the triangular cavity $h = 4$ m, the height of the trapezoidal cavity $h = 1$ m, $U_{wall} = 1$ m/s for all cases under consideration, the fluid density $\rho = 1$ kg/m³, the fluid dynamic viscosity $\mu = 0.005$ Pa·s in the triangular cavity produces a $Re = 800$, and $\mu = 0.01, 0.0025, 0.001$ Pa·s in the trapezoidal cavity produces a $Re = 100, 400, 1000$, respectively.

The cavities' models are shown in Fig. 20.2.. The Flow Simulation calculation of flow in the triangular cavity has been performed on the 48×96 computational mesh. The results in comparison with those from Ref. 21 are presented in Fig. 20.3. (streamlines) and in Fig. 20.4. (the fluid velocity X-component along the central vertical bisector shown by a green line in Fig. 20.2.). A good agreement of these calculations is clearly seen.

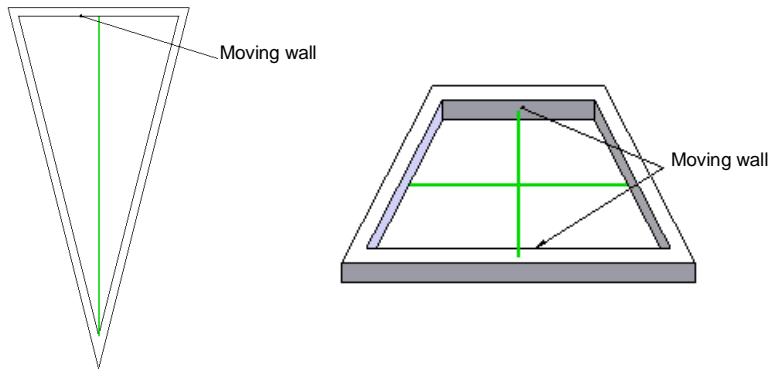


Fig. 20.2. The models for calculating the lid-driven 2D flows in the triangular (left) and trapezoidal (right) cavities with Flow Simulation.

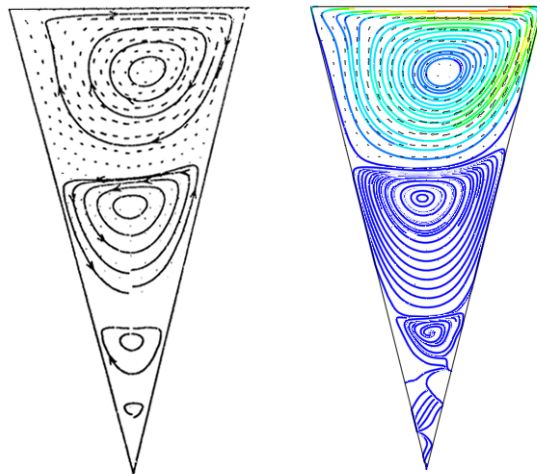


Fig. 20.3. The flow trajectories in the triangular cavity, calculated by Flow Simulation (right) and compared to the Ref. 21 calculation (left).

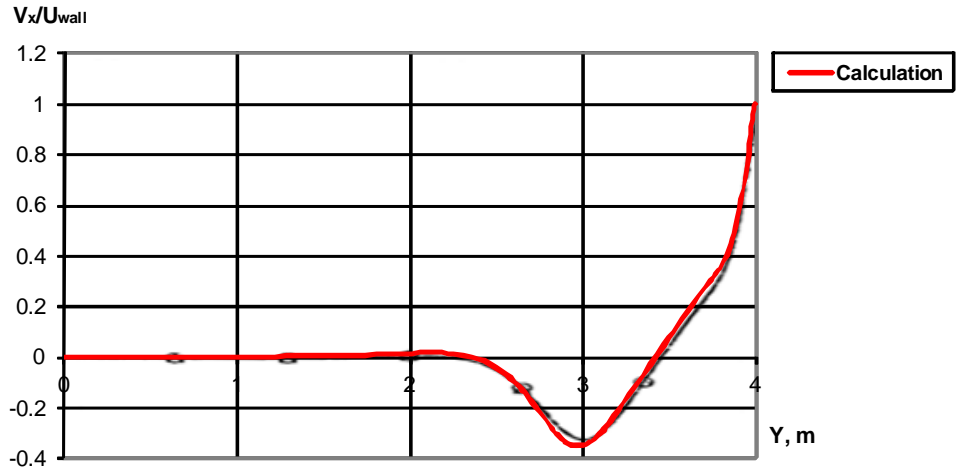


Fig. 20.4. The triangular cavity's flow velocity X-component along the central vertical bisector, calculated by Flow Simulation (red line) and compared to the Ref. 21 calculation (black line with circlets).

The Flow Simulation calculations of flows in the trapezoidal cavity with one and two moving walls at different Re values have been performed with the 100x50 computational mesh. Their results in comparison with those from Ref.16 are presented in Fig. 20.5.-20.10 (streamlines) and in Fig. 20.11. (the fluid velocity X-component along the central vertical bisector shown by a green line in Fig. 20.2.). A good agreement of these calculations is seen.

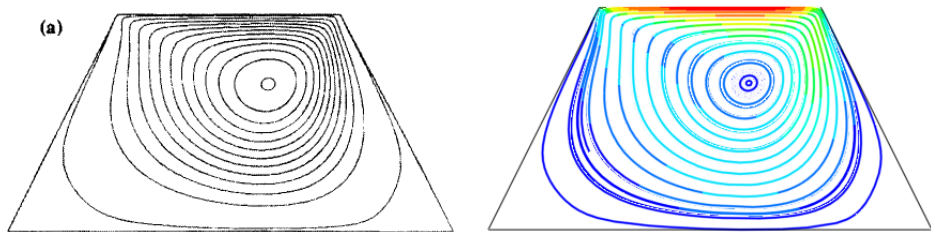


Fig. 20.5. The flow streamlines in the trapezoidal cavity with a top only moving wall at Re = 100, calculated by Flow Simulation (right) and compared to the Ref. 20 calculation (left).

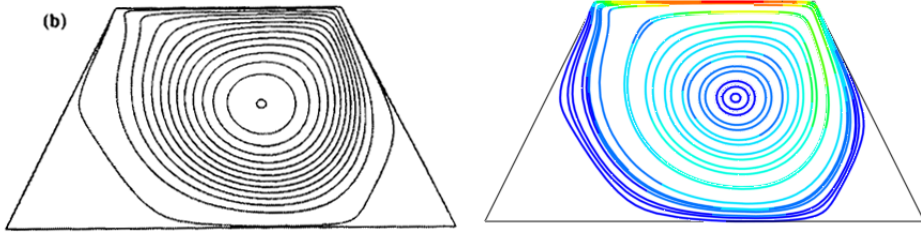


Fig. 20.6. The flow streamlines in the trapezoidal cavity with a top only moving wall at $Re = 400$, calculated by Flow Simulation (right) and compared to the Ref. 20 calculation (left).

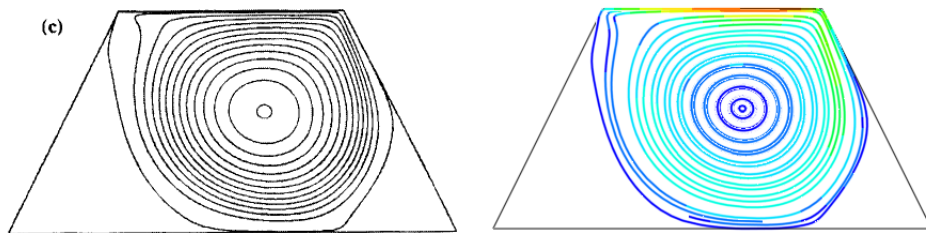


Fig. 20.7. The flow streamlines in the trapezoidal cavity with a top only moving wall at $Re = 1000$, calculated by Flow Simulation (right) and compared to the Ref. 20 calculation (left).

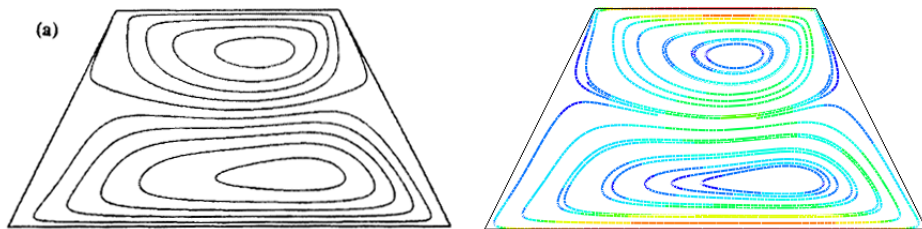


Fig. 20.8. The flow streamlines in the trapezoidal cavity with two moving walls at $Re = 100$, calculated by Flow Simulation (right) and compared to the Ref. 20 calculation (left).

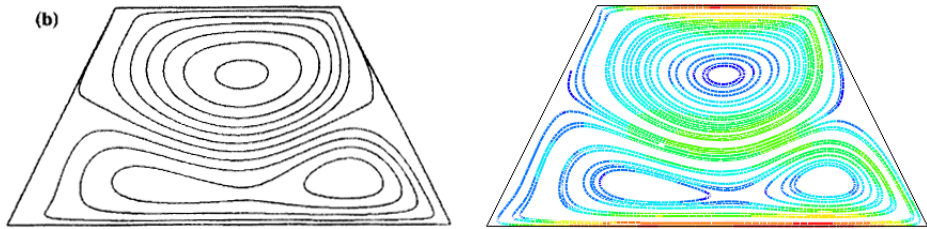


Fig. 20.9. The flow streamlines in the trapezoidal cavity with two moving walls at $Re = 400$, calculated by Flow Simulation (right) and compared to the Ref. 20 calculation (left).

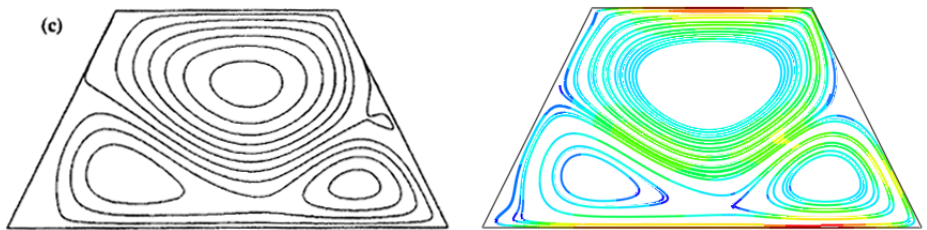


Fig. 20.10. The flow streamlines in the trapezoidal cavity with two moving walls at $Re = 1000$, calculated by Flow Simulation (right) and compared to the Ref. 20 calculation (left).

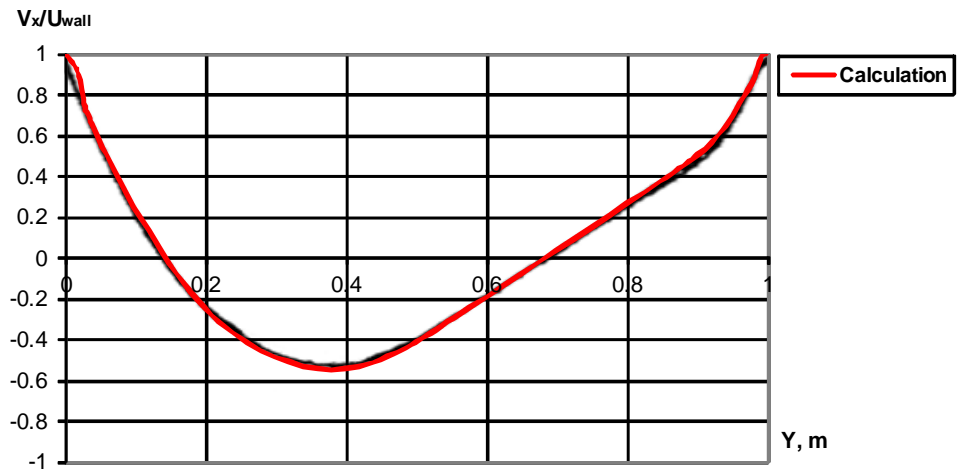


Fig. 20.11. The flow velocity X-component along the central vertical bisector in the trapezoidal cavity with two moving walls at $Re = 400$, calculated by Flow Simulation (red line) and compared to the Ref. 20 calculation (black line).

21 Flow in a Cylindrical Vessel with a Rotating Cover

Let us now see how Flow Simulation predicts a 3D recirculating flow in a cylindrical vessel closed by a rotating cover (see Fig. 21.1.) in comparison with the experimental data presented in Ref. 21 (also in Ref. 22). This vessel of $R = h = 0.144$ m dimensions is filled with a glycerol/water mixture. The upper cover rotates at the angular velocity of Ω . The other walls of this cavity are motionless. The default no-slip boundary condition is specified for all walls.

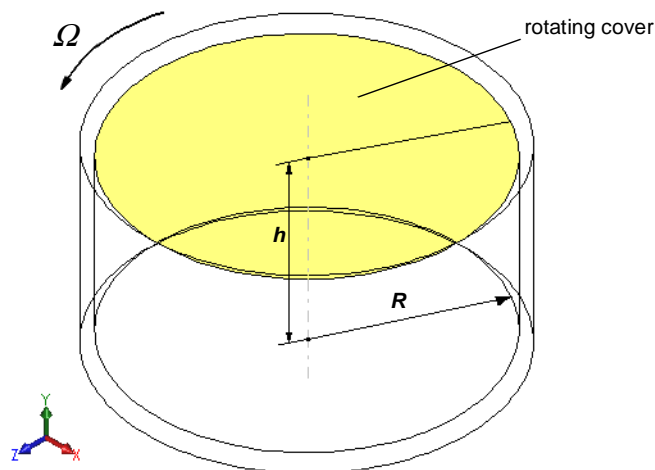


Fig. 21.1. The cylindrical vessel with the a rotating cover.

Due to the cover rotation, a shear-driven recirculating flow forms in this vessel. Such flows are governed by the Reynolds number $Re = \rho \cdot \Omega \cdot R^2 / \mu$, where ρ is the fluid density, μ is the fluid dynamic viscosity, Ω is the angular velocity of the rotating cover, R is the radius of the rotating cover. In the case under consideration the 70/30% glycerol/water mixture has $\rho = 1180 \text{ kg/m}^3$, $\mu = 0.02208 \text{ Pa}\cdot\text{s}$, the cover rotates at $\Omega = 15.51 \text{ rpm}$, so $Re = 1800$.

The Flow Simulation calculation has been performed on the $82 \times 41 \times 82$ computational mesh. The formed flow pattern (toroidal vortex) obtained in this calculation is shown in Fig. 21.2. using the flow velocity vectors projected onto the XY-plane. The tangential and radial components of the calculated flow velocity along four vertical lines arranged in the XY-plane at different distances from the vessel axis in comparison with the Ref. 21 experimental data are presented in Figs. 21.3-7 in the dimensionless form (the Y-coordinate is divided by R , the velocity components are divided by $\Omega \cdot R$). There is good agreement with the calculation results and the experimental data shown.

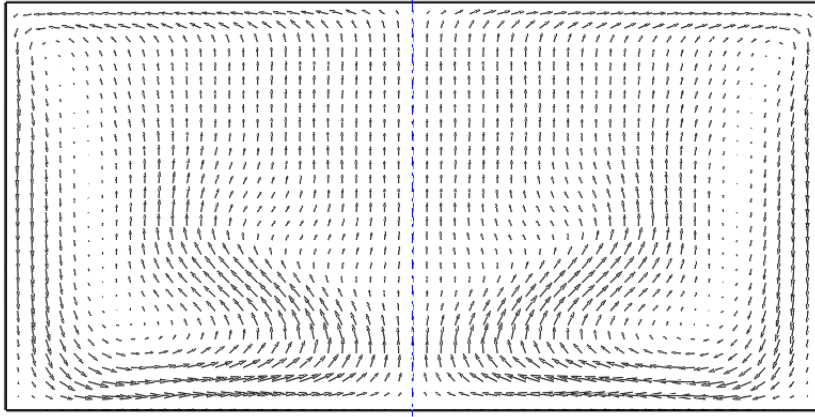


Fig. 21.2. The vessel's flow velocity vectors projected on the

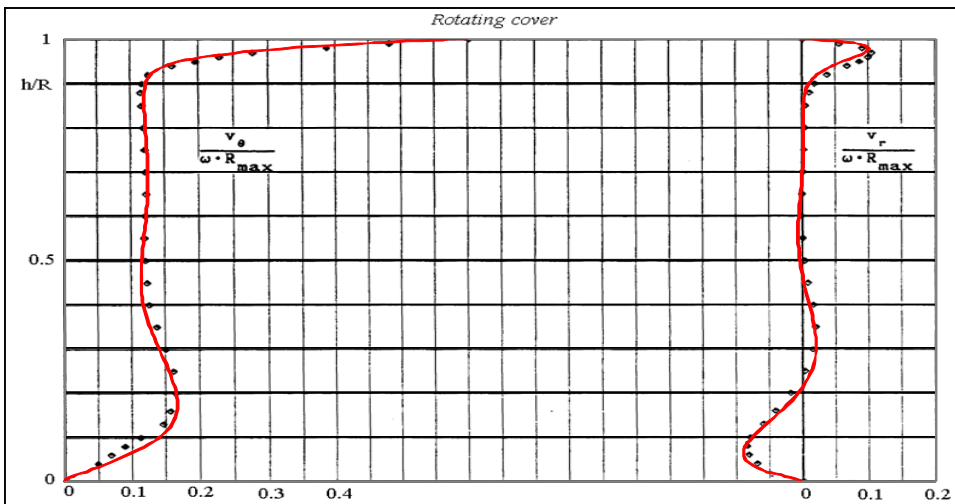


Fig. 21.3. The vessel's flow tangential and radial velocity components along the $X = 0.6$ vertical, calculated by Flow Simulation (red) and compared to the Ref. 21 experimental data.

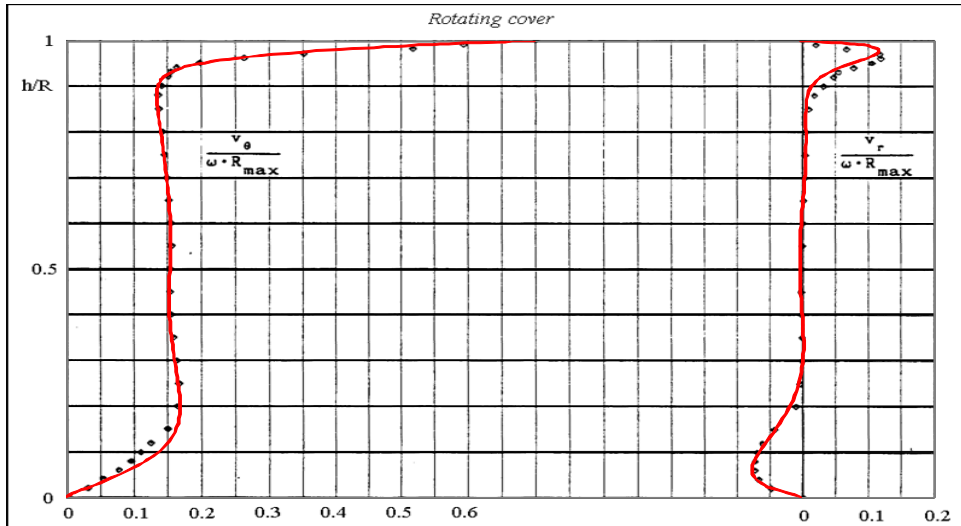


Fig. 21.4. The vessel's flow tangential and radial velocity components along the X = 0.7 vertical, calculated by Flow Simulation (red) and compared to the Ref. 21 experimental data.

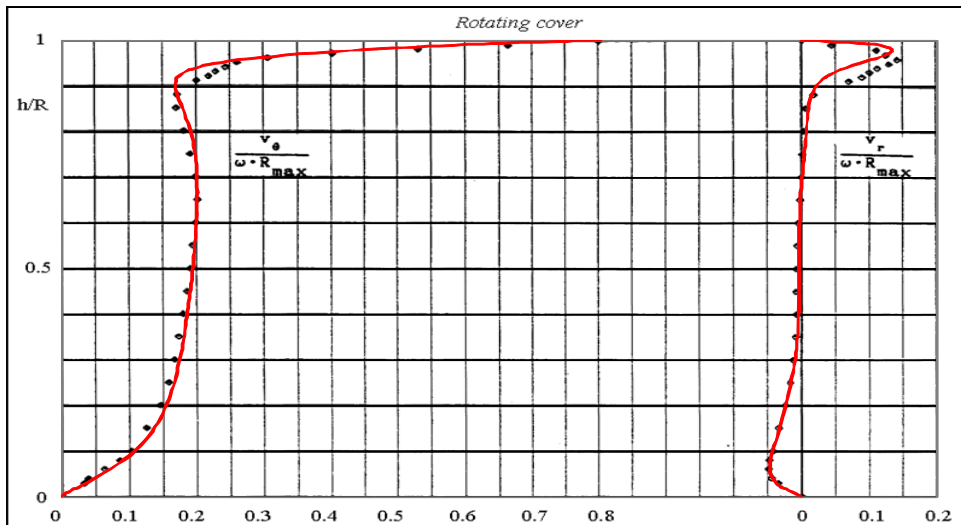


Fig. 21.5. The vessel's flow tangential and radial velocity components along the X = 0.8 vertical, calculated by Flow Simulation (red) and compared to the Ref. 21 experimental data.

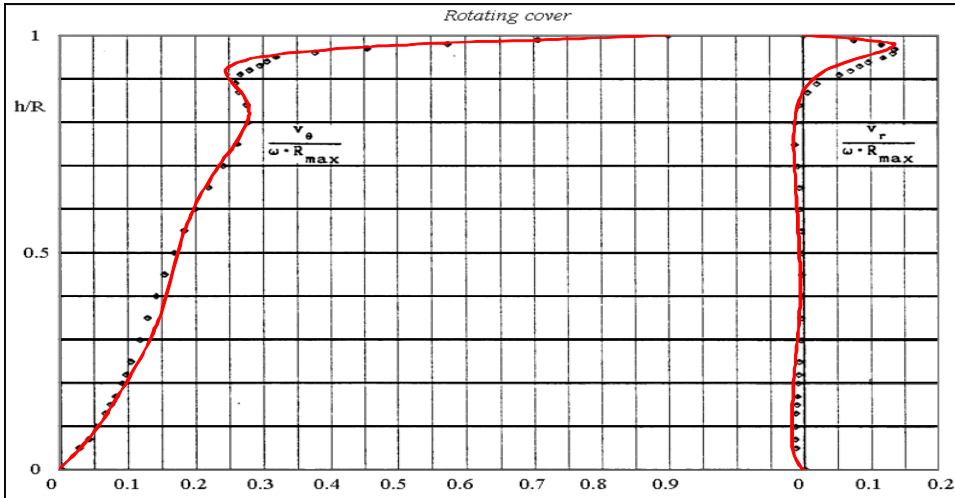


Fig. 21.6. The vessel's flow tangential and radial velocity components along the $X = 0.9$ vertical, calculated by Flow Simulation (red) and compared to the Ref. 21 experimental data.

22 Flow in an Impeller

Let us now validate the Flow Simulation ability to perform calculations in a rotating coordinate system related to a rotating solid. Following Ref. 23, we will consider the flow of water in a 9-bladed centrifugal impeller having blades tilted at a constant 60° angle with respect to the intersecting radii and extending out from the 320 mm inner diameter to the 800 mm outer diameter (see Fig. 22.1.). The water in this impeller flows from its center to its periphery. To compare the calculation with the experimental data presented in Ref.22, the impeller's angular velocity of 32 rpm and volume flow rate of $0.00926 \text{ m}^3/\text{s}$ are specified.

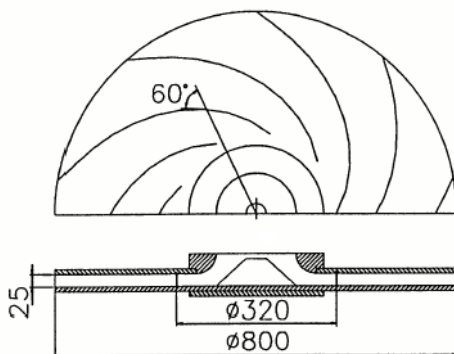


Fig. 22.1. The impeller's blades geometry.

Since the impeller's inlet geometry and disk extension serving as the impeller's vaneless diffuser have no exact descriptions in Ref. 23, to perform the validating calculation we arbitrarily specified the annular inlet as 80 mm in diameter with a uniform inlet velocity profile perpendicular to the surface in the stationary coordinate system. The impeller's disk's external end was specified as 1.2 m diameter, as shown in Fig. 22.2..

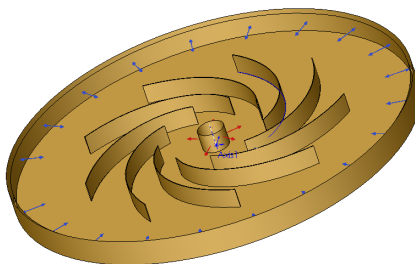


Fig. 22.2. The model used for calculating the 3D flow in the impeller.

The above-mentioned volume flow rate at the annular inlet and the potential pressure of 1 atm at the annular outlet are specified as the problem's flow boundary conditions.

The Flow Simulation 3D flow calculation is performed on the computational mesh using the result resolution level of 5 and the minimum wall thickness of 2 mm (since the blades have constant thickness). To further capture the curvature of the blades a local initial mesh was also used in the area from the annular inlet to the blades' periphery. As a result, the computational mesh has a total number of about 1,000,000 cells.

Following Ref. 23, let us compare the passage-wise flow velocities (w_s , see their definition in Fig. 22.3., $\beta = 60^\circ$) along several radial lines passing through the channels between the blades (lines g, j, m, p in Fig. 22.4.) at the mid-height between the impeller's disks.

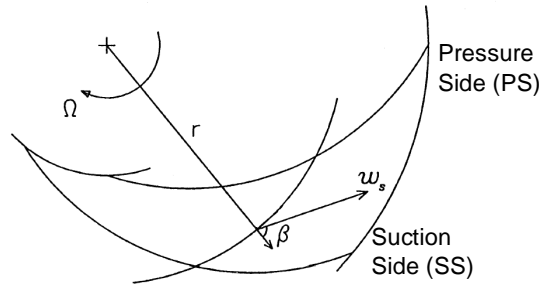


Fig. 22.3. Definition of the passage-wise flow velocity.

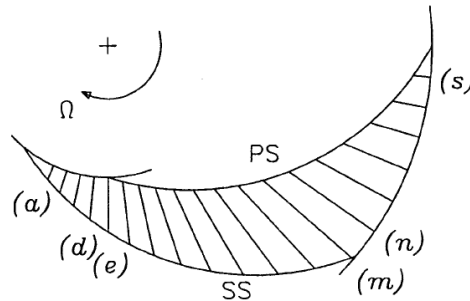


Fig. 22.4. Definition of the reference radial lines along which the passage-wise flow velocity was measured in Ref. 23 (from a to s in the alphabetical order).

The passage-wise flow velocities divided by Ωr_2 , where Ω is the impeller's angular velocity and $r_2 = 400$ mm is the impeller's outer radius, which were measured in Ref. 23 and obtained in the performed Flow Simulation calculations, are shown in Fig. 22.5., 6, 7, and 8. In these figures, the distance along the radial lines is divided by the line's length. The Flow Simulation results are presented in each of these figures by the curve obtained by averaging the corresponding nine curves in all the nine flow passages between the impeller blades. The calculated passage-wise flow velocity's cut plot covering the whole computational domain at the mid-height between the impeller's disks is shown in Fig. 22.9.. Here, the g, j, m, p radial lines in each of the impeller's flow passages are shown. A good agreement of these calculation results with the experimental data is seen.

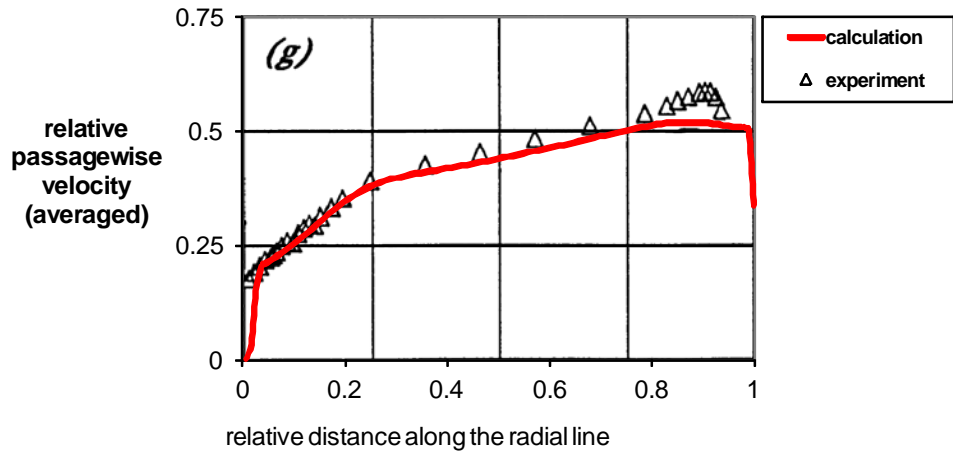


Fig. 22.5. The impeller's passage-wise flow velocity along the *g* (see Fig. 22.4.) radial line, calculated by Flow Simulation and compared to the experimental data.

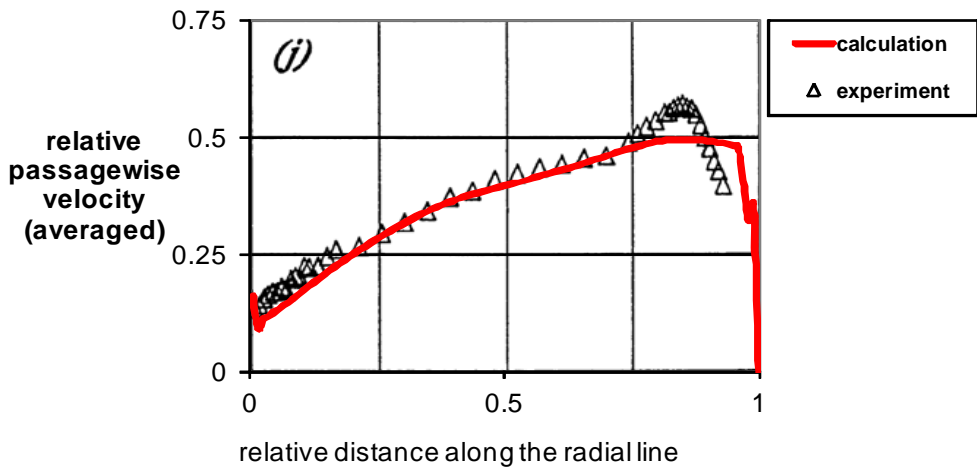


Fig. 22.6. The impeller's passage-wise flow velocity along the *j* (see Fig. 22.4.) radial line, calculated by Flow Simulation and compared to the experimental data.

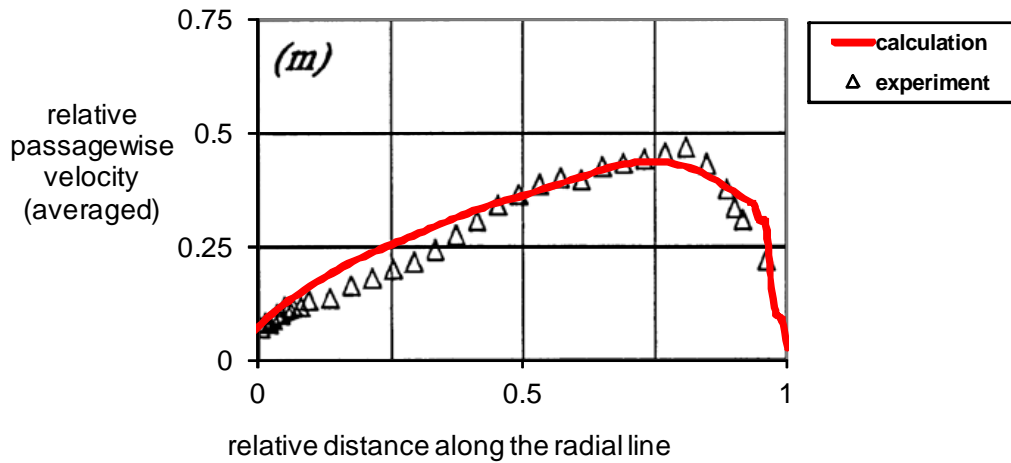


Fig. 22.7. The impeller's passage-wise flow velocity along the m (see Fig. 22.4.) radial line, calculated by Flow Simulation and compared to the experimental data.

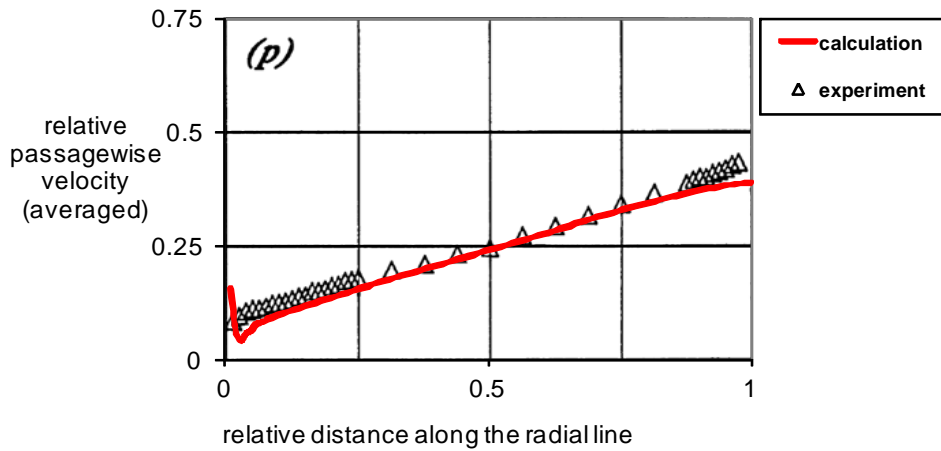


Fig. 22.8. The impeller's passage-wise flow velocity along the p (see Fig. 22.4.) radial line, calculated by Flow Simulation and compared to the experimental data.

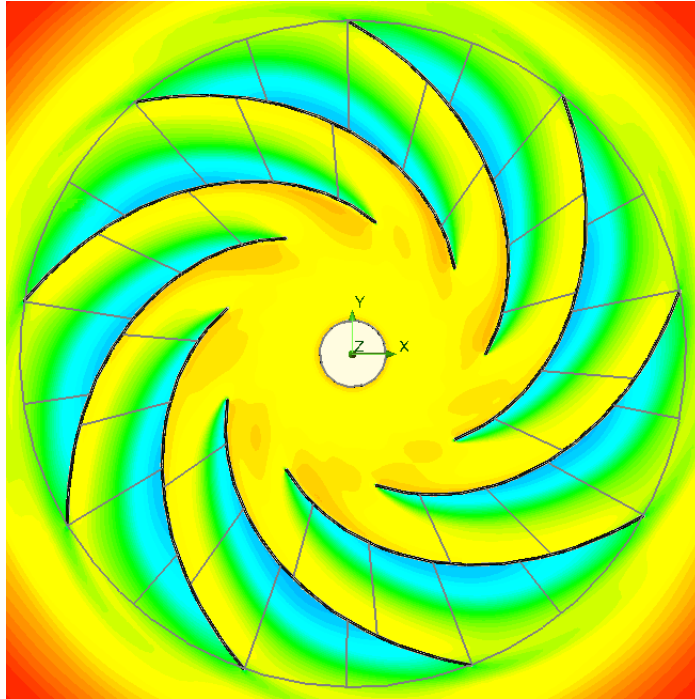


Fig. 22.9. A cut plot of the impeller's passage-wise flow velocity calculated by Flow Simulation.

23 Cavitation on a hydrofoil

When the local pressure at some point in the liquid drops below the liquid's vapour pressure at the local temperature, the liquid undergoes phase transition and form cavities filled with the liquid's vapor with an addition of gas that has been dissolved in the liquid. This phenomenon is called cavitation.

In this validation example we consider Flow Simulation abilities to model cavitation on the example of water flow around a symmetric hydrofoil in a water-filled tunnel. The calculated results were compared with the experimental data from Ref. 24.

The problem is solved in the 2D setting. A symmetric hydrofoil with the chord c of 0.305 m is placed in a water-filled tunnel with the angle of attack of 3.5° . The part of the tunnel being modelled has the following dimensions: length $l = 2$ m and height $h = 0.508$ m. The calculation is performed four times with different values of the cavitation number σ defined as follows:

$$\sigma = \frac{P_\infty - P_v}{\frac{1}{2} \rho U_\infty^2}$$

where P_∞ is the inlet pressure, P_v is the saturated water vapor pressure equal to 2340 Pa at given temperature (293.2 K), ρ is the water density at inlet, and U_∞ is the water velocity at inlet (see Fig. 23.1.).

The inlet boundary condition is set up as `Inlet Velocity` of 8 m/s. On the tunnel outlet an `Environment Pressure` is specified so that by varying it one may tune the cavitation number to the needed value. The project fluid is water with the cavitation option switched on, and the mass fraction of non-condensable gas is set to $5 \cdot 10^{-5}$. A local initial mesh was created in order to resolve the cavitation area better. The resulting mesh contains about 30000 cells.

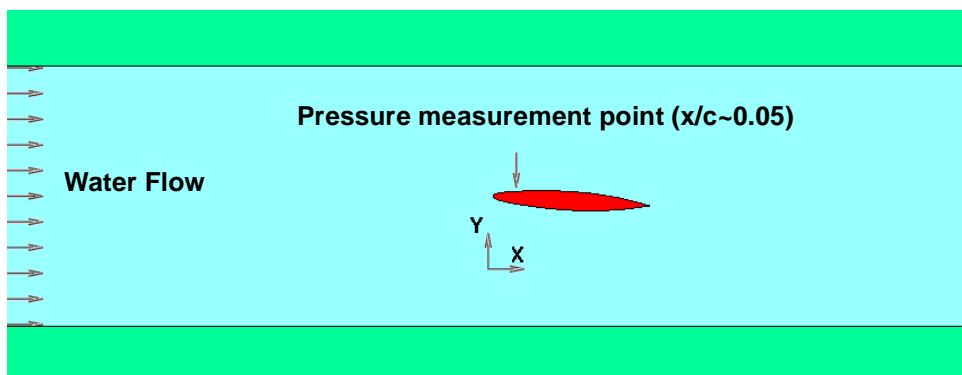


Fig. 23.1. The model geometry.

The qualitative comparison in a form of cut plots with Vapor Volume Fraction as the visualization parameter are shown on Fig. 23.2.

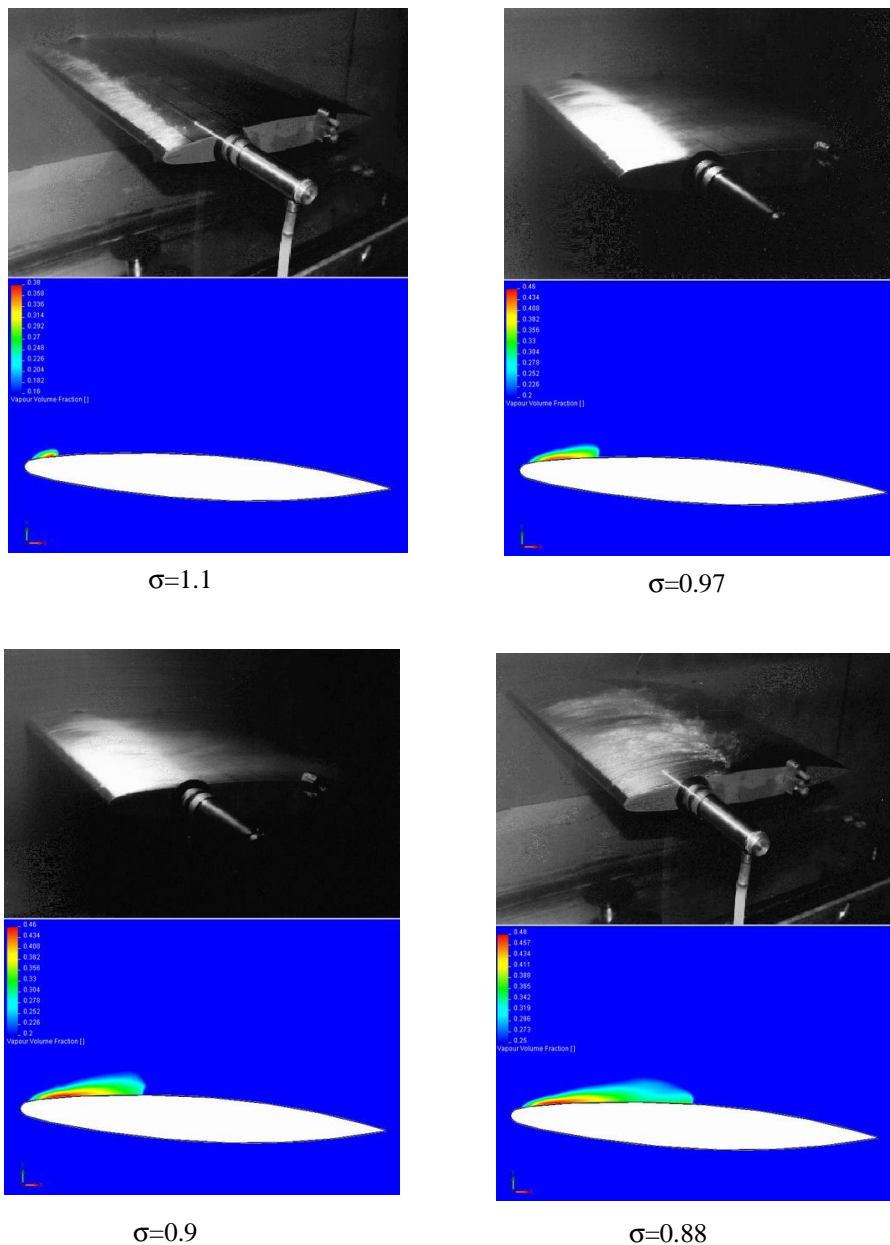


Fig. 23.2. A comparison of calculated and experimentally observed cavitation areas for different σ

The calculated length of the cavitation area was derived from the distribution of the Vapor Volume Fraction parameter over the hydrofoil's surface as the distribution's width at half-height. The results are presented on Fig. 23.3.

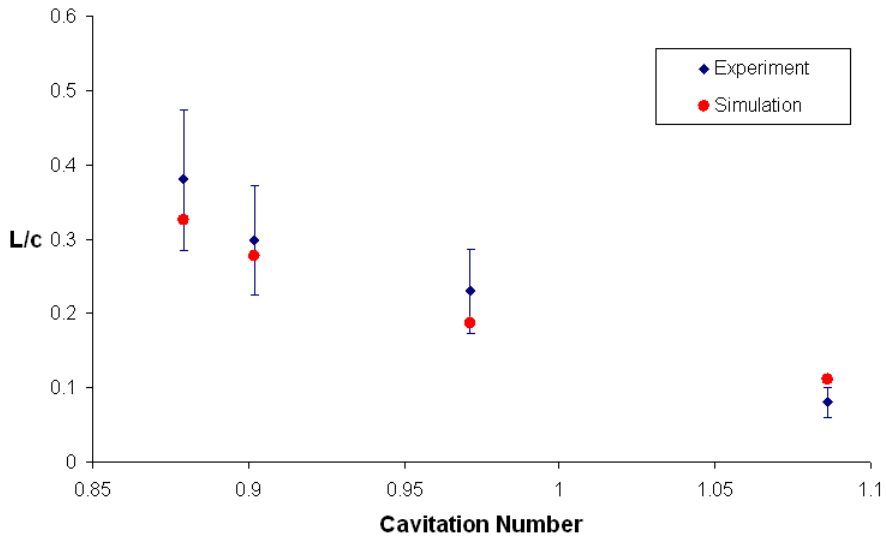


Fig. 23.3. A comparison of calculated and measured cavitation lengths

According to Ref. 24, the "clear appearance" of the cavity becomes worse for larger cavity lengths. The experimental data also confirm that the amount of uncertainty increases with increasing cavity extent. Taking these factors into account together with the comparison performed above, we can see that the calculated length of the cavitation area agrees well with the experiment for a wide range of cavitation numbers.

Pressure measurements were performed on the hydrofoil surface at $x/c = 0.05$ in order to calculate the pressure coefficient defined as follows:

$$-C_p = \frac{P_\infty - P_{x/c=0.05}}{\frac{1}{2} \rho U_\infty^2}$$

A comparison of the calculated and experimental values of this parameter is presented on Fig. 23.4. and also shows a good agreement.

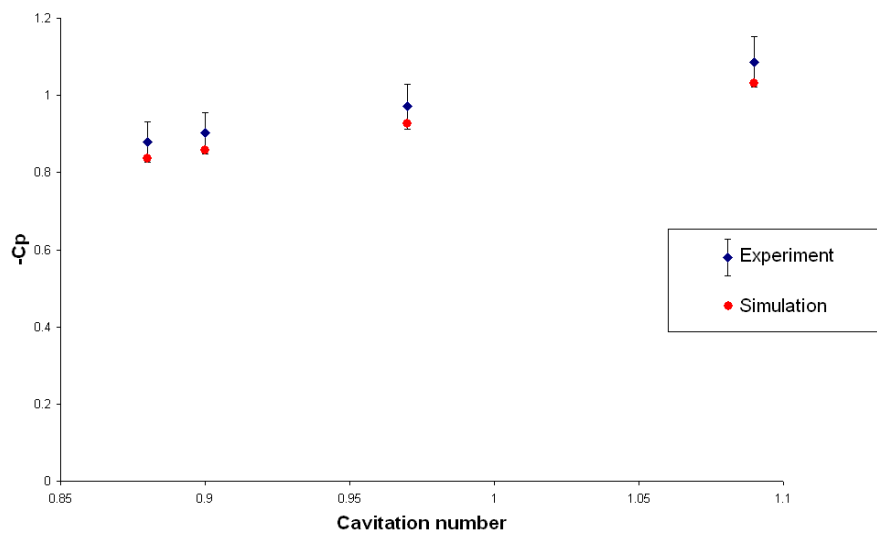


Fig. 23.4. A comparison of calculated and measured pressure coefficient

24 Isothermal Cavitation in a Throttle Nozzle

In this validation example we consider Flow Simulation capabilities to simulate cavitation in industrial liquid flows using the Isothermal cavitation model. The problem studied here validates this model by considering a 3D diesel fuel flow in a throttle channel that was studied experimentally in Ref. 25. According to this work, thermal effects in the considered flow are negligible. Therefore, it is reasonable to apply the Isothermal cavitation model.

Throttle channel geometry with its main dimensions is shown in Fig. 24.1

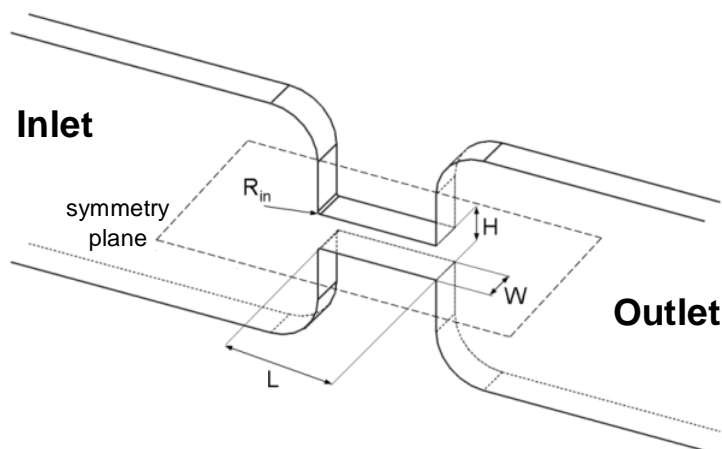


Fig. 24.1 The channel geometry: $L=1\text{mm}$, $H=0.299\text{mm}$, $W=0.3\text{mm}$, $R_{in}=0.02\text{mm}$.

Diesel fuel at 30°C is supplied to the inlet under the pressure (P_{in}) of 100 bar. The outlet pressure (P_{out}) varies from 10 to 70 bar. The properties of the analyzed fuel for the given temperature are presented in Table 24.1.

Table 24.1 Properties of the diesel fuel (2-D) at 30°C .

Density (kg/m^3)	836
Molar Mass (kg/mol)	0.198
Dynamic Viscosity ($\text{Pa}\cdot\text{s}$)	0.0025
Saturation Pressure (Pa)	2000

It is assumed that fuel contains dissolved air. The mass fraction of dissolved air is set to 0.001 to conform with the experimental data.

The objective of the calculations is to obtain channel characteristic under cavitation conditions and compare it with the experimental measurements. Because throttle channel has a symmetry plane, only a half of the model is used to generate the computational mesh. A finer local mesh is used to resolve the flow in the narrow channel and the adjacent regions providing about 15 mesh cells across the channel half-height. Additional refinement is performed in the region near the small fillet R_{in} . The resulting mesh are shown in Fig. 24.2.

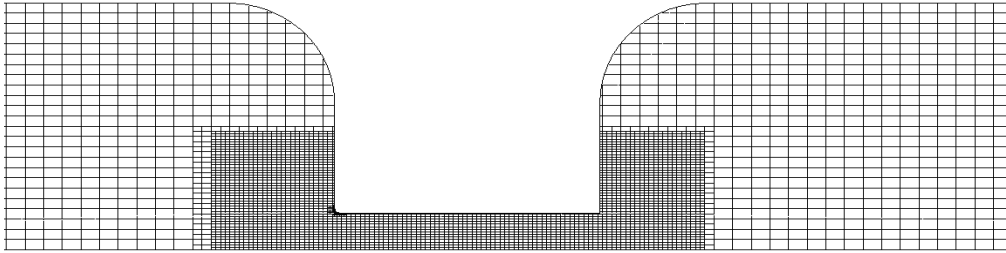


Fig. 24.2 The computational mesh (zoom-view).

Fig. 24.3 shows the distribution of the vapour volume fraction at different pressure drop. This figure provides a view of the initiation and development of the cavitation area.

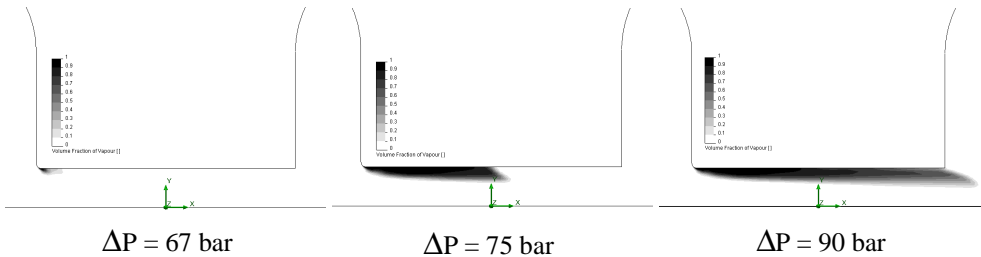


Fig. 24.3 Cavitation fields at symmetry plane.

The dependency of the pressure drop on the mass flow rate both predicted by Flow Simulation and determined experimentally are shown on Fig. 24.4. The difference between the calculations and the experimental measurements is less than 5%. Also, as it can be seen from the Fig. 24.3 and Fig. 24.4, the critical cavitation point corresponds to the pressure drop of about 70 bar. This point defines the transition from a pressure-dependent mass flow to choked mass flow that is induced by cavitation.

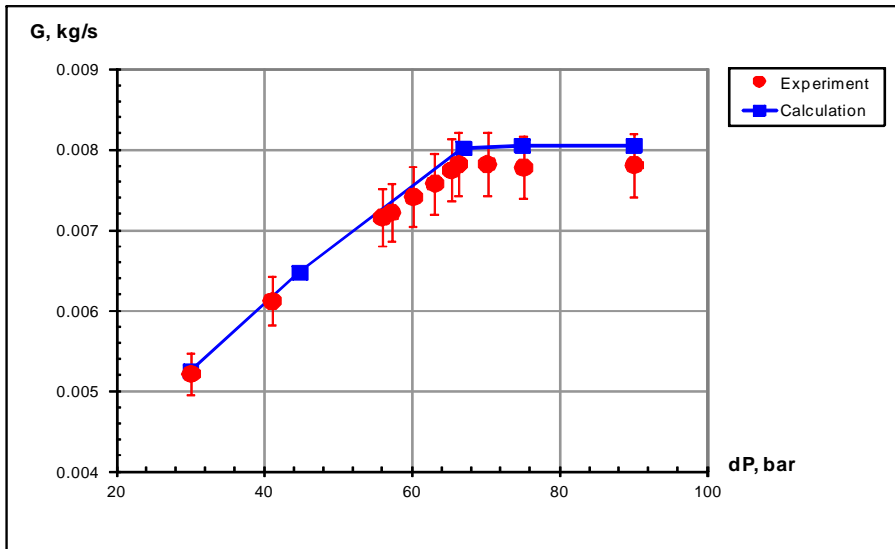


Fig. 24.4 Mass flow rate versus pressure drop at 100 bar inlet pressure in comparison with the experimental data (Ref. 25).

The comparison of the Flow Simulation calculations with the experimental data shows that the application of the Isothermal cavitation model that employs a limited set of fluid properties allows to predict cavitating flow characteristics with the sufficient accuracy.

25 Thermoelectric Cooling

Flow Simulation has the ability to model the work of a thermoelectric cooler (TEC), also known as Peltier element. The device used in this example has been developed for active cooling of an infrared focal plane array detector used during the Mars space mission (see Ref. 26).

According to the hardware requirements, the cooler (see Fig. 25.1.) has the following dimensions: thickness of 4.8 mm, cold side of $8 \times 8 \text{ mm}^2$ and hot side of $12 \times 12 \text{ mm}^2$. It was built up of three layers of semiconductor pellets made of $(\text{Bi,Sb})_2(\text{Se,Te})_3$ -based material. The cooler was designed to work at temperatures of hot surface in the range of 120-180 K and to provide the temperature drop of more than 30 K between its surfaces.

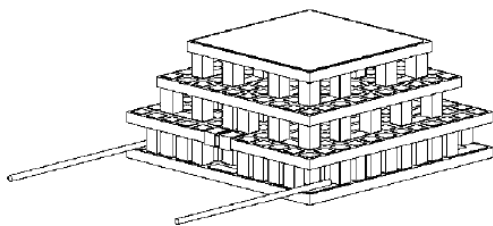


Fig. 25.1. Structure of the thermoelectric cooler.

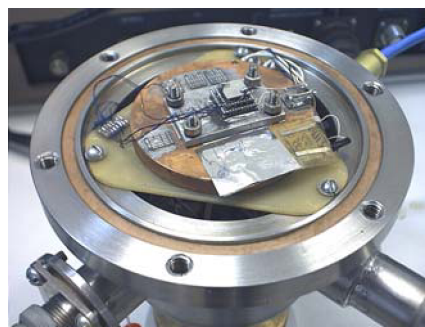


Fig. 25.2. The thermoelectric module test setup. (Image from Ref. 26)

To solve the engineering problem using Flow Simulation, the cooler has been modelled by a truncated pyramidal body with fixed temperature (Temperature boundary condition) on the hot surface and given heat flow (Heat flow boundary condition) on the cold surface (see Fig. 25.3.).

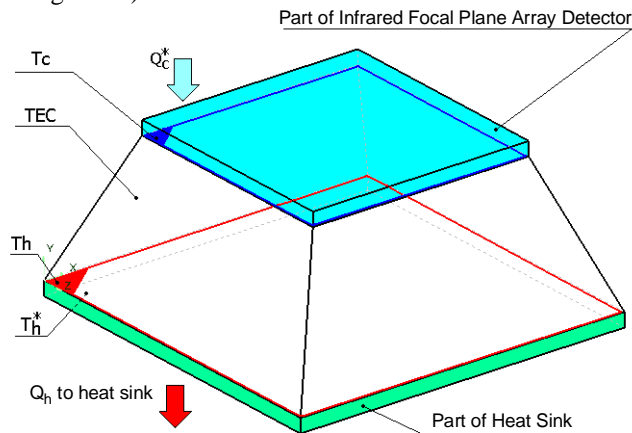


Fig. 25.3. The model geometry.

The TEC characteristics necessary for the modelling, i.e. temperature dependencies of the maximum pumped heat, maximum temperature drop, maximum current strength and maximum voltage, were represented in the Flow Simulation Engineering Database as a linear interpolation between the values taken from Ref. 26 (see Fig. 25.4.).

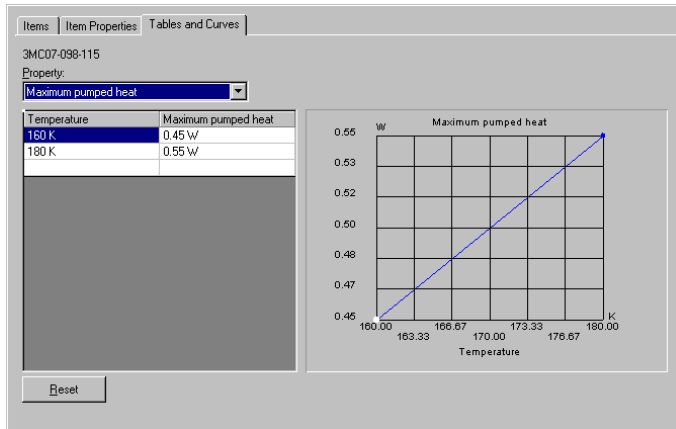


Fig. 25.4. The TEC's characteristics in the Engineering Database.

As it can be seen on Fig. 25.5., the temperature drop between the cooler's hot and cold surfaces in dependence of current agrees well with the experimental data.

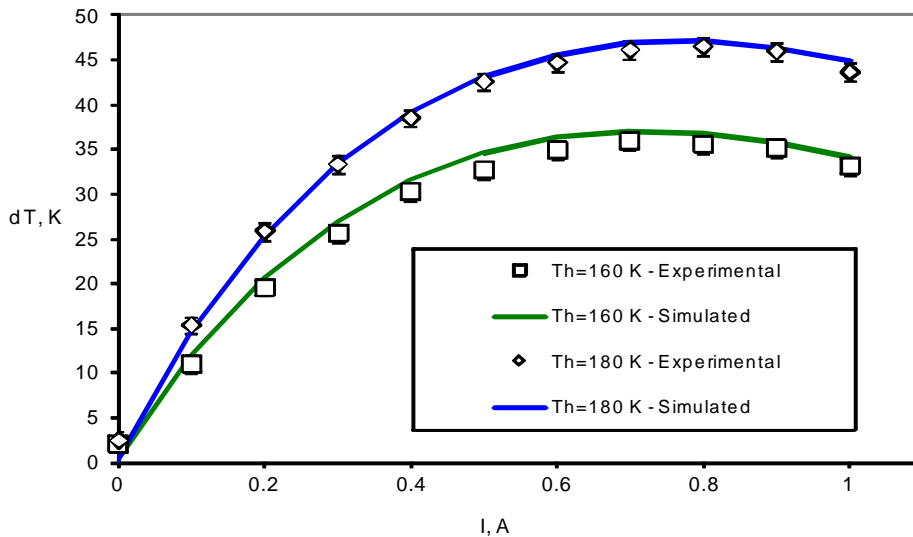


Fig. 25.5. ΔT as a function of current under various T_h .

The dependency of ΔT against heat flow under various T_h (see Fig. 25.6.) is also in a good agreement with the performance data, as well as the coefficient of performance COP (see Fig. 25.7.) defined as follows:

$$COP = \frac{Q_c}{P_{in}} = \frac{Q_c}{Q_h - Q_c}$$

where P_{in} is the cooler's power consumption, and Q_c and Q_h are the heat flows on the cold and hot faces, respectively.

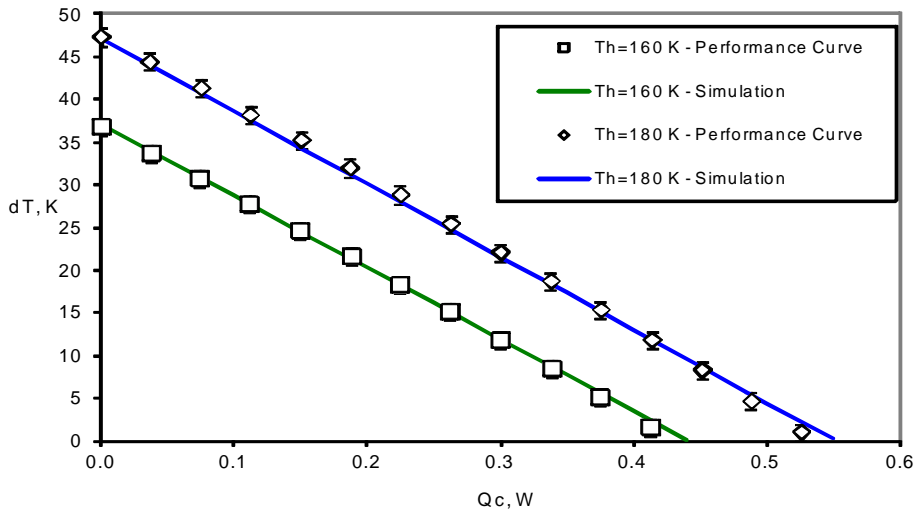


Fig. 25.6. ΔT as a function of heat flow under various T_h .

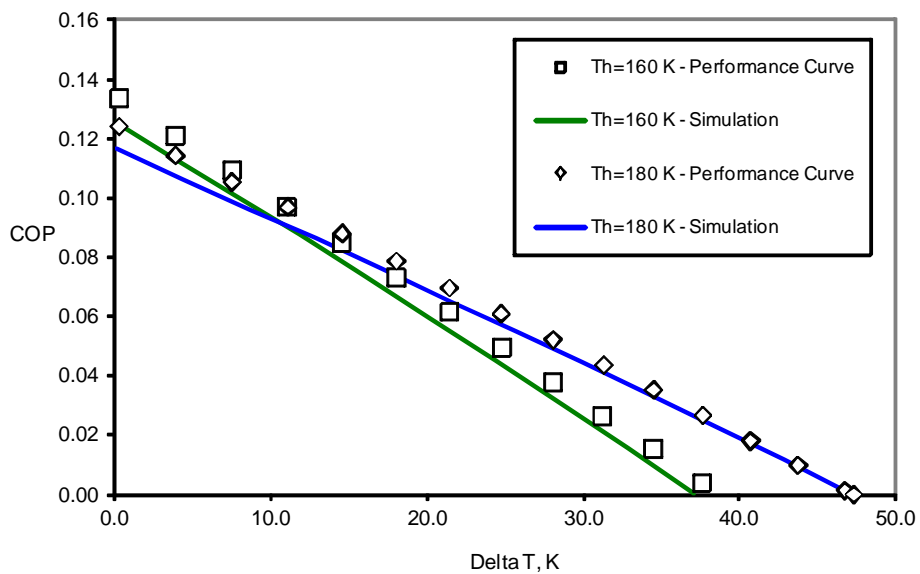


Fig. 25.7. COP as a function of ΔT under various T_h .

Finally, we may conclude that Flow Simulation reproduces thermal characteristics of the thermoelectric coolers at various currents and temperatures with good precision.

References

- 1 Schlichting, H., *Boundary Layer Theory*. 7th ed., McGraw –Hill, New York, 1979.
- 2 Idelchik, I.E., *Handbook of Hydraulic Resistance*. 2nd ed., Hemisphere, New York, 1986.
- 3 Panton, R.L., *Incompressible Flow*. 2nd ed., John Wiley & Sons, Inc., 1996.
- 4 White, F.M., *Fluid Mechanics*. 3rd ed., McGraw-Hill, New York, 1994.
- 5 Artonkin, V.G., Petrov, K.P., *Investigations of aerodynamic characteristics of segmental conic bodies*. TsAGI Proceedings, No. 1361, Moscow, 1971 (in Russian).
- 6 Holman, J.P., *Heat Transfer*. 8th ed., McGraw-Hill, New York, 1997.
- 7 Humphrey, J.A.C., Taylor, A.M.K., and Whitelaw, J.H., *Laminar Flow in a Square Duct of Strong Curvature*. J. Fluid Mech., v.83, part 3, pp.509-527, 1977.
- 8 Van Dyke, Milton, *An Album of Fluid Motion. The Parabolic press*, Stanford, California, 1982.
- 9 Davis, G. De Vahl: *Natural Convection of Air in a Square Cavity: a Bench Mark Numerical Solution*. Int. J. for Num. Meth. in Fluids, v.3, pp. 249-264 (1983).
- 10 Davis, G. De Vahl, and Jones, I.P.: *Natural Convection in a Square Cavity: a Comparison Exercise*. Int. J. for Num. Meth. in Fluids, v.3, pp. 227-248 (1983).
- 11 Emery, A., and Chu, T.Y.: *Heat Transfer across Vertical Layers*. J. Heat Transfer, v. 87, p. 110 (1965).
- 12 Denham, M.K., and Patrick, M.A.: *Laminar Flow over a Downstream-Facing Step in a Two-Dimensional Flow Channel*. Trans. Instn. Chem. Engrs., v.52, pp. 361-367 (1974).
- 13 Yanshin, B.I.: *Hydrodynamic Characteristics of Pipeline Valves and Elements. Convergent Sections, Divergent Sections, and Valves*. “Mashinostroenie”, Moscow, 1965.
- 14 Enchao Yu, Yogendra Joshi: *Heat Transfer Enhancement from Enclosed Discrete Components Using Pin-Fin Heat Sinks*. Int. J. of Heat and Mass Transfer, v.45, p.p. 4957-4966 (2002).
- 15 Kuchling, H., *Physik*, VEB FachbuchVerlag, Leipzig, 1980.
- 16 Balakin, V., Churbanov, A., Gavrilouk, V., Makarov, M., and Pavlov, A.: *Verification and Validation of EFD.Lab Code for Predicting Heat and Fluid Flow*, In: CD-ROM Proc. Int. Symp. on Advances in Computational Heat Transfer “CHT-04”, April 19-24, 2004, Norway, 21 p.
- 17 Jonsson, H., Palm B., *Thermal and Hydraulic Behavior of Plate Fin and Strip Fin Heat Sinks Under Varying Bypass Conditions*, Proc. 1998 Intersociety Conf. On Thermal and Thermomechanical Phenomena in Electronic Systems (ITherm '98), Seattle, May 1998, pp. 96-103.
- 18 Henderson, C.B. *Drag Coefficients of Spheres in Continuum and Rarefied Flows*. AIAA Journal, v.14, No.6, 1976.

- 19 Jyotsna, R., and Vanka, S.P.: *Multigrid Calculation of Steady, Viscous Flow in a Triangular Cavity*. J. Comput. Phys., v.122, No.1, pp. 107-117 (1995).
- 20 Darr, J.H., and Vanka, S.P.: *Separated Flow in a Driven Trapezoidal Cavity*. J. Phys. Fluids A, v.3, No.3, pp. 385-392 (1991).
- 21 Michelsen, J. A., *Modeling of Laminar Incompressible Rotating Fluid Flow*, AFM 86-05, Ph.D. Dissertation, Department of Fluid Mechanics, Technical University of Denmark, 1986.
- 22 Sorensen, J.N., and Ta Phuoc Loc: *Higher-Order Axisymmetric Navier-Stokes Code: Description and Evaluation of Boundary Conditions*. Int. J. Numerical Methods in Fluids, v.9, pp. 1517-1537 (1989).
- 23 Visser, F.C., Brouwers, J.J.H., Jonker, J.B.: *Fluid flow in a rotating low-specific-speed centrifugal impeller passage*. J. Fluid Dynamics Research, 24, pp. 275-292 (1999).
- 24 Wesley, H. B., and Spyros, A. K.: *Experimental and computational investigation of sheet cavitation on a hydrofoil*. Presented at the 2nd Joint ASME/JSME Fluid Engineering Conference & ASME/EALA 6th International Conference on Laser Anemometry. The Westin Resort, Hilton Head Island, SC, USA August 13 - 18, 1995.
- 25 Winklhofer, E., Kull, E., Kelz, E., Morozov, A. *Comprehensive Hydraulic and Flow Field Documentation in Model Throttle Experiments Under Cavitation Conditions*. Proceedings of the ILASS-Europe Conference, Zurich, pp. 574-579 (2001).
- 26 Yershova, L., Volodin, V., Gromov, T., Kondratiev, D., Gromov, G., Lamartinié, S., Bibring, J-P., and Soufflot, A.: *Thermoelectric Cooling for Low Temperature Space Environment*. Proceedings of 7th European Workshop on Thermoelectrics, Pamplona, Spain, 2002.